The University Of Sheffield.

Greenland Ice Sheet hydrology and dynamics: the role of surface and basal topography

By:

Ádám Ignéczi

A thesis submitted in partial fulfilment of the requirements for the degree of Doctor of Philosophy

The University of Sheffield
Faculty of Social Sciences
Department of Geography

09.2018.

ABSTRACT

The Greenland Ice Sheet (GrIS) is an important and growing contributor to global sea level rise. However, the long-term influence of meltwater hydrology on GrIS dynamics (i.e. hydro-dynamics) and mass balance in a warming climate remains uncertain, partly due to our limited understanding of controls governing the large-scale spatial structure of surface drainage. Although the bed-to-surface transfer of basal topographical variations is thought to exert a key influence on surface hydrology, this is yet to be tested at the ice sheet-scale. Focussing on the contemporary GrIS, I use recent developments in the theory of bed-to-surface transfer to demonstrate that bed properties can be used to predict the surface relief of the ice sheet. Although the approach is approximate, the magnitude and spatial pattern of discrepancies with real topography are consistent with the limitations of the theory and known uncertainties of the input datasets. Additional analyses show that surface relief, which is predominantly controlled by the bed-to-surface transfer of basal topography, preconditions the large scale spatial structure of surface drainage. It follows that the spatial structure of surface drainage depends strongly on the transfer of basal topography to the ice surface. Based on these findings, I estimate the changing future distribution of surface lakes on the GrIS, which is crucial for hydro-dynamics as lakes can initiate surface-to-bed hydraulic connections through thick ice. The total volume of surface lakes is projected to increase sharply – by 172-270% – during the 21st century though the rate of increase slows between 2100 and 2300. The regional distribution of surface lakes is also projected to shift on the GrIS, from the SW to the W, NW and NE. Effects of the changing surface relief on surface lake distribution can be neglected during the 21st century, but projections beyond 2100 should incorporate them.

ACKNOWLEDGEMENTS

Firstly, I would like to thank the exceptional support and inspiration I received from my supervisors: Andrew Sole and Stephen Livingstone. I also thank you for making me feel welcomed in Sheffield and for providing me the opportunity to develop my research skills and ideas. I also want to express my special gratitude to Felix Ng, who developed some of the new mathematical methods which I have used in my work. These methods were inspired by my project but were developed and published by Felix (Ng et al., 2018), who also involved me in the writing process. I have gained particularly valuable experiences from this collaboration. I also want to thank the Ice and Climate Research at Sheffield (ICERS) for the financial support during my project.

During the writing and publication of my papers (Ignéczi et al., 2016, 2018), which provide the basis for this thesis, I gained valuable support from numerous researchers from both the UK and abroad. I would like to highlight the help of Amber Leeson who created a surface lake depth dataset for my project; results acquired from this are published in Ignéczi et al. (2016). I am also grateful for the support of Kang Yang, Nick Selmes, Xavier Fettweis, Noel Gourmelen and Kate Briggs who have not just supplied me with their published datasets, but also provided valuable advice as co-authors on my papers. I also want to thank Stephen Price, Joseph MacGregor and Miren Vizcaino for providing me with their previously published datasets, along with useful hints regarding their usage. I have also gained valuable insights regarding my project from discussions with Chris Clark, David Rippin and Ian Hewitt.

I want to express my gratitude to my parents for supporting me throughout my studies. Finally, I want to thank the selfless support, endless patience and excellent proofreading of my wife, Szonja Földi. This thesis would never have been finished without you.

CONTENTS

LIST OF FIGURES

LIST OF TABLES

CHAPTER 1: INTRODUCTION

1.1. Significance and rationale

The largest unknown factor in predictions of future global sea level rise is the contribution from contemporary ice sheets (IPCC, 2013). The annual mass loss of the Greenland Ice Sheet (GrIS) nearly tripled between 1958 and 2010 (Rignot et al., 2008; Shepherd et al., 2012), and currently the GrIS is the largest single contributor to global sea level rise (Shepherd et al., 2012; IPCC, 2013). Ice discharge across the grounding line and negative surface mass balance (SMB) – i.e. net ablation – contributed almost equally to the annual mass loss of the GrIS before 2005-2010. However, surface ablation has become the primary driver – currently accounting for about 60% - of the GrIS mass loss due to increasing surface melt and runoff (van den Broeke et al., 2009; Enderlin et al., 2014; van den Broeke et al., 2016). As the mass balance of the GrIS is modulated by the interactions between ice sheet hydrology and ice flow, i.e. hydro-dynamical processes (e.g. Zwally et al., 2002; Rennermalm et al., 2013; Nienow et al., 2017), reducing the uncertainty of future global sea level rise projections relies on improved understanding of the GrIS hydrological system (IPCC, 2013; Flowers et al., 2015).

The drainage system of the GrIS can be divided into supraglacial, englacial and subglacial components. The quantity and activity of water in the hydrological system and the interaction between the supra-, sub and englacial components is highly variable in time and space (Irvine-Fynn et al., 2011; Nienow et al., 2017). In general, the majority of meltwater is produced on the surface of the GrIS during summer (van den Broeke et al., 2009; van As et al., 2012; Enderlin et al., 2014). Once the firn/snow on the surface of the ice sheet becomes saturated with meltwater or melts completely – leading to a bare ice surface with low permeability – a complex surface drainage system of lakes, streams and moulins develops (Catania et al., 2010; Selmes et al. 2011, Irvine-Fynn et al., 2011; Smith et al., 2015; Yang and Smith, 2016; Karlstrom and Yang, 2016; Nienow et al., 2017).

The surface drainage system directly affects the mass balance of the GrIS by reducing the albedo and thus increasing surface melt, which results in a more negative SMB (Greuell et al., 2002; Lüthje et al., 2006; Tedesco et al., 2012). Although the presence of surface lakes increases surface melt rates by up to 110-170% - compared to bare ice – the relatively small spatial coverage of surface lakes currently limits the net

effect on GrIS mass balance (Greuell et al., 2002; Lüthje et al., 2006). However, the overall albedo-melt feedback caused by surface lakes is enhanced by the presence of meltwater in the saturated snowpack – i.e. slush – and in the spatially distributed surface stream network (e.g. Greuell et al., 2002). Furthermore, the expected future expansion of low albedo surface lakes towards higher elevations might lead to a larger impact on the GrIS mass balance (Lüthje et al., 2006).

As well as affecting the surface energy balance by reducing albedo, surface meltwater also penetrates to the ice sheet bed – thus entering into the subglacial drainage system – via moulins, which are surface-to-bed hydraulic connections formed by the hydrofracture of surface cracks/crevasses (van der Veen, 2007; Das et al., 2008; Krawczinsky et al., 2009; Poinar et al., 2017). As shown by theoretical calculations (Krawczinsky et al., 2009), if surface cracks – with an initial depth above 1-7 m – remain completely filled with meltwater, hydrofracture will reach the ice sheet bed forming surface-to-bed moulins in most cases. Hence, the hydrological connectivity between the supraglacial and subglacial drainage systems is strongly dependent on the presence of surface cracks/crevasses (Poinar et al., 2015; Christoffersen et al., 2018) and abundant meltwater supply (Krawczinsky et al., 2009; Poinar et al., 2017). Surface lakes, which form in topographical depressions during the melt season (Echelmeyer et al., 1991; Lampkin and VanderBerg, 2011; Sergienko 2013), are of key importance as they are capable of providing a stable and abundant source of meltwater to keep surface cracks water-filled until they reach the bed (Krawczinsky et al., 2009). Consequently, surface lakes are known to drain rapidly – i.e. in a matter of hours – to the ice sheet bed (e.g. Das et al., 2008; Selmes et al., 2011; Cooley and Christoffersen, 2017), though slower overland drainage into pre-existing moulins (Tedesco et al., 2013; Kingslake et al., 2015) and refreezing (Selmes et al., 2013) has also been observed.

The rapid drainage of surface lakes and subsequent surface-to-bed meltwater transport have substantial effects on the mass balance and dynamics of the GrIS (e.g. Zwally et al., 2002; Das et al., 2008; Sole et al., 2011; Doyle et al., 2014; Nienow et al., 2017). Abrupt surface-to-bed meltwater injections during rapid lake drainage events transiently overwhelm the subglacial drainage system, raising subglacial water pressure and/or sediment pore-water pressure. This causes reduced basal friction and/or sediment shear strength, resulting in transient ice flow accelerations (Zwally et al., 2002; Das et al., 2008; Shepherd et al., 2009; Bartholomew et al., 2010; Sole et al., 2011; Joughin et al., 2013; Bougamont et al., 2014; Cowton et al., 2016; Kulessa et al., 2017; Andrews et al., 2018; Hoffman et al., 2018). Ice flow acceleration causes faster transport of ice

towards lower elevations where surface melt is greater, thus leading to more intensive mass loss from the GrIS (e.g. Zwally et al., 2002). Ice flow accelerations might also lead to subsequent cascading hydrofracture and rapid lake drainage events due to tensile shock. This positive feedback allows the rapid drainage of lakes at high elevations where initial surface cracks are rare (Christoffersen et al., 2018; Hoffman et al., 2018).

Subglacial channel expansion from turbulent heat dissipation, and increasing subglacial connectivity – due to sustained large-magnitude surface-to-bed meltwater transport – leads to the more effective evacuation of subglacial meltwater, including from the distributed and weakly connected subglacial drainage system (Hoffman et al., 2017). Therefore, ice flow typically decelerates later in the melt season when surface-to-bed meltwater transport is steady or falling, due to increasing basal friction caused by the efficient low-pressure evacuation of meltwater from the subglacial drainage system (Andrews et al., 2014; Hoffman et al., 2017; Andrews et al., 2018). Minimum annual speed typically occurs following the seasonal cessation of melting, after which ice flow gradually recovers to pre-melt season levels due to re-pressurization of the now-inefficient subglacial drainage system by meltwater created by basal motion (Joughin et al., 2008; Sole et al., 2013). Hence, larger surface melting can regulate consequent increased summer ice flow due to the prolonged presence of a more widespread and larger bore low-pressure subglacial drainage system, which causes a greater drop in late-melt season basal water pressure and in winter ice flow velocities (Sole et al., 2013). An alternative hypothesis explains the seasonal and interannual ice flow variations by temporal changes in the shear strength of basal sediments (Bougamont et al., 2014). In this hypothesis, early season inputs of surface meltwater lead to increased pore water pressures that weaken the sediment and thus increase ice flow, while reduced ice motion in late summer is caused by an increase in sediment strength due to reduced water flow through now-expanded pore spaces (Bougamont et al., 2014; Kulessa et al., 2017). In contrast to self-regulation due to reduction in regional basal water pressure by flow into low pressure channels, some modelled scenarios with extensive basal sediment cover indicate a net increase in ice motion in warmer years (Bougamont et al., 2014). This implies a positive feedback between surface melt and increased ice flow towards the ice sheet margin. However, such a relationship has not been observed. Instead, decadal observations, where available (e.g. Tedstone et al., 2015; van de Wal et al., 2015), show a reduction in annual ice motion as surface melt increases. Furthermore, the prevalence of basal sediment cover is unclear, despite some evidence for its presence in certain regions (e.g. Kulessa et al., 2017).

At higher elevations far from the ice sheet margin, the formation of effective subglacial drainage systems – especially subglacial channels – is thought to be hindered by thick ice, low moulin density, small surface-to-bed meltwater transport and low hydraulic potential gradients. Hence, the effective evacuation of subglacial meltwater, especially from weakly connected regions and/or basal sediments, might be hindered in these regions (Doyle et al., 2014; Dow et al., 2014; Dow et al., 2015; Banwell et al., 2016; Hoffman et al., 2017; Kulessa et al., 2017). Although few studies are available from this zone, Doyle et al. (2014) have observed a small annual net increase in the ice flow velocity that coincided with increasing surface melt, which supports the theoretical implications discussed above. However, it remains unclear how self-regulation will affect hydrologically induced ice flow variations at high elevations on the GrIS in the future.

Besides the direct effects on ice flow, enhanced surface-to-bed meltwater transport can also increase the energy flux into the interior of the ice sheet – i.e. cryohydrological warming – altering ice rheology and/or the thermal conditions of the ice sheet bed, causing faster ice flow velocities (Phillips et al., 2010; Doyle et al., 2014). The formation of surface-to-bed moulins and effective subglacial drainage systems also enables the rapid transfer of surface meltwater to the ice sheet margin, thereby reducing the retention and refreezing of meltwater (Willis et al., 2015; Smith et al., 2015). This process also affects the magnitude and timing of freshwater and nutrient delivery to the oceans (Irvine-Fynn et al., 2011; Hawkings et al., 2015). Surface-to-bed and subsequent subglacial meltwater transport to the grounding lines of tidewater glaciers emerges as buoyant freshwater plumes. These plumes entrain ambient fjord water as they rise towards the fjord surface, establishing an along-fjord circulation where coastal ocean water is drawn towards the glaciers at approximately their grounding line depths, and water leaves the fjord at shallower depths. This circulation has important implications for ice-ocean interactions because it maintains the contact between the glaciers and relatively warm coastal waters (Cowton et al., 2015), and thus also enhances submarine melt rates. Therefore, in a warming climate larger magnitude freshwater discharge at the grounding lines of tidewater glaciers in Greenland – due to increasing surface melt and runoff – is likely to cause more intensive undercutting and calving of tidewater glacier termini (Motyka et al., 2003; Straneo et al., 2011; Carroll et al., 2015; Slater et al., 2015, 2017a, 2017b; Cowton et al., 2018).

Despite these advancements in the understanding of ice sheet hydro-dynamics, the net long-term influence (10^2 years and longer) of hydrology on GrIS flow, mass

balance and downstream ecosystems in a warming climate remains uncertain, because existing observations of the relevant mechanisms – discussed above – cover only a relatively short time period (< 20 years) and are yet to be incorporated in a robust manner into ice sheet models (IPCC, 2013; Flowers et al., 2015). As an initial step in achieving this goal, the factors which control the long-term evolution of the spatial structure of surface drainage on the GrIS need to be explored, as this is key to resolving the spatial and temporal influence of surface drainage on the mass balance and dynamics of the GrIS. Furthermore, the distribution and extent of future surface-to-bed meltwater connections at high elevations has also been identified as a key priority for further investigations on GrIS hydrology (Nienow et al., 2017).

1.2. Research context

1.2.1. The effects of hydrology on the ice flow of temperate and polythermal valley glaciers

Although basal sliding has been recognized as a contributor to the overall movement of glaciers since the mid-1800s (Flowers, 2010), theories describing subglacial channels and cavities, the movement of meltwater within glaciers, and the role of these processes in basal sliding have only been formulated since the mid-1900s (e.g. Lliboutry, 1958; Weertman, 1964; Shreve, 1972; Röthlisberger, 1972; Iken, 1981). Observations have also linked the spatiotemporal evolution of ice flow – such as surges (e.g. Kamb et al., 1985), ice streaming (e.g. Alley et al., 1986), and seasonal-diurnal ice flow velocity cycles (e.g. Iken et al., 1983; Iken and Bindschadler, 1986; Nienow et al., 2005) – to changes of the glacial drainage system. The work of Iken et al. (1983) is of particular interest as this study empirically demonstrated that horizontal ice flow velocity correlates well with the rate of glacier uplift – instead of the absolute vertical displacement – on the Unteraargletscher, Alps. Furthermore, the largest speed-up/uplift events were linked to periods of increased surface melt. In conclusion, Iken et al. (1983) proposed that ice flow velocity is more responsive to variations in subglacial water pressure – initiated by surface-to-bed meltwater transport – than to the amount water stored at the ice-bed interface, or to the size of subglacial cavities/channels. This interpretation was later confirmed by borehole water pressure measurements on the Findelengletscher, Alps (Iken and Bindschadler, 1986).

As demonstrated above, the coupling between surface melt, subglacial water pressure and ice flow velocity was well studied and understood even as early as the 1980s. However, most studies focussed on temperate glaciers (glaciers where ice is at the pressure-melting point, except for the topmost 10-15 m which experiences seasonal temperature variations) and the coupling between surface melt and ice flow velocity on polythermal glaciers (glaciers with a perennial occurrence of both temperate and cold ice) was considered ambiguous until recently (e.g. Copeland et al., 2003; Irvine-Fynn et al., 2011). Despite the notion that surface-to-bed meltwater transport is hindered by cold ice (e.g. Hooke, 1989; Hodgkins, 1997) seasonal ice flow variations were detected on predominantly cold polythermal glaciers – e.g. in the Canadian Arctic Archipelago (Müller and Iken, 1973; Iken, 1974; Copeland et al., 2003) – and even on the GrIS (e.g. Zwally et al., 2002). By the late 2000s sufficient evidence had been gathered to demonstrate that surface meltwater was transported to the bed of polythermal glaciers – enabled by hydrofracture (van der Veen, 2007) – and that the coupling between surface melt and ice flow velocity was similar for both temperate and polythermal glaciers (e.g. Copeland et al. 2003; Bingham et al., 2005; 2006). Much of the work dealing with hydro-dynamical process of the GrIS (Section 1.1) is based on these findings – i.e. from temperate and polythermal valley glaciers – albeit in the case of the GrIS it took another decade to obtain the necessary field evidence.

1.2.2. The spatial structure of surface drainage and its controlling factors on the GrIS

Satellite derived observations have provided insights into the spatial structure and the seasonal evolution of surface drainage on the GrIS. Surface lakes are initially formed at low elevations around the margin of the GrIS, and as the melt season progresses they tend to form and drain at higher elevations (McMillan et al., 2007; Sundal et al., 2009; Lampkin, 2011; Liang et al., 2012; Johansson et al., 2013; Morriss et al., 2013; Fitzpatrick et al., 2014). Late in the melt season, the drainage and refreezing of surface lakes causes their overall extent to decrease (e.g. Leeson et al., 2013; Selmes et al., 2013; Fitzpatrick et al., 2014). In years with warmer summers, surface lakes appear earlier and expand to higher elevations (Liang et al., 2012; Morriss et al., 2013; Fitzpatrick et al., 2014). At low elevations small and highly clustered surface lakes dominate, while at higher elevations the lakes are larger and less clustered (Lampkin, 2011; Fitzpatrick et al., 2014). For example, in West Greenland Lampkin

(2011) reported <0.5 km^2 mean area and ~100-500 m average spacing for lakes between the elevations of 100 and 700 m, while these figures increase to 0.5-1 km^2 and ~900-1400 m – respectively – for lakes between the elevations of 700 and 1200 m.

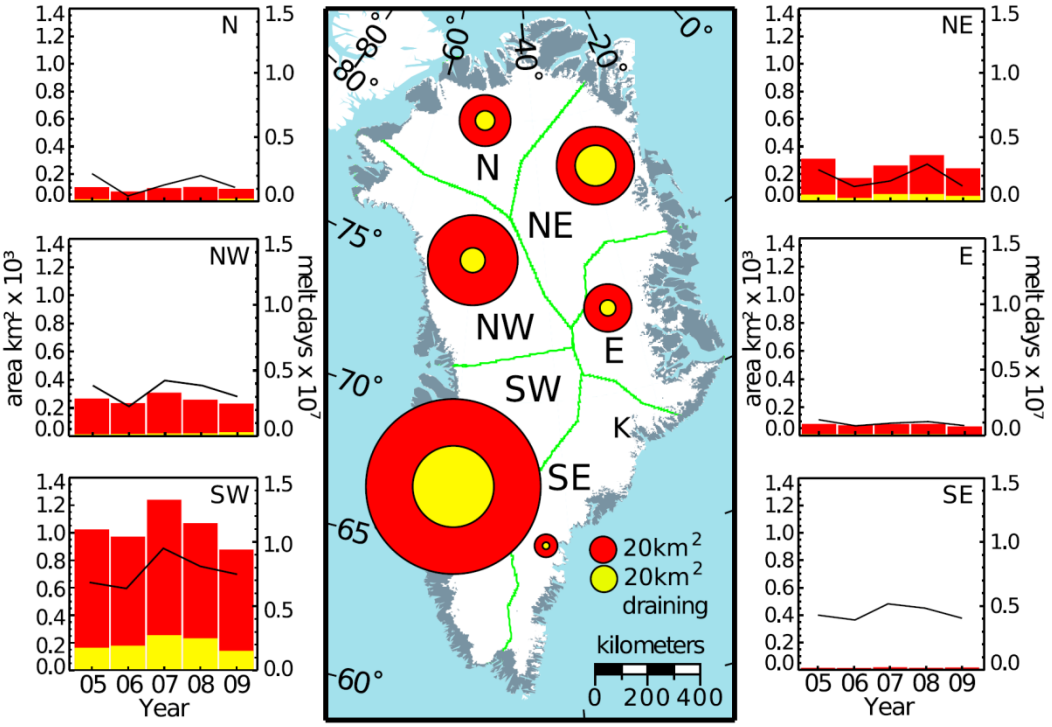

Figure 1.1 The distribution of lake area (red) and rapidly draining lake area (yellow) on the GrIS. The map shows the mean distribution for 2005-2009, while the bar graphs show the annual variations with the melt intensity also plotted (Source: Figure 2 in Selmes et al., 2011).

Despite the recent focus on the effects of hydrology and rapid lake drainage on GrIS mass balance and dynamics (Section 1.1), estimations of the relative frequency and spatiotemporal distribution of rapid lake drainage on the GrIS vary widely (Cooley and Christoffersen, 2017). The relative frequency of rapid lake drainage is estimated to range between 1-28% in West Greenland (Liang et al., 2012; Morriss et al., 2013; Fitzpatrick et al., 2014), while the only study available for the whole GrIS estimates 13% (Selmes et al., 2011). Selmes et al. (2011) have also shown that rapid lake drainage is more frequent in SW, N and NE Greenland compared to other regions of the ice sheet (Fig. 1.1). However, Cooley and Christoffersen (2017) demonstrated that previous investigations have underestimated the relative frequency of rapid lake drainage due to cloud cover exacerbating the limited temporal resolution of satellite imagery; according to them 36-45% of the surface lakes in West Greenland drain rapidly. Rapid surface lake drainage events are observed throughout the melt season but they peak around the time of the maximum overall extent of lake coverage (e.g. Morriss et al., 2013).

Fitzpatrick et al. (2014) also showed that surface lakes at high elevations tend to have multiple rapid drainage events due to the fast creep-closure of surface-to-bed moulins. Other mechanisms of surface lake cessation – i.e. refreezing and slow drainage overland – have received little attention on the GrIS (Johansson et al., 2013; Selmes et al., 2013). Although little information is available, it has been proposed that refreezing surface lakes are common on the GrIS – around 12-46% of surface lakes refreeze at the end of the melt season – especially at high elevations (Selmes et al., 2013; Johansson et al., 2013). The slow overland drainage of surface lakes into pre-existing moulins/crevasses at lower elevations – due to thermal incision of surface streams once the lip of the lake basin is overtopped (e.g. Kingslake et al., 2015) – is also estimated to be widespread. Although around 34% of the surface lakes on the GrIS are proposed to drain slowly overland (Selmes et al., 2013), the study of Cooley and Christoffersen (2017) indicates a degree of uncertainty about this figure by revealing the underestimation of rapid lake drainage frequency.

The majority of previous investigations have focused on small areas in W and SW Greenland (e.g. McMillan et al., 2007; Lampkin, 2011; Liang et al., 2012; Johansson et al., 2013; Morriss et al., 2013; Fitzpatrick et al., 2014), though there are a handful of more spatially comprehensive studies. These latter studies demonstrate that surface lake formation is widespread across the GrIS, although the greatest frequency of lakes occurs in SW Greenland (Sundal et al., 2009; Selmes et al., 2011; Howat et al., 2013). Meanwhile, surface lakes are relatively scarce in the E and SE (Fig. 1.1) due to the high surface slope and large mass-balance gradient, which hinders the saturation of surface layers (Sundal et al., 2009; Howat et al., 2013). Sundal et al. (2009) also showed that there is a 2-3 week delay in the evolution of surface lakes in N Greenland compared to the south due to latitudinal temperature – and thus melt – gradients.

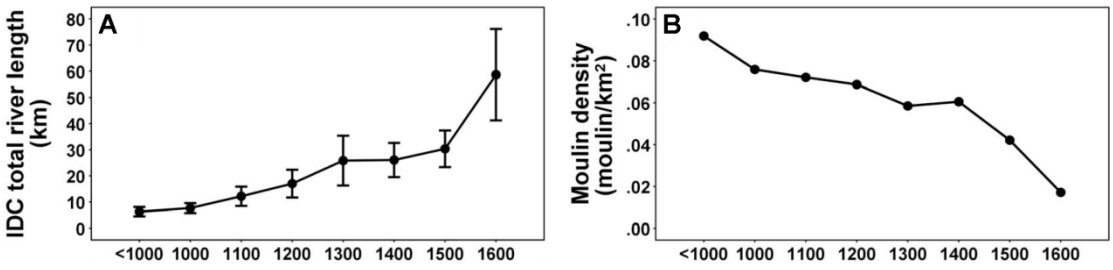

Figure 1.2 (A) The changing total river length in internally drained catchments and (B) moulin density by elevation (Source: Figure 5 in Yang and Smith, 2016).

Although surface lakes have been the focus of supraglacial hydrology investigations over the last decade or more, there are also a number of studies that provide insights about the spatial structure of surface streams and moulins (e.g. Lampkin and VanderBerg, 2014; Clason et al., 2015; Smith et al., 2015; Yang et al., 2016; Yang and Smith, 2016). During each summer, supraglacial streams form dendritic networks on the surface of the GrIS (Irvine-Fynn et al., 2011; Rennermalm et al., 2013; Smith et al., 2015). Surface streams incise into the ice surface due to thermal erosion, and strongly influence the ice surface topography on short – i.e. 100-200 m – length-scales (Karlstrom and Yang, 2016). Observations from west Greenland indicate that only a small fraction of the surface stream networks drain directly into proglacial rivers, with the majority internally drained via a terminal lake or moulin (Yang and Smith, 2016; Yang et al., 2016). Similar to surface lakes, surface stream networks expand to higher elevations during the melt season (Lampkin and VanderBerg, 2014), while the number of streams and the ratio of internally draining streams also increase (Lampkin and VanderBerg, 2014). This corresponds well with the increasing frequency of rapid lake drainage events (Morriss et al., 2013) and moulin formation as the melt season progresses (Clason et al., 2015). The majority of moulins form close to the ice sheet margin (Fig. 1.2) due to the hydrofracture of crevasses, which are more abundant at low elevations (Clason et al., 2015; Poinar et al., 2015; Yang and Smith, 2016). However, moulins also form at higher elevations due to hydrofracture and rapid lake drainage (Clason et al., 2015; Cooley and Christoffersen, 2017). This is now thought to occur even in the absence of initial surface cracks formed by tensile stresses of the background ice flow – which are rare at higher elevations (Poinar et al., 2015) – due to tensile shocks initiated by rapid lake drainage events at lower elevations (Stevens et al., 2015; Christoffersen et al., 2018; Hoffman et al., 2018). Meltwater is transported over larger distances in surface stream networks at high elevations, which is indicated by the larger total length of surface streams in internally drained catchments at high elevations, i.e. 58.7 km above 1600 m and 6.3 km below 1000 m (Yang and Smith, 2016) (Fig. 1.2). However, significant meltwater transport from high to low elevations has not been observed on the surface of the ice sheet in West Greenland due to the shape and size of internally drained catchments (Yang and Smith, 2016). Hence, the surface-to-bed meltwater transport is efficient even at high elevations, once the surface drainage system becomes mature late in the melt season (Smith et al., 2015; Yang and Smith, 2016).

The spatial structure and temporal evolution of surface drainage is controlled by a range of exogenic and endogenic – i.e. in relation to the ice sheet surface – processes. Meltwater production and runoff are the key exogenic processes controlling the seasonal evolution of the surface drainage system. These in turn depend on atmospheric and ice surface conditions, including temperature, irradiation, precipitation, firn layer thickness, surface permeability and albedo (e.g. Lüthje et al., 2006; Leeson et al., 2012; Lampkin and VanderBerg, 2014; Clason et al., 2015; Poinar et al., 2017). However, surface lakes, major surface streams and moulins have also been observed to re-occur in approximately the same location from year to year, instead of advecting with ice flow (Echelmeyer et al., 1991; Catania et al., 2010; Selmes et al., 2011). This indicates that the large-scale spatial structure of surface drainage is strongly influenced by ice surface topography (e.g. Lüthje et al., 2006; Banwell et al., 2012; Leeson et al., 2012; Joughin et al., 2013; Karlstrom and Yang, 2016) which – on length scales comparable to the ice thickness – is thought to be predominantly controlled by endogenic processes, i.e. the transfer of basal variability (Gudmundsson et al., 2003; Raymond and Gudmundsson, 2005; Ng et al., 2018). These observations and theories support the idea that ice surface topographical features can be fixed in space by the bed topography at scales relevant to the routing of surface water. Accordingly, surface lakes, surface drainage basins and surface meltwater flux have been observed to correlate spatially with basal topography (Lampkin and VanderBerg, 2011; Karlstrom and Yang, 2016). However, to date, empirical tests of the hypothesis have been spatially limited (Lampkin and VanderBerg, 2011; Karlstrom and Yang, 2016) and have not utilized the bed-to-surface transfer theory (Gudmundsson, 2003) to predict surface topography or drainage structures.

1.2.3. The transfer of basal variability to the surface

The vertical variability of bed elevation over a given horizontal distance, i.e. bed roughness (e.g. Bingham and Siegert, 2009), plays a key role in the flow of glaciers and ice sheets as it influences the coupling between the ice and the bed – for example controls sliding velocity (e.g. Weertman, 1964) – and also affects the transient response of ice flow to meltwater injections to the bed (Iken, 1981). Besides its influence on ice flow, bed roughness – when combined with other lines of evidence – could be used to infer subglacial geology, erosion rates, the thermal regime of basal ice, and ice sheet evolution (e.g. Bingham and Siegert, 2009; Rippin, 2013; Rippin et al., 2014; Ross et al., 2014). Precise knowledge of bed roughness is also important when assessing the

sensitivity of an ice sheet – or certain ice streams, for example the Pine Island Glacier, Antarctica – to future changes (Bingham et al., 2017), and when using radar scattering to infer the presence of subglacial water (Jordan et al., 2017).

Modulated by ice thickness, bed roughness and slipperiness also influence spatial variations in ice surface topography and velocity (e.g. Gudmundsson et al., 1998; Gudmundsson, 2003). As the spatial variability of surface elevation – i.e. surface roughness – affects ice surface texture, satellite imagery could be used to infer ice thickness and subglacial geomorphology (e.g. Ross et al., 2014; Chang et al., 2016). This approach is especially useful in regions where ice penetrating radar measurements are scarce, e.g. Princess Elizabeth Land in East Antarctica (Jamieson et al., 2016). Besides qualitative inferences obtained from ice surface texture, quantitative numerical inversions estimating basal roughness (causing 'form drag') and slipperiness (causing 'skin drag') have also been carried out by several investigations, to better constrain predictive ice sheet models (e.g. Kyrke-Smith et al., 2018). Some inversion techniques only require high resolution measurements of ice surface topography and velocity, and invert simultaneously for basal topography and slipperiness using Bayesian statistical inference methods (e.g. Raymond and Gudmundsson, 2009; Raymond Pralong and Gudmundsson, 2011). However, most techniques invert only for basal slipperiness – using the full Stokes equations – and require measurements of ice thickness, in addition to high resolution surface topography and velocity data (e.g. Kyrke-Smith et al., 2017; 2018). Although increasing the spatial resolution of ice thickness measurements enhances the accuracy of basal slipperiness inversions – due to the better resolved bed roughness – results appear to be more strongly influenced by the misfit optimisation procedure (Kyrke-Smith et al., 2018). Measurements independent of ice flow models – such as seismic surveys (e.g. Brisbourne et al., 2017) – also hold much promise in resolving basal slipperiness, though further theoretical work is necessary to incorporate such outputs into ice sheet models (Kyrke-Smith et al., 2017).

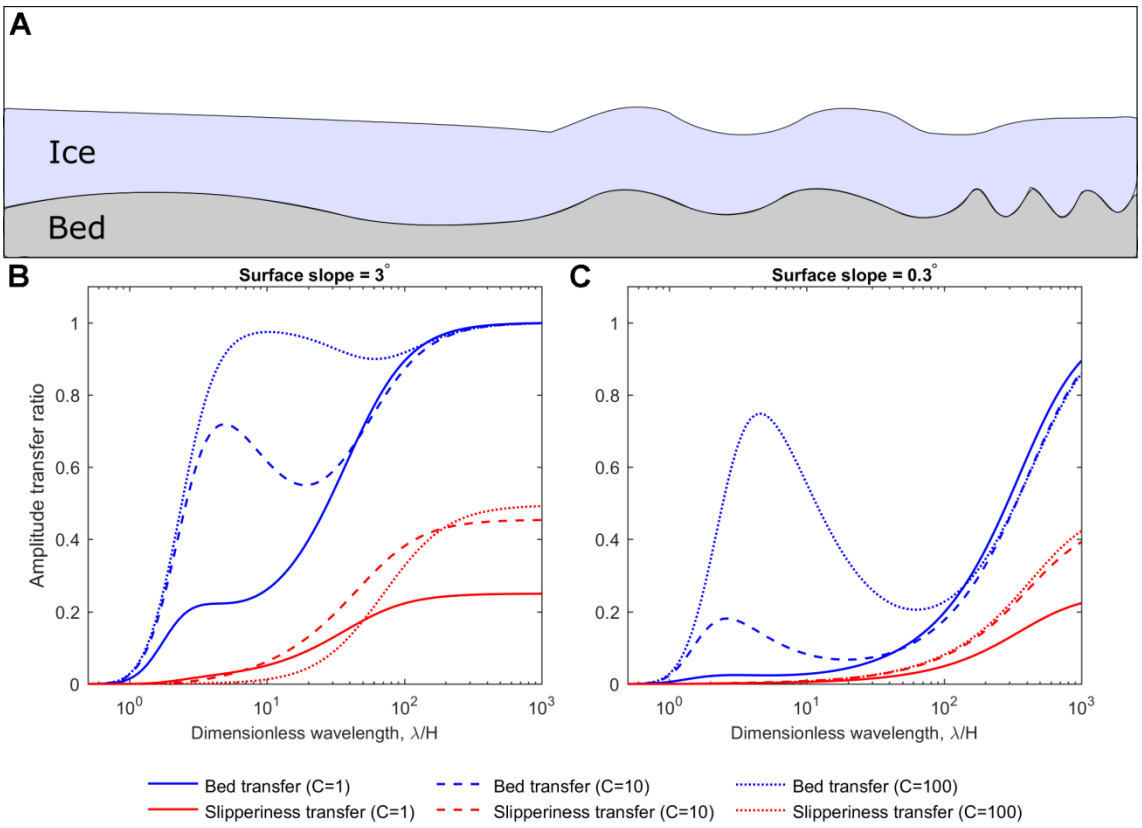

Figure 1.3 (A) Cartoon illustrating the transfer of basal topographical variability (perturbations) to the ice surface. Ice flow behaves as a filter preferentially transferring bed topographical undulations of particular wavelengths compared to the ice thickness. (B-C) Non-dimensional amplitude transfer ratios of basal topographical perturbations (blue lines) and basal slipperiness perturbations (red lines) for a wide range of non-dimensional wavelengths and basal slip ratios (C = 1, 10 and 100; solid dashed and dotted lines respectively) and surface slopes.

In the remainder of this section, I focus on the aforementioned influence of basal variability – both topographical and slipperiness – on ice surface topography, within the framework of Gudmunsson's (2003) analytical theory of basal variability transfer. The surface topography of glaciers and ice sheets exhibits undulations superimposed on their general shape (Fig. 1.3A). On length-scales comparable to the ice thickness (i.e. mesoscale) these surface topographical undulations are controlled by the transfer of basal topographical and slipperiness variability to the surface (Gudmundsson et al., 1998; Gudmundsson, 2003; Raymond and Gudmundsson, 2005; De Rydt et al., 2013; Ng et al., 2018). Gudmundsson (2003) derived his theory, describing this control, by using the full Stokes equations and perturbation theory as a starting point – thus the effects of longitudinal stress components are resolved – assuming steady, plane-parallel ice flow and linear ice viscosity. The resulting linearised transfer equations operate in the Fourier-domain (i.e. describe wavelength/frequency dependent transfer) and demonstrate that the amplitude of surface topographical undulations is controlled by the non-dimensional wavelength – i.e. undulation wavelength (λ) / ice thickness (H) – and

amplitude of basal topographical and slipperiness undulations, the ice surface slope and the basal slip ratio (*C*), i.e. sliding velocity / deformational velocity (Fig 1.3B-C). In general, the bed-to-surface transfer is more efficient where the basal slip ratio and/or the ice surface slope is larger. The bed-to-surface transfer of basal topographical and slipperiness perturbations is inefficient at short non-dimensional wavelengths. Although the efficiency generally increases with the non-dimensional wavelength, the bed-to-surface topography transfer exhibits a local maximum (Gudmundsson, 2003) (Fig. 1.3B). It was shown by finite element simulations (Raymond and Gudmundsson, 2005) that a departure from linear ice flow (i.e. non-linear ice viscosity) does not affect the bed-to-surface transfer fundamentally. Although the quantitative characteristics of the transfer change due to non-linearity, the qualitative aspects – e.g. number of local maxima and inflection points on the transfer functions – remain largely unchanged.

The transfer theory of Gudmundsson (2003) was derived for plane-parallel ice flow, which means that it assumes uniform ice thickness, ice surface slope and basal slip ratio. Although this approximation holds in certain cases – e.g. on Antarctic ice stream trunks, where De Rydt et al. (2013) tested Gudmundsson's (2003) theory successfully – in general, ice thickness, ice surface slope and basal slip ratio vary considerably. A new extension of the theory by Ng et al. (2018) considers Gudmundsson's (2003) transfer functions as Fourier transforms of impulse response functions in the spatial domain and employs an approximation based on non-stationary convolution (e.g. Margrave, 1998), to allow calculations of the bed-to-surface transfer on non-uniform (i.e. changing ice thickness, ice surface slope and basal slip ratio) glacier flowlines. Ng et al. (2018) used three non-uniform synthetic glacier flowlines – calculated using finite element Stokes flow – to show that the predicted surface topographical undulations correlate well with the surface topographical undulations calculated using the finite element full Stokes equations (Pearson correlation coefficient; $R > 0.9$). Two real non-uniform glacier flowlines – one on the Columbia Glacier, Alaska and one ending on the Nordenskiöld Glacier, GrIS – were also investigated by Ng et al. (2018). Although the correlations were lower in these cases ($R \sim 0.6$-0.7) – mostly due to lateral variations in the background ice flow and data availability/quality issues – qualitative features of the surface topography along the flowlines were reproduced. However, the original theory of Gudmundsson (2003) and the non-stationary extension (Ng et al., 2018) have not been tested on an ice sheet-wide array of glacier flowlines.

1.2.4. Estimating the future spatial structure of GrIS surface drainage

Surface topography is thought to be the first order control on the spatial distribution of surface drainage (Section 1.2.2). This relationship is the most obvious in the case of surface lakes, which form by the accumulation of surface meltwater in closed topographical basins (Echelmeyer et al., 1991). Several studies have utilized this intuitive and simple fact, and used surface DEMs and meltwater production estimates to route meltwater over the surface of the ice sheet to model the contemporary and future evolution of surface lakes (Leeson et al., 2012, 2015; Arnold et al., 2014). This approach circumvents several problems associated with satellite observations of surface lakes, such as clouds, shadows and revisit frequency (Arnold et al., 2014). Despite these advantages, the resolution and accuracy of the ice surface DEM (Yang et al., 2015) and the fact that not all depressions host lakes somewhat limits the power of this approach. However, Leeson et al. (2012) found that modelling the seasonal evolution of surface lakes using this method produced reasonable estimations in SW Greenland.

Since 2000 the maximum elevation of surface lakes has increased remarkably, on the order of hundreds of metres (Howat et al., 2013; Gledhill and Williamson, 2017). However, to date only Leeson et al. (2015) have modelled the long-term future distribution of surface lakes. Leeson et al. (2015) focused on a ~ 20,000 km^2 area in SW Greenland and used a surface lake initiation and growth model (Leeson et al., 2012) forced by moderate and high climate change scenarios. They predicted that the maximum elevation of lakes will increase by 399-426 m (reaching elevations around 2191-2221 m) and the lake covered region will expand inland by 103-110 km during 2000-2060 in SW Greenland. Using an empirically based extrapolation of these results to the whole ice sheet – based on the empirical relationship between the elevation of surface lakes and geographical latitude – they suggested a 48–53% increase in the total area over which surface lakes are distributed by 2060 (Leeson et al., 2015). However, this investigation only considered a fixed (i.e. present-day) rather than a dynamically evolving ice surface topography (e.g. Vizcaino et al., 2014). They also used a relatively small study area to extrapolate ice sheet-wide trends, which assumes that the surface topography (e.g. distribution surface depressions) and ice-surface conditions (e.g. firn thickness and runoff) are representative of the wider GrIS. Hence, a wider assessment of the changing future distribution of surface lakes on the GrIS, that incorporates regional differences in the favourability for surface lake formation (e.g. the availability of

surface depressions) and the effect of changing endo- and exogenic controls (Section 1.2.2 and 1.2.3), is still missing.

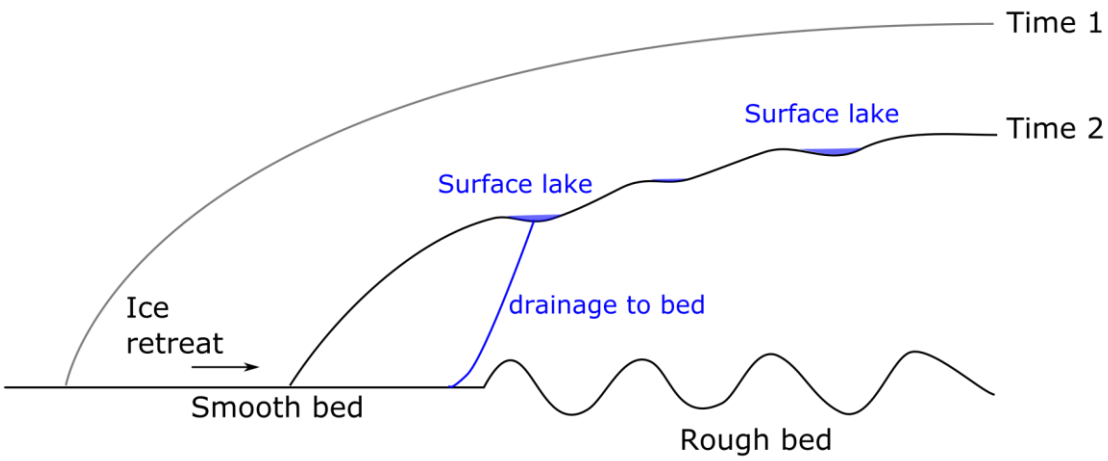

Figure 1.4 Concept of how an evolution of ice sheet geometry modifies the transfer of basal variability to the surface, and thus the spatial structure of surface drainage.

Changing endogenic controls on the surface drainage can be described within the framework of the bed-to-surface transfer theory (Gudmundsson, 2003). Since temporally-evolving ice thickness affects the spatial distribution of mesoscale ice surface undulations (Gudmundsson, 2003; Ng et al., 2018), which are thought to influence the distribution of surface drainage (e.g. Lampkin and VanderBerg, 2011), the validity of surface drainage (e.g. surface lake) projections assuming stationary ice surface topography (e.g. Leeson et al., 2015) is limited by the persistence of surface undulations. On longer time scales, evolving ice thickness (e.g. Pritchard et al., 2009; Vizcaino et al., 2014) could significantly modify the pattern of mesoscale surface topographical undulations, and thus the spatial distribution of surface drainage (Lampkin and VanderBerg, 2011) (Fig. 1.4). Although higher-order ice sheet models are capable of simulating the necessary topographical details, the computational costs of producing such simulations at the required spatial resolution limit their applicability for ice sheet-scale problems.

This thesis overcomes issues caused by extrapolating projections carried out in a small area (Leeson et al., 2015) by considering regional variations in the distribution of surface depressions on the GrIS. Furthermore, I also circumvent the problem posed by the assumption of stationary ice surface topography. In order to achieve this I use the non-stationary extension of Gudmundsson's (2003) transfer theory developed by Ng et al. (2018), whereby the mesoscale surface undulations are calculated from bed topography DEMs, available at relatively high resolution, and modelled surface

topography and flow state, which are available at lower resolution (Ng et al., 2018). This approach enables extension of the timescale of surface drainage projections and thus informs the long-term response (>10^2 years) of the GrIS to changes in the surface and subglacial drainage.

1.3. Aims and objectives

My aim is to investigate the role of basal variability in controlling the large-scale current and future spatial structure of surface drainage on the GrIS.

1.3.1 Objectives

O1.) Ice sheet-wide application of the non-stationary extension of Gudmundsson's (2003) transfer theory.

I apply the non-stationary transfer integral of Ng et al. (2018) to thousands of ice flowlines across the GrIS to predict surface topographic undulations. This builds on the work of Ng et al. (2018), who successfully applied the non-stationary extension of Gudmundsson's (2003) transfer theory to three synthetic and two real glacier flowlines. This analysis produces ice sheet wide maps of predicted and observed surface relief – i.e. topographical variability of the ice sheet surface derived from the amplitudes of mesoscale surface topographical undulation profiles – which I use to explore the limitations of the theory (O2).

O2.) Determine controls governing the bed-to-surface transfer and the accuracy of the non-stationary extension of Gudmundsson's (2003) transfer theory.

The ice sheet-wide datasets, obtained in O1, allow a more in-depth investigation of the explanatory power and the practical limitations of the bed-to-surface transfer theory. Here I calculate the ice sheet-wide correlation of the observed and predicted surface relief and carry out sensitivity tests to estimate the ice sheet-wide relative importance of the bed-to-surface slipperiness transfer. Finally, I investigate the factors that could hinder the accuracy of the bed-to-surface transfer theory, using the ice sheet-wide difference between the observed and predicted surface relief.

O3.) Evaluate the influence of the bed-to-surface transfer on the large-scale spatial structure of surface drainage.

I test the hypothesis of basal (endogenic) control on the large-scale spatial structure of surface drainage (Section 1.2.2). First, I compare satellite imagery-derived and surface DEM-derived surface drainage features with observed/predicted surface relief from O1. To filter out exogenic controls (Section 1.2.2), I control for runoff when comparing satellite imagery derived surface drainage features and surface relief in SW Greenland. Finally, I derive empirical relationships between the observed/predicted surface relief and surface drainage features.

O4.) Estimate the distribution of surface lakes on the GrIS during the 21st century assuming a fixed ice sheet surface topography.

Several studies have used surface DEMs and surface meltwater routing to model the evolution of surface lakes (Section 1.2.4). However, only Leeson et al. (2015) have modelled the future evolution of surface lakes on the GrIS, and these projections were only applied to a small area in SW Greenland and then extrapolated to the ice sheet scale (Section 1.2.4). I avoid the need for spatial extrapolation by using ice sheet-wide modelled SMB and surface depression inventory – derived from surface DEMs – to estimate the changing future distribution of surface lakes and their potential for rapid lake drainage.

O5.) Estimate the changing future distribution of surface lakes between 1980-2300 using an evolving ice surface topography.

The potential effects of evolving ice surface topography – due to changing endogenic controls, i.e. bed-to-surface transfer – on surface drainage are acknowledged by several studies (Section 1.2), but none have quantified the impact. In order to estimate the influence of an evolving ice surface topography on future surface drainage, I apply the transfer integral in O1 to modelled future ice sheet surface topography and basal slipperiness. The results enable quantification of the specific effect of the changing surface topography – due to changing bed-to-surface transfer – on the total volume and distribution of surface lakes. Finally, I also estimate the effect of evolving ice surface topography on the changing future potential for hydrofracture and rapid lake drainage.

1.4. Thesis structure, relation to previous publications, and workflow

The above 5 objectives are detailed in the following three chapters. In Chapter 2, I apply the non stationary extension of Gudmundsson's (2003) transfer theory (Ng et al., 2018) to ice sheet wide datasets (O1). Here, I also investigate the dominant controlling factors on the surface relief of the GrIS and the accuracy of the predictions (O2). In Chapter 3, I investigate empirical relationships that describe the control of basal variability on the large-scale spatial structure of GrIS surface drainage (O3). Finally, using the outcomes from Chapters 2 and 3, I estimate the future distribution of surface lakes assuming stationary (O4) and evolving (O5) ice surface topography in Chapter 4.

The new non-stationary extension of Gudmundsson's (2003) transfer theory (Ng et al., 2018) – which makes it possible to calculate the bed-to-surface transfer on non-uniform glacier flowlines – is one of the central concepts applied in this dissertation (O1-3, O5). The mathematical theory – i.e. the non-stationary integrals which describe the non-uniform bed-to-surface transfer – was developed by Dr Felix Ng and published in Ng et al. (2018), though this work was inspired by my PhD project and I was involved in the publication of the paper. Before this collaboration yielded the necessary mathematical tools to tackle O1-3 and O5, I had carried out the analyses outlined in O4. These results have been published in Ignéczi et al. (2016) and included in Chapter 4. Although the results included in Chapter 4 are similar to the ones published in Ignéczi et al. (2016), they have been updated to include the MEaSUREs Greenland Ice Mapping Project (GIMP) DEM from GeoEye and WorldView Imagery, Version 1 dataset (Howat et al., 2014; 2017) which was released after the publication of Ignéczi et al. (2016). I have also amended the results published in Ignéczi et al. (2016) with new estimations of the potential for rapid lake drainage. After the non-stationary transfer equations – published in Ng et al. (2018) – became available, I carried out the analyses outlined in O1-3 and O5 in their respective order. Results from O1-3 are published in Ignéczi et al. (2018) and included in Chapters 2 and 3. Results of O5 have not been published yet. Although both of my published papers (Ignéczi et al. 2016, 2018) are relevant to Chapter 1, I have refrained from citing and discussing them as the results published in these two papers are presented in the thesis.

CHAPTER 2: CONTROLS ON THE SURFACE TOPOGRAPHICAL VARIABILITY OF THE GREENLAND ICE SHEET

2.1. Introduction

Surface topographical undulations on length scales comparable to the local ice thickness are thought to be controlled by the bed-to-surface transfer of basal topographical and slipperiness perturbations, which is modulated by ice thickness, basal slip ratio and surface slope (Section 1.2.3). Besides the bed-to-surface transfer, several other factors might also influence surface topographical undulations; e.g. spatial variations in SMB and snow compaction rates (Black and Budd, 1964; Gow and Rowland, 1965; Whillans, 1975; Medley et al., 2015), glacier surges (e.g. Murray et al., 1998), thermal incision of surface streams (Karlstrom and Yang, 2016), and preferential melting beneath surface lakes (Greuell et al., 2002; Lüthje et al., 2006). However, observational evidence remains scarce regarding the relative importance of the different effects which control surface topographical undulations.

A recent extension of Gudmundsson's (2003) bed-to-surface transfer theory by Ng et al. (2018) has enabled testing of the theory on non-uniform – i.e. variable ice thickness, surface slope and basal slip ratio – glacier flowlines. Although limited tests have been carried out on real, non-uniform glacier flowlines (Ng et al., 2018), ice sheet-wide tests on many flowlines are still missing (Section 1.2.2). Hence, I apply the non-stationary transfer theory of Ng et al. (2018) on several thousand equally spaced flowlines of the GrIS. My aim is to test the large-scale applicability of the work of Ng et al. (2018), examine the factors that could affect its accuracy, and explore the key controls on the surface topography of the GrIS (Section 1.3, O1-2).

2.2. Methods

2.2.1. Calculating the transfer of basal variability to the surface on non-uniform glacier flowlines

The transfer of variability in basal topography and slipperiness to the surface of ice masses (Fig. 2.1A) has been mathematically expressed for a parallel, plane-slab ice flow with isotropic rheology and constant viscosity (Gudmundsson, 2003). An extension of calculating this transfer, based on non-stationary convolution and

applicable to 2D (i.e. a 1D flowline of varying ice thickness) flow sections (Ng et al., 2018), allows me to estimate the topographical response of the surface to basal perturbations (i.e. to both topography and slipperiness) when background variables (ice thickness, surface slope and basal slip ratio: sliding velocity / deformational velocity) vary with distance x along individual flowlines. Specifically, if $b(x)$ and $c(x)$ represent the basal topography and slipperiness perturbations respectively, then the Fourier transform of the surface elevation response is given by

$$\hat{s}(k) = \int_{-\infty}^{\infty} T_{sb}(k,x)b(x)e^{-ikx}\,dx + \int_{-\infty}^{\infty} T_{sc}(k,x)c(x)H(x)e^{-ikx}\,dx \quad \text{(Eq. 2.1)}$$

(Ng et al., 2018), where k denotes the wavenumber, $H(x)$ is the background ice thickness and the transfer functions T_{sb} and T_{sc} (reported by Gudmundsson, 2003) vary with the background variables and thus depend on x. The surface response $s(x)$, itself a perturbation superimposed on the background surface elevation profile, is found by computing the inverse Fourier transform of $\hat{s}$:

$$s(x) = \frac{1}{2\pi}\int_{-\infty}^{\infty} \hat{s}(k)e^{ikx}\,dk. \quad \text{(Eq. 2.2)}$$

As flowlines have finite lengths, the integrals are evaluated as discrete sums in the same way as in the Discrete Fourier Transform and its inverse (Ng et al., 2018). In the calculations of the transfer, reported below, I use the particular forms of T_{sb} and T_{sc} given by section 4.9 of Gudmundsson (2003), which were derived from a linearised ice-flow theory assuming constant ice viscosity.

2.2.2. Deriving bed topography and basal slip ratio profiles along ice flowlines

Ice flowlines were derived from a modelled ice surface velocity field of the contemporary GrIS (Price et al., 2017). Their tracing required manual delineation of 5138 seed-points close to the ice divides, to ensure an adequate density of lines for the whole ice sheet. Along each flowline, surface topography, bed topography and basal slip ratio, were sampled at a spacing of 250 m (Fig. 2.1). Surface topography was obtained from the GIMP-DEM (Howat et al., 2014; 2017; 30 m grid resolution), bed topography from the IceBridge BedMachine Greenland, Version 3 dataset (Morlighem et al., 2017a, 2017b; 150 m grid resolution), and basal slip ratio from a dataset by MacGregor et al. (2016).

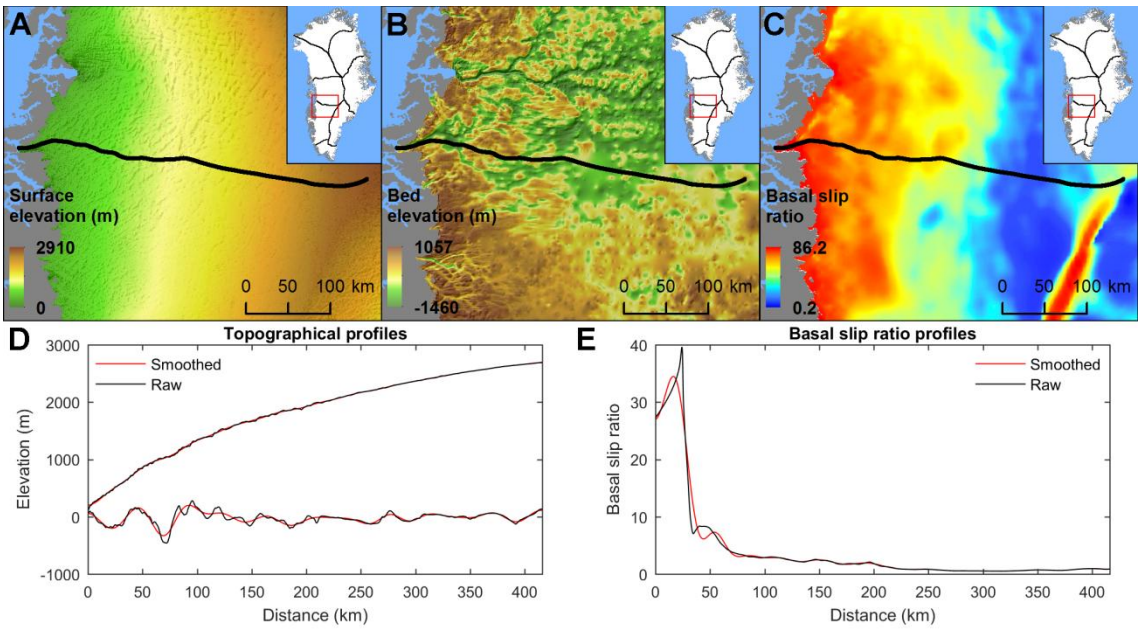

Figure 2.1 (A) Maps of ice surface topography, (B) bed topography (D) and basal slip ratio in SW Greenland, showing a sample flowline (bold curve). (D) Raw profiles of bed and surface elevations, (E) and basal slip ratio derived from the map along the flowline, the corresponding smoothed versions are also plotted. Areas around the ice divides are masked out to minimise edge effects.

This basal slip ratio dataset, calculated by the formula u_s/u_d (u_s: representative surface velocity, u_d: deformational velocity), approximates the true basal slip ratios which are defined in Section 1.2.3 (i.e. sliding velocity / deformational velocity). Generally, true basal slip ratios are underestimated by the calculations of MacGregor et al. (2016) due to overestimation of u_d and underestimation of u_s. The overestimation of u_d arises from the assumption of fully temperate ice throughout the GrIS, and the underestimation of u_s arises from the use of observed winter ice flow velocity to represent annual ice motion, which ignores summer speed-up events (Bartholomew et al., 2010). I conducted sensitivity experiments to assess the effects of u_d overestimation and u_s underestimation on my surface relief predictions (detailed in Section 2.2.7).

2.2.3. Separating background variables and perturbations

Bed topography, ice surface topography and basal slip ratio profiles (Fig. 2.1E-F) were smoothed using a 6th-order Butterworth low pass filter to separate background variables (smoothed data) which determine the strength of the transfer (Fig. 2.2A-C), and basal perturbations (raw minus smoothed data) which are transferred to the surface (Fig. 2.2D). While this subtraction for the bed elevation yielded $b(x)$ directly (Fig. 2.2D), the slipperiness forcing $c(x)$ – defined in the transfer theory as mesoscale perturbations on the coefficient of the basal sliding law (Gudmundsson et al., 1998;

Gudmundsson, 2003) – is unknown, because direct observations/measurements of subglacial properties are lacking. One way of estimating $c(x)$ is to treat the ice flow as an inverse problem for constraining the basal conditions, using knowledge of u_s and the surface topographical undulations as inputs (discussion by Ng et al., 2018), but this difficult problem is not tackled in this thesis. Note that this issue with $c(x)$ does not concern the background slip ratios conditioning the transfer (De Rydt et al., 2013), which are simply derived as the smoothed version of the basal slip ratio dataset. Although $c(x)$ is unknown, theory suggests that its effect on surface topographical undulations may be small compared to $b(x)$ (Gudmundsson, 2003; De Rydt et al., 2013) in many areas (unless $b(x) \approx 0$, on ice streams with exceedingly smooth beds). Hence, here I neglected the second integral of Eq. (2.1) – containing $c(x)$ – in my calculations but nevertheless undertook experiments to assess its potential effects on the surface topography (Section 2.2.6). The observed ice surface undulations, defined by the perturbation $s(x)$ (Fig. 2.2E), were derived by subtracting the smoothed surface topographical profile from its raw version. To predict $s(x)$ (Fig. 2.2E), I carried out the integral method in Eqs. (2.1) and (2.2), using the basal topographical perturbation profiles $b(x)$ and the background profiles as the inputs.

As the linearised transfer theory of Gudmundsson (2003) was derived for a parallel slab flow, the smoothing distance (L) in the Butterworth filter, which determines its corner frequency, should reach or exceed the length-scale at which the shallow-ice approximation (SIA) applies (~10 times the regional ice thickness). However the smoothing distance, which separates the mesoscale perturbations from the long-scale background variables, is not unique (Ng et al., 2018) and its choice is based on two opposing considerations. Greater smoothing distances enable the inclusion of longer surface undulations in the transfer and dampen fast spatial changes in the background variables, ensuring that the approximations behind the use of non-stationary convolution in Eq. (2.1) are applicable (Ng et al., 2018). But greater smoothing distances also retain larger amplitude perturbations, which can invalidate the approximations behind Gudmundsson's (2003) linearised transfer theory (Ng et al., 2018). In order to inform this choice, I experimented with a range of smoothing distances from 5 to 30 km, in steps of 5 km (Section 2.2.5).

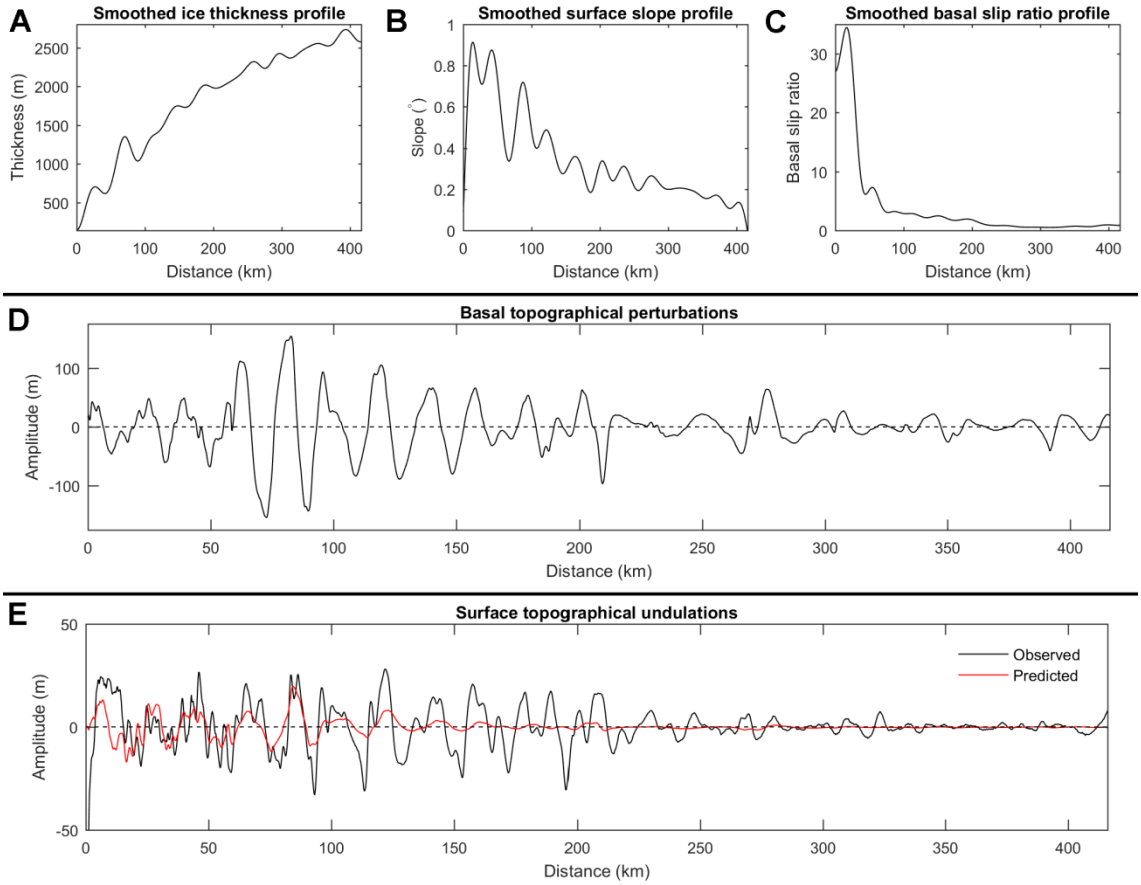

Figure 2.2 Prediction experiment with the flowline in Fig 2.1. Background variables: (A) ice thickness, (B) ice surface slope, (C) basal slip ratio, (D) and basal topographical perturbations. (E) Observed and predicted surface topographical undulations, showing correspondence between some of their peaks and troughs.

2.2.4. Calculating observed and predicted surface relief and relief anomaly

A continuous wavelet transform (CWT - Eq. 2.3) was applied to the observed and predicted surface topographical undulation profiles to study their spectral composition (Fig. 2.3):

$$W_f(p,a) = \int_{-\infty}^{\infty} f(x)\frac{1}{\sqrt{a}}\Psi^*\left(\frac{x-p}{a}\right)dx. \qquad \text{(Eq. 2.3)}$$

Here $f(x)$ is the observed or predicted surface undulation profile, p is the position, a is the scale, Ψ is the mother wavelet for which an analytic Morlet wavelet was chosen (ω_0 = 6), and * represents the complex conjugate (Mallat, 2009; Alessio, 2016). The absolute value of the real part of the continuous wavelet transforms measures the amplitudes of surface undulations at wavelengths below the smoothing distance (Fig. 2.3). Subtracting the observed CWT amplitudes from the predicted CWT amplitudes gives an "anomaly" (Fig. 2.3C) that reveals any under- and overestimation of the amplitude of surface undulations at different wavelengths and positions. Detailed

analysis of all CWT and anomaly plots for the several thousand flowlines across the GrIS was not feasible. Instead, for each flowline, I condensed the plots by averaging their results over the mesoscale range of wavelengths (up to the smoothing distance) to create spatial profiles of observed mean surface undulation amplitude, predicted mean surface undulation amplitude, and mean amplitude anomaly (Fig. 2.3D-F). For brevity, these are henceforth referred to as the observed/predicted mean surface relief and relief anomaly. Linear regression was applied to test the expected 1:1 linear relationship between the observed and predicted mean surface relief along all flowlines simultaneously, testing the overall performance of the method. Colour-coded maps of the whole ice sheet were also produced from the observed/predicted mean surface relief and relief anomaly profiles by kriging interpolation, for visual inspection of spatial patterns and subsequent comparisons. Although maps could also have been made directly from the observed and predicted surface topographical undulation profiles (Fig. 2.2F), their repeated zero crossings would have complicated the spatial analyses. My approach circumvents this problem by first extracting amplitudes in spectral terms.

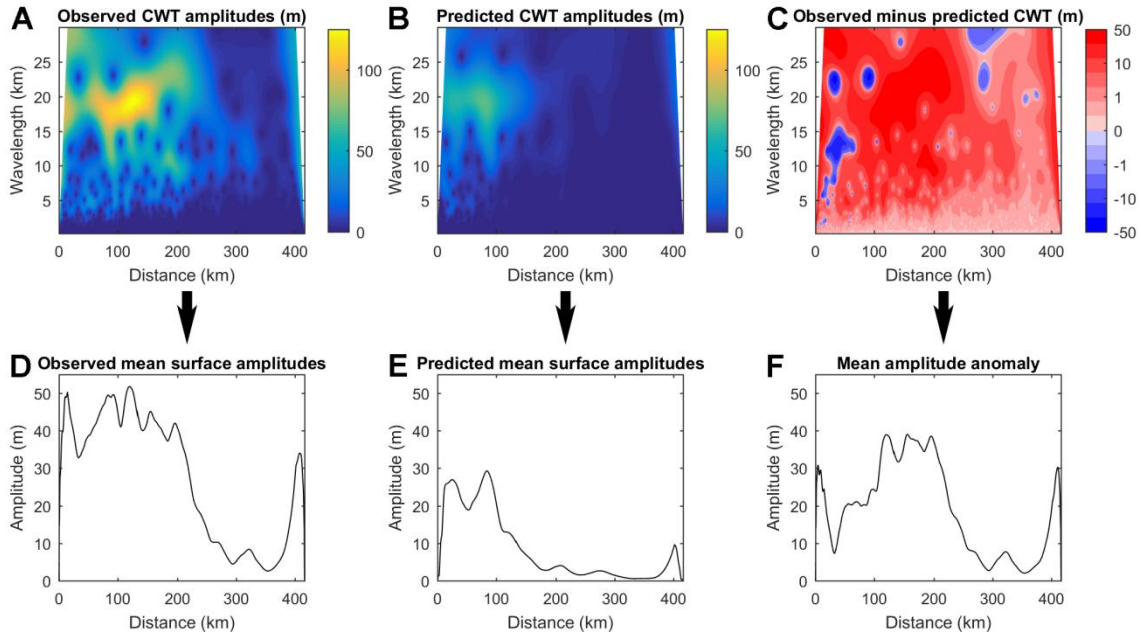

Figure 2.3 (A) Continuous wavelet transforms (CWT) of the observed (B) and predicted surface undulation profiles along the flowline in Fig 1. These "scalograms" show the amplitude (in metres, as indicated by the colour scale panels) of the different wavelength topographical undulations along the profile. (C) Amplitude difference between (A) and (B) is also shown. The lower plots, made by averaging the upper plots over different wavelengths, quantify the (D) observed (E) and predicted mean mesoscale surface undulation amplitudes (F) and the mean amplitude anomaly along the flowline.

The last step was the removal of areas close to the ice divides from the resulting surface relief profiles and maps. This was necessary as uncertain basal slip ratios, caused by poorly constrained flow azimuths (MacGregor et al., 2016), and edge effects

of the Butterworth filter low pass filter and the CWT made the results less reliable close to the ice divides. These regions were masked out manually by identifying areas with anomalously high observed and/or predicted mean surface relief. In general, regions selected for removal were roughly within one smoothing distance of the ice divide.

2.2.5. Deciding the optimal smoothing distance

The smoothing distance (L) – determining the corner frequency of the 6th-order Butterworth low pass filter – used to separate the background variables (determining the strength of the transfer) and the perturbations (which are transferred to the surface) is not unique. My choice of L is based on two opposing considerations described in the second paragraph of Section 2.2.3. Sensitivity tests were carried out to inform this choice. The observed and predicted mean surface relief profiles, derived from the continuous wavelet transforms (CWTs) of the observed and predicted surface topographical undulation profiles, were calculated using L from 5 to 30 km at 5 km intervals. The performance of each L-value was evaluated by linear regression analysis of the relationship between the observed and predicted mean surface relief. In addition, I calculated the mean wavelet coherence for each L, indicating the match between the observed and predicted surface topographical undulation profiles at different wavelengths, by taking the mean of the wavelet coherence matrices calculated along the flowlines.

2.2.6. Estimating the relative response of surface topography to basal slipperiness perturbations

Although the actual basal slipperiness perturbations – $c(x)$ – are unknown, I can estimate the response of the surface topography to $c(x)$ relative to basal topographic perturbations, $b(x)$. As a first approach, I use the equations of Gudmundsson (2003) to calculate the non-dimensional amplitude transfer ratios (the ratio of basal and surface undulation amplitudes) of $c(x)$ and $b(x)$ with a wide range of non-dimensional wavelengths (basal undulation wavelengths scaled to a constant ice thickness, λ/H) for a variety of background basal slip ratios and surface slopes. Using the non-dimensional amplitude transfer ratios, I also investigate the importance of $c(x)$ relative to $b(x)$ in determining surface topography.

The aforementioned calculations only provide additional clarifications within the theoretical framework of Gudmundsson (2003) and thus have limited relevance to my

results. In order to evaluate the surface topographical response to $c(x)$ relative to the response to $b(x)$ in the context of the non-stationary convolution approach of Ng et al. (2018), where the surface relief is calculated from the CWT of surface undulations, I need to conduct further sensitivity tests. As $c(x)$ is dimensionless and scaled to the background ice thickness in Eq. 2.1, it is possible to replace the unknown $c(x)$ in the second integral of Eq. 2.1 with the observed $b(x)$ and skip the scaling. Hence, it is possible to calculate the surface topographical response using the two transfer functions – T_{sb} and T_{sc} within the two integrals of Eq. 2.1 – separately but with the same input forcings. Positive $b(x)$ (i.e. bed bumps) acts as resistance to the ice flow while positive $c(x)$ (i.e. slippery spots) enhances ice flow (Gudmundsson, 2003), thus I replaced $c(x)$ with $-b(x)$ in Eq. 2.1 to ensure that forcings are not just of the same magnitude but the same effective phase as well. After these steps, the mean surface relief due to the bed-to-surface transfer of both $b(x)$ and synthetic $c(x)$ – i.e. $-b(x)$ – was calculated using the approach outlined in Sections 2.2.1-2.2.4. Using these outputs the ratio of predicted mean surface relief due to $b(x)$ and synthetic/potential $c(x)$ could be calculated and analysed under typical ice sheet conditions.

2.2.7. Estimating the consequences of basal slip ratio underestimation

As discussed in Section 2.2.2, the basal slip ratio dataset (MacGregor et al., 2016) generally underestimates true basal slip ratios due to the underestimation of representative surface velocities and the overestimation of deformational velocities. The underestimation of representative surface velocities arises from the use of observed winter ice flow velocity to represent annual ice motion, which ignores summer speed-up events (Bartholomew et al., 2010). Whereas, the overestimation of deformational velocities arises from the assumption of fully temperate ice throughout the GrIS through the usage of a constant creep parameter ($A = 2.4 \times 10^{-24}$ Pa^{-3} s^{-1}) in Eq. (2.4) – associated with temperate ice – across the whole ice sheet (MacGregor et al., 2016).

$$u_d = \frac{2A}{n+1} (\rho_i g H \sin \alpha)^n H \qquad \text{(Eq. 2.4)}$$

where $n = 3$ is Glen's exponent (e.g. Cuffey and Paterson, 2010), $\rho_i = 900$ kg m^{-3} is the ice density, g is the gravitational acceleration (m s^{-2}), H is the ice thickness (m), and α is the along flow ice surface slope. Two sensitivity tests were carried out to quantify how much basal slip ratios may have been underestimated and to approximate the consequences of this for the predicted surface relief outputs.

The first test estimates the consequences of using winter surface velocities. Basal slip ratios were re-calculated using the deformational velocities provided by MacGregor et al. (2016) and observed annual surface velocities derived from standard cross-correlation (e.g. Rosenau et al., 2015) of Landsat 8 images acquired on 6th August 2014 and 25th August 2015 over a 4,205 km^2 area in SW Greenland (A. Sole, personal communication, 2017). This new basal slip ratio dataset was then used to re-predict the surface relief for this area. Comparison of these datasets shows not only the basal slip ratio underestimation due to the usage of winter surface velocities but also the error this might have caused on the predicted surface relief.

The second test – exploring the consequences of the assumption of a fully temperate ice column across the GrIS by MacGregor et al. (2016) – follows the approach of Ng et al. (2018) by considering the actual/likely thermal structure of the GrIS. The creep parameter decreases strongly with decreasing ice temperature; its value is around 10 times smaller at -15°C than at 0°C (Cuffey and Paterson, 2010). MacGregor et al. (2016) used a creep parameter assuming temperate ice (i.e. 0°C), yet around the ice sheet divide much of the ice column is likely to have temperatures of -15 to -20°C (Ng et al., 2018). Therefore, the deformational velocity and thus the basal slip ratio could be underestimated by an order of magnitude in the ice sheet interior. Close to the ice sheet margin the entire ice column could be temperate (Harrington et al., 2015; MacGregor et al., 2016), thus the factor of basal slip ratio underestimation is expected to decrease along the flowlines towards the ice sheet margins. In order to quantify the factor of basal slip ratio underestimation, a profile containing a basal slip ratio correction factor (Eq. 2.5) was constructed along each flowline (Ng et al., 2018):

$$b(x) = b_1 + (b_2 - b_1)\frac{x}{x_{max}} \qquad \text{(Eq. 2.5)}$$

where b_1 and b_2 are the basal slip correction factors at x = 0 (the ice sheet divide) and x_{max} (the ice sheet margin) respectively. Then, the original basal slip ratio profile was multiplied with this profile. The modified basal slip ratio profile was used in the standard procedure to predict surface undulations. Following Ng et al. (2018), I allow b_1 and b_2 to vary independently between 1 and 100, with an increment of 1, and seek their optimal combination yielding the best fit (minimal root-mean-squared error) between the observed and predicted surface undulation profiles. This process was repeated for all of the flowlines.

2.3 Results

2.3.1. The optimal smoothing distance

The bed-to-surface variability transfer calculations require a smoothing distance to separate the short-scale perturbations (which are transferred to the surface) from the long-scale background variables (which determine the strength of the transfer). As the smoothing distance (L) is not unique (Ng et. al, 2018) and all subsequent results are based on its value, I first introduce the results which informed the final choice of L. The linear regression models for all Ls tested – from 5 to 30 km at 5 km intervals – were statistically significant (p-value < 0.01), but their coefficients showed considerable variations (Figs. 2.4 and 2.5). The slope increases with the smoothing distance until 20 km, above which it starts to decrease. The coefficient of determination (R^2) generally increases with increasing smoothing distance. However, it is anomalously high at 5 km and the rate of increase slows down above 20 km, at 30 km the R^2 even decreases slightly. The mean wavelet coherence exhibits a steady increase with L, and (like the R^2) the rate of increase drops down above 20 km (Fig. 2.5).

These R^2 and mean wavelet coherence results show that low smoothing distances yielded a relatively weak match between the observed and predicted surface relief (Fig. 2.5). This matches with my expectations, as short smoothing distances retain fast changes in the background variable profiles, making the approximations used in the non-stationary transfer functions less applicable (Ng et al., 2018). Accordingly, the match between the observations and the predictions improves as L increases, although more slowly above 20 km (Fig. 2.5). This effect is also consistent with the theory, as long smoothing distances yield large amplitude perturbations for which Gudmundsson's (2003) linearised transfer theory is less applicable (Ng et al., 2018).

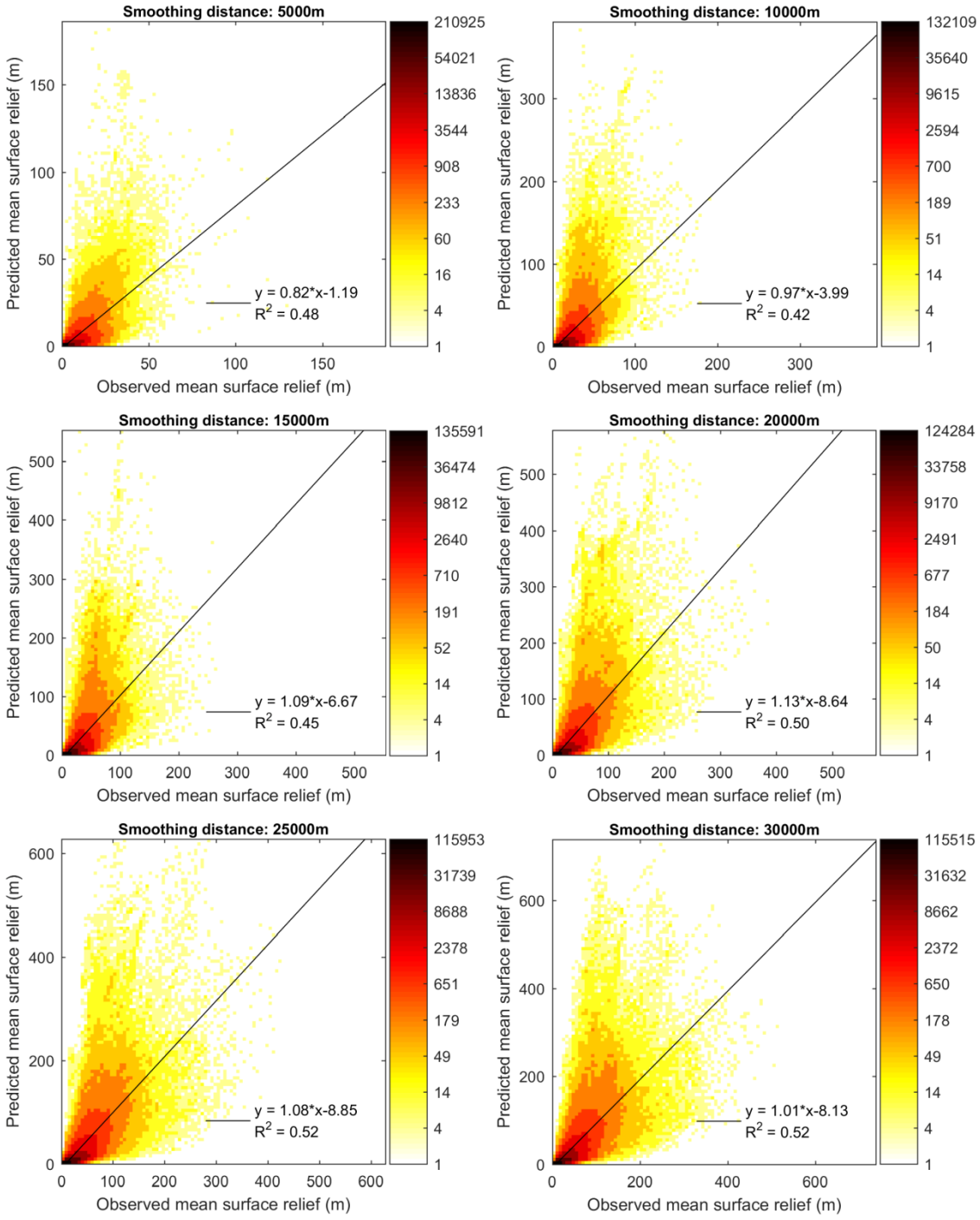

Figure 2.4 Observed and predicted mean surface relief, derived from the continuous wavelet transforms of the surface undulation profiles, are plotted against each other on dot density plots. The colorbars indicate the count of points per pixel. The different smoothing distances used to obtain the results are indicated on the subpanels. Linear trend lines were fitted on the data to test the expected 1:1 linear relationship between the observed and predicted values, the equations and the coefficients of determination (R^2) are also provided.

The slope of the best fit linear equation at 20 km is slightly higher than 1, corresponding to the expected 1:1 linear relationship. However, the local maxima of the slopes and the drop in the rate of change of the R^2 and the mean wavelet coherence (Fig. 2.5) suggest that 20 km is roughly where the two opposing considerations about the

choice of the smoothing distance cancel each other out. Hence, a smoothing distance of 20 km was found to be near-optimal in satisfying both conditions as far as possible, and was therefore used throughout the rest of the thesis. This choice also matches the requirement that the smoothing distance exceeds 10 times the mean ice thickness, which is 1632 m along the flowlines. In conclusion, when carrying out sensitivity tests is not viable, I recommend choosing a smoothing distance which is just above 10 times the mean ice thickness.

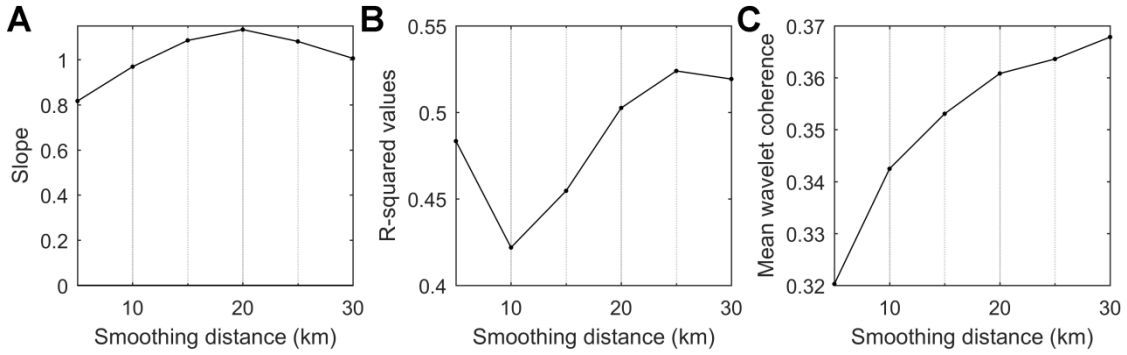

Figure 2.5 (A) The slope, (B) and the coefficient of determination (R^2) which correspond to the linear relationships between observed and predicted mean surface relief obtained using different smoothing distances. (C) The mean wavelet coherence between the observed and predicted surface topographical undulations, calculated along the flowlines obtained using different sommothing distances.

2.3.2. Ice sheet wide observed and predicted mean surface relief

Generally, and as expected, the observed mean surface relief decreases towards the interior of the GrIS, though the rate of decrease shows significant regional differences (Fig. 2.6). Large surface relief is found extending far from the ice sheet margin in the W, NW and NE catchments of the GrIS (Fig. 2.6A) (e.g. on the upstream part of Jakobshavn Glacier and on the Northeast Greenland Ice Stream), where high basal topographical variability (Fig. 2.6C) and basal slip ratios penetrate deep inland (Rippin, 2013; MacGregor et al., 2016) (Fig. 2.6D). In contrast, in the N, E and SW catchments, where such inland penetration is limited (Fig. 2.6C-D), the observed mean surface relief decays quickly away from the margin (Fig. 2.6A). Besides these relationships, there is also a visible spatial correlation between the predicted and observed mean surface relief (Fig. 2.6A-B) confirming the qualitative explanatory power of Gudmundsson's (2003) theory and its non-stationary (i.e. allowing for non-uniform background variables) extension by Ng et al. (2018).

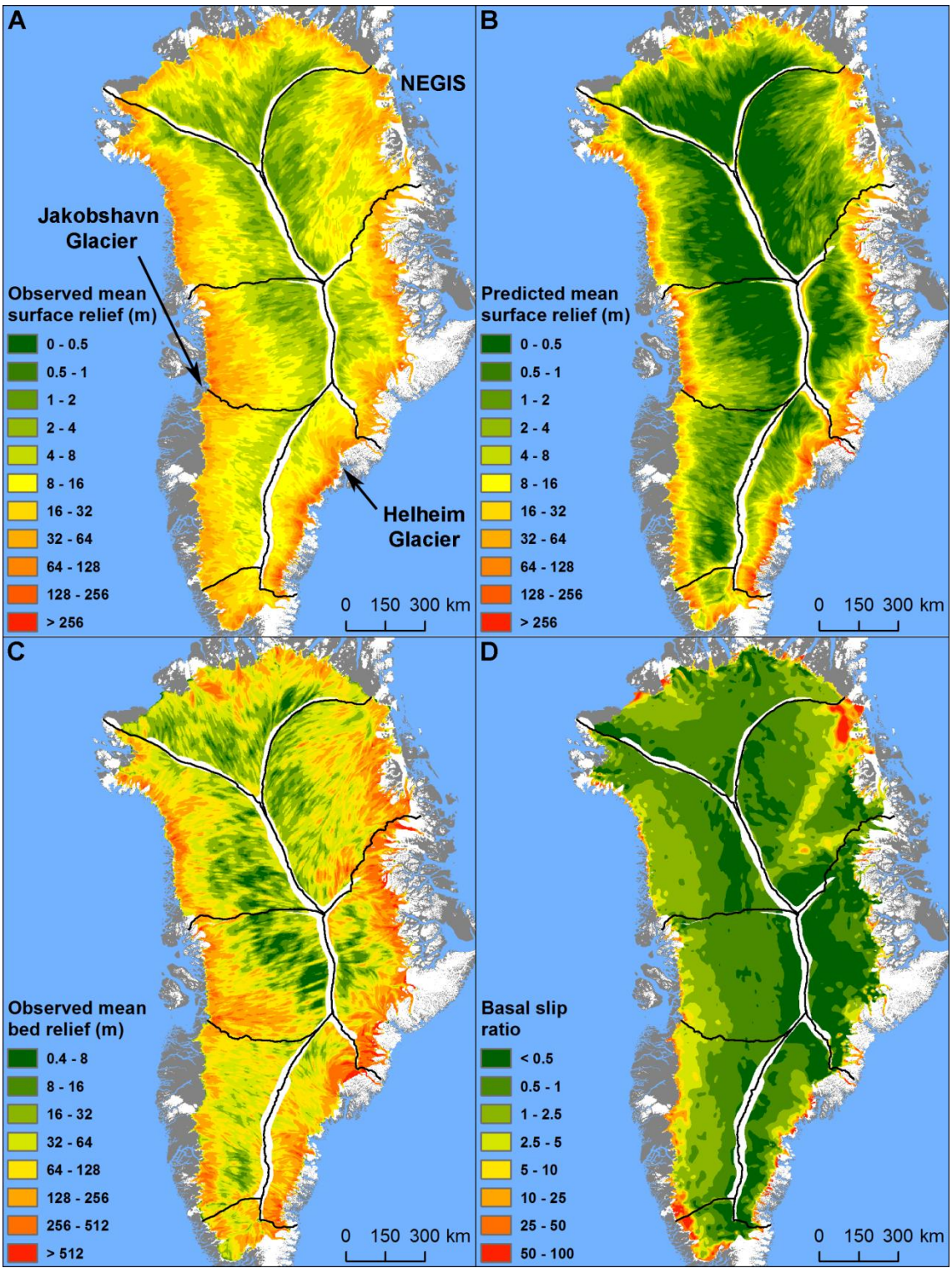

Figure 2.6 (A) Maps of observed mean ice surface relief, (B) predicted mean ice surface relief, (C) observed mean bed relief (D) and basal slip ratio across the GrIS. Areas around the ice sheet divides are masked out to minimise edge effects. The catchments indicated on the subplots were delineated by the Goddard Ice Altimetry Group (Zwally et al., 2012).

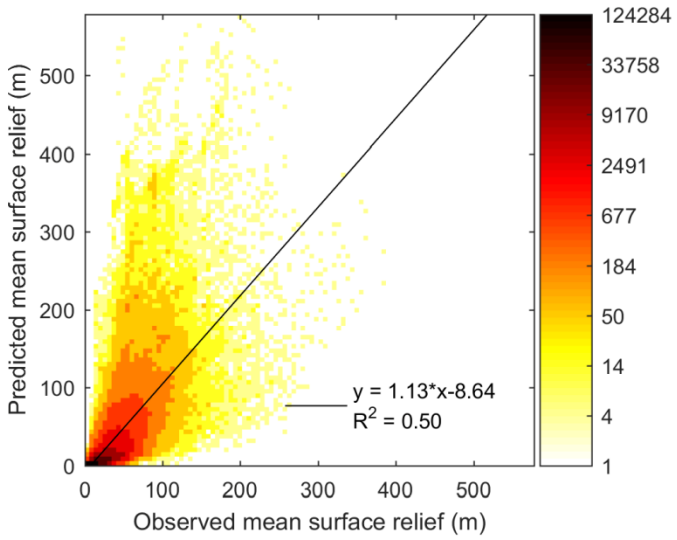

Figure 2.7 Predicted mean surface relief against observed mean surface relief calculated along the flowlines (before interpolation), on a data density plot. The colour bar indicates the number of data points per pixel.

I proceeded to quantify the performance of the method outlined in Eq. (2.1) and Eq. (2.2) in capturing the transfer, whose explanatory power has already been attested by visible correlation between the observed and predicted mean surface relief maps (Fig. 2.6A-B). Linear regression demonstrates a statistically significant (p-value < 0.01) relationship between these relief variables (Fig. 2.7), with the best-fit equation (slope = 1.13; intercept = -8.64) deviating slightly from perfect match (slope = 1; intercept = 0). Despite this impressive result and the qualitative spatial correlation (Fig. 2.6A-B), which indicates general success of the method, there is a considerable mean absolute error (14.9 m) between the observed and the predicted mean surface relief. Additional insights come from the map of relief anomaly (i.e. spectral-mean difference between observed and predicted CWT amplitudes), which reveals systematic patterns in the amount of underestimation (positive anomaly) or overestimation (negative anomaly) of the predictions across Greenland (Fig. 2.8B). The frequency distribution of the relief anomaly is bi-modal, with one modus at +8 m and another at -16 m (Fig. 2.8C). Most of the ice sheet (92.5%) is characterized by underestimation, while overestimation is restricted to numerous small areas close to the margins (Fig. 2.8A-C). These negative anomalies often correspond with the high absolute principal strain rates on fast-flowing outlet glaciers (Fig. 2.8C-E, G-H).

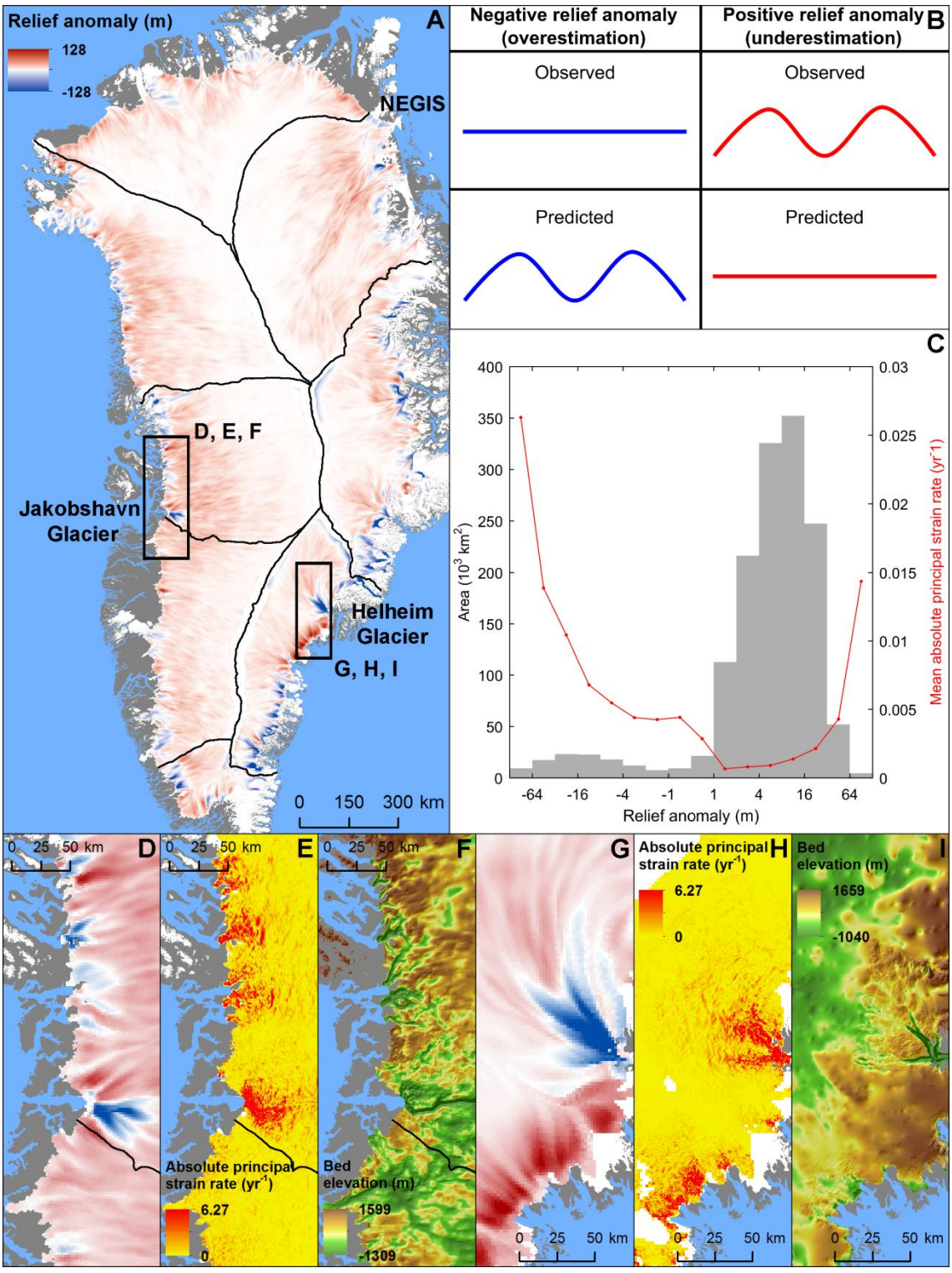

Figure 2.8 (A) Map of surface relief anomaly across the GrIS. (B) Cartoon of surface topography explaining what the two types of relief anomaly. The anomaly is negative (blue) where the observed relief is less than predicted, and positive (red) where it is more than predicted. (C) Ice sheet-wide frequency distribution of relief anomalies and the corresponding means of the absolute principal strain rates, categories smaller than 4500 km^2 have been removed and accordingly the colour scale was capped on panel (A). (D, G) Relief anomaly, (E, H) absolute principal strain rate (F, I) and bed topography in the two regions outlined by the boxes in (A).

2.3.3. The relative response of surface topography to basal slipperiness perturbations

I quantified the relative surface response to potential basal slipperiness perturbations – even though the actual perturbations are unknown – using two sensitivity tests discussed in Section 2.2.6. The first test utilized the transfer equations of Gudmundsson (2003) directly in order to calculate non-dimensional amplitude transfer ratios of $c(x)$ and $b(x)$, which differ significantly – especially – at short wavelengths and high background basal slip ratios (Fig. 2.9A-B). Although Gudmundsson (2003) discussed this in detail, the relative surface topographical response to $c(x)$ and $b(x)$ has received less attention. My calculations demonstrate that the relative surface topographical response to $c(x)$ is well below 0.2 – compared to the surface topographical response to $b(x)$ – when the non-dimensional wavelengths (λ/H) of basal perturbations are lower than 5-10 (Fig. 2.9C-D). Basal slipperiness perturbations with longer wavelengths and/or under thinner ice (around $\lambda/H > 10$) have a larger relative effect on the surface topography (between ~0.2 and ~0.5) though even in the case of very large λ/Hs the ratio does not approach unity (Fig. 2.9C-D). The relative surface topographical response to $c(x)$ increases with background slip ratios when basal perturbations have λ/Hs above ~10, whereas background slip ratios have the opposite effect when basal perturbations have lower λ/Hs (Fig. 2.9C-D). It is also interesting that surface slope does not affect the relative surface topographical response to $c(x)$ (Fig. 2.9C-D). In conclusion, the theory of Gudmundsson (2003) suggests that the relative surface topographical response to $c(x)$ is the highest when basal perturbations are relatively long – above 20 times the local ice thickness – and background slip ratios are high. However, this ratio remains below 0.5, even for the most favourable conditions (Fig. 2.9C-D).

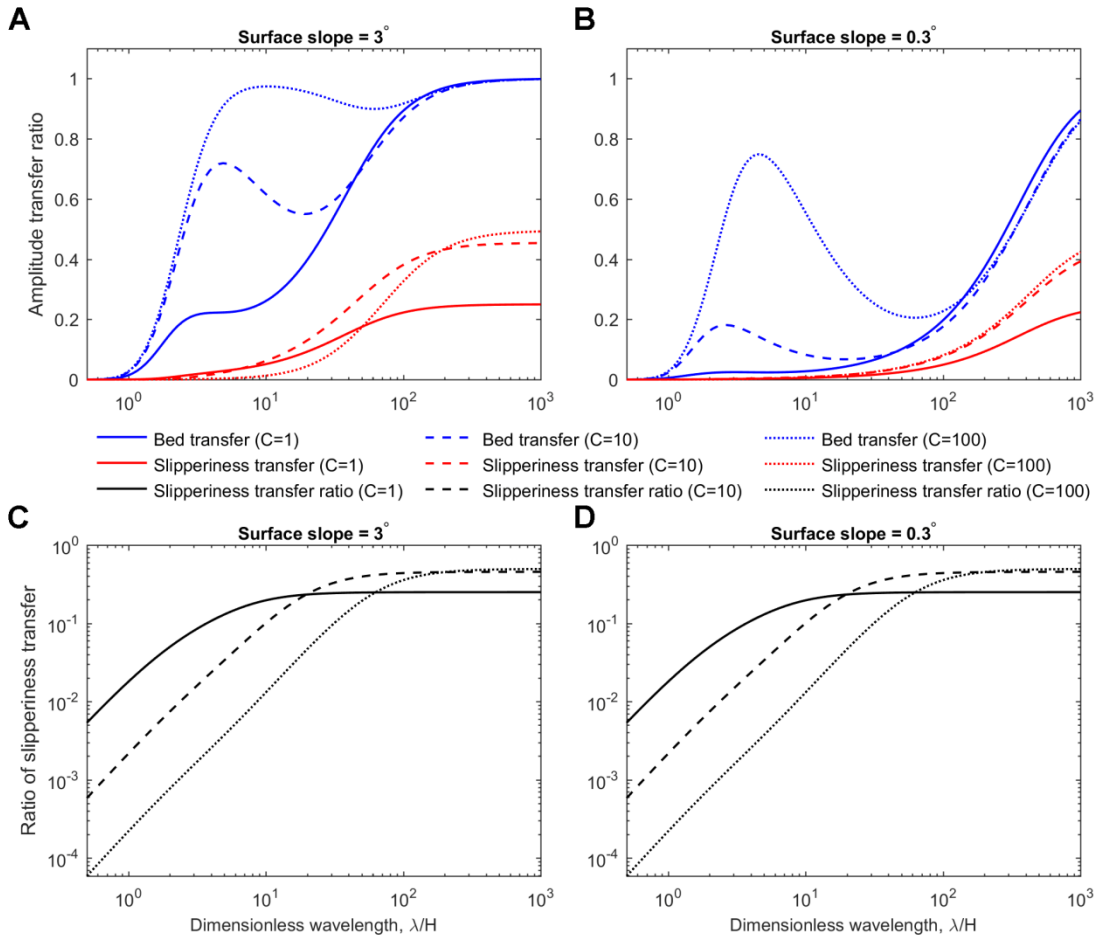

Figure 2.9 (A-B) Non-dimensional amplitude transfer ratios of b(x) (blue lines) and c(x) (red lines) for a wide range of non-dimensional wavelengths and background slip ratios (C = 1, 10 and 100; solid dashed and dotted lines respectively) and surface slopes (3° and 0.3° for (A) and (B) respectively). (C-D) Surface topographical response to $c(x)$ relative to the response to $b(x)$ (black lines), using the same parameters as on panels (A) and (B).

Results of the second sensitivity test, which employs the approach to calculate surface relief (Section 2.2.1-2.2.4) in addition to Gudmundsson's (2003) transfer equations, support the findings above. The relative response of surface relief to synthetic $c(x)$, which has the same magnitude and effective phase as $b(x)$, is low in the interior of the ice sheet (< 0.15), where ice is thicker and basal wavelengths have lower λ/H (Fig. 2.10). Closer to the margins, where ice is thinner and λ/H higher, the relative effect of $c(x)$ on surface relief is greater, though still predominantly below 0.3 (Fig. 2.10). The effects of background slip ratios on the relative surface relief response to synthetic $c(x)$ are less obvious. However, the general increase in basal slip ratios towards the margins of the ice sheet (Fig 2.6D), where λ/Hs are higher, could contribute to the increase in the relative surface relief response. It is also interesting that the relative surface relief response to synthetic $c(x)$ is especially low on the Northeast Greenland Ice Stream, Jakobshavn Glacier, Helheim Glacier in SE Greenland and other

major outlet glaciers (Fig. 2.10). This supports the theoretical expectation that bed topography exerts a dominant control on the surface topographical undulations on ice streams (Gudmundsson et al., 1998; Gudmundsson, 2003; De Rydt et al., 2013). However, I also suggest that a key precondition is the presence of relatively thick ice (Figs. 2.9 and 2.10). In conclusion, the relative surface relief response to $c(x)$ is expected to be highest close to the margins, where the ice is thin and the basal slip ratio high. However, even here this ratio – relative to $b(x)$ – is below 0.3-0.4, and more typically 0.1-0.3. Hence, I propose that the response to $c(x)$ from the total surface relief response to $b(x)$ and $c(x)$ remains well below <25% in most cases, provided that the amplitudes of $c(x)$ are not significantly larger than those of $b(x)$.

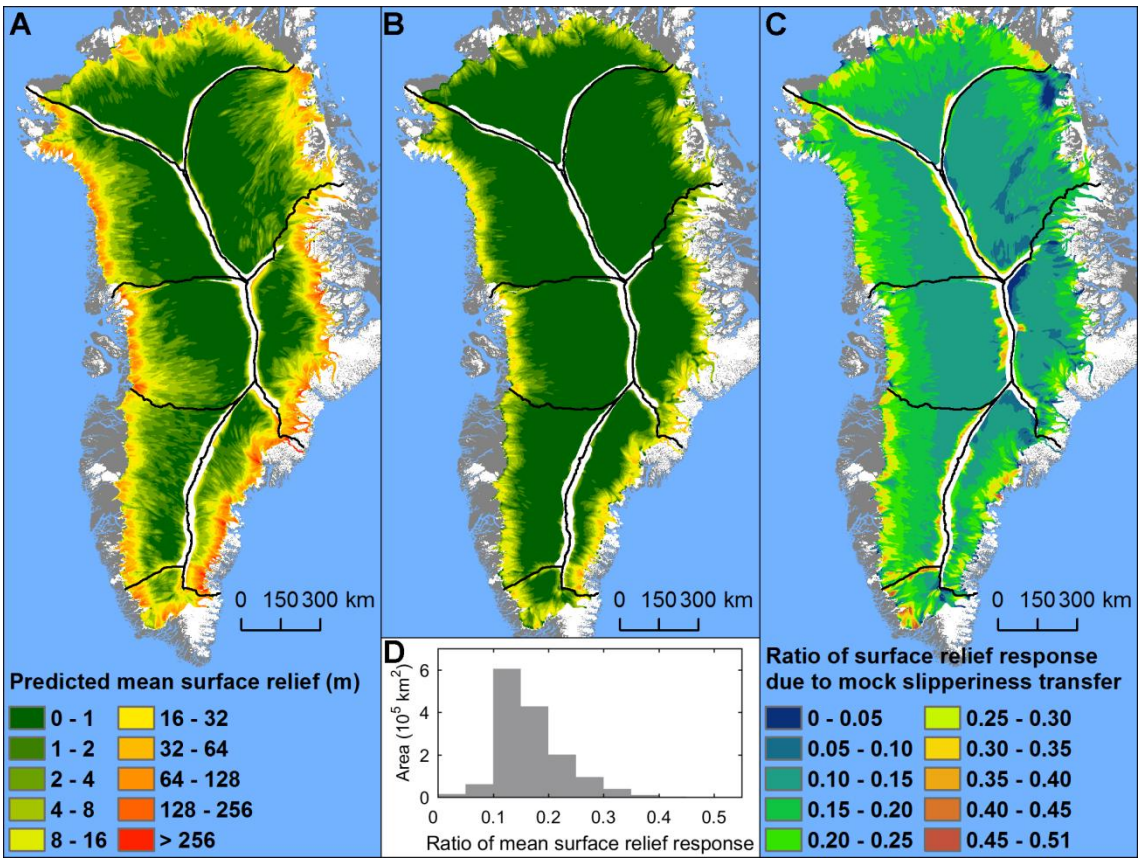

Figure 2.10 (A-B) Predicted mean surface relief response to $b(x)$ and synthetic $c(x)$, respectively. (C-D) A map and a histogram, respectively, showing the relative predicted mean surface relief response to synthetic $c(x)$ compared to the response to $b(x)$.

2.3.4. Basal slip ratio underestimation and its effects on the predicted mean surface relief

The basal slip ratio dataset provided by MacGregor et al. (2016) generally underestimates true basal slip ratios (Section 2.2.2 and 2.2.7). To quantify the consequences of this on the predicted mean surface relief datasets I have carried out two sensitivity tests, discussed in Section 2.2.7. The first sensitivity test shows that the usage of winter velocities as representative surface velocities underestimated the basal slip ratios within SW Greenland by a mean relative difference of 18.6%, as summer ice flow speed-ups were neglected (Fig. 2.11). However, my tests also demonstrate that this only caused a relatively moderate underestimation – with a mean relative difference of 6.6% – of the predicted mean surface relief (Fig. 2.11).

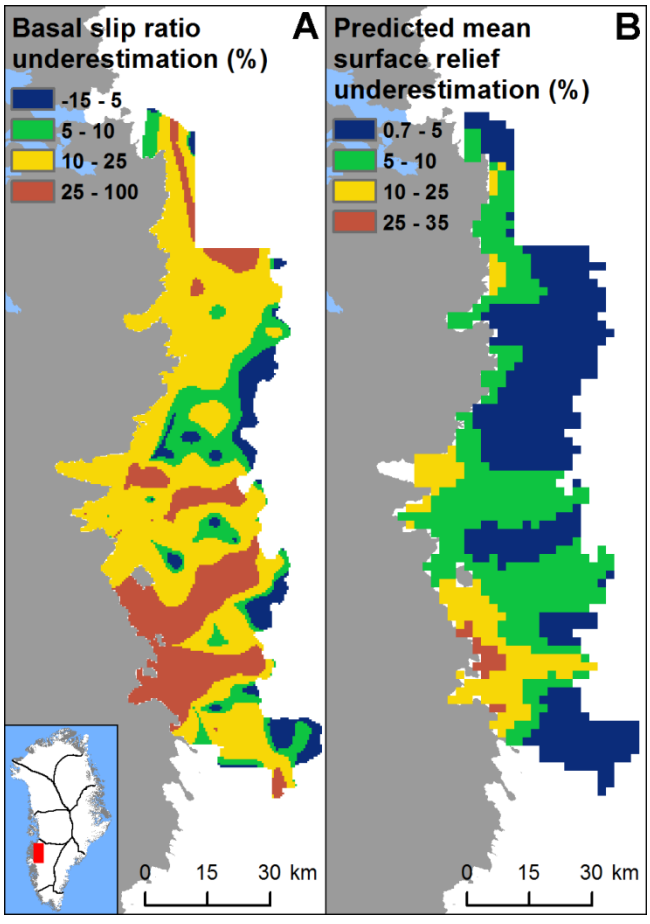

Figure 2.11 (A) The percentage of the basal slip ratio underestimation caused by the usage of winter, instead of annual, ice flow velocities, (B) the underestimation of the predicted mean surface relief caused by the usage of winter, instead of annual, basal slip ratios.

The output of the second sensitivity test, the optimal basal slip ratio correction factor (*b*) – offsetting the underestimation of the basal slip ratio due to the assumption of fully temperate ice (Section 2.2.7) – shows a marked tendency to increase towards

the ice sheet divide (Fig. 2.12). Although 100 was prescribed as the maximum possible correction factor (Section 2.2.7), it rarely attains this and usually remains below 20-25 and 40-50 around the ice sheet divide in SW-NE and in N Greenland, respectively (Fig. 2.12A). This increasing pattern towards the ice divide is less clear in other sectors of the ice sheet, most notably in the SE sector of the GrIS where the correction factor not only increases towards the margin but also attains unusually high values (Fig. 2.12A). It is also striking that the correction factor is 1 over large areas of the GrIS, extending all the way up to the ice divide (Fig. 2.12A). In these areas, a larger basal slip ratio would increase the overall mismatch between the observed and predicted surface undulations along the flowlines.

Generally, the predicted mean surface relief is underestimated – especially in the SE of the ice sheet – due to the assumption of a fully temperate ice column across the whole GrIS (Fig. 2.12B). However, the large-scale pattern of the predicted mean surface relief has not been modified significantly due to this effect (Fig. 2.6). Instead, the basal slip optimisation just dampened the rate of predicted relief decrease towards the interior of the ice sheet in most cases (Fig. 2.12B). Regions where large surface relief has been predicted (and observed) far from the ice sheet margin using the original basal slip ratio dataset – e.g. NW, W, NE (Fig. 2.6) – have even higher predicted relief with the optimised basal slip ratio dataset (Fig. 2.12B). However, the coverage and position of these regions have not changed significantly and new regions with similar characteristics have not been detected (Fig. 2.12B). However, I also note that the highest increase in the predicted surface relief has been observed close to the ice sheet margin in SE Greenland, coinciding with the unusual inverse pattern of the basal slip correction factors (Fig. 2.12B).

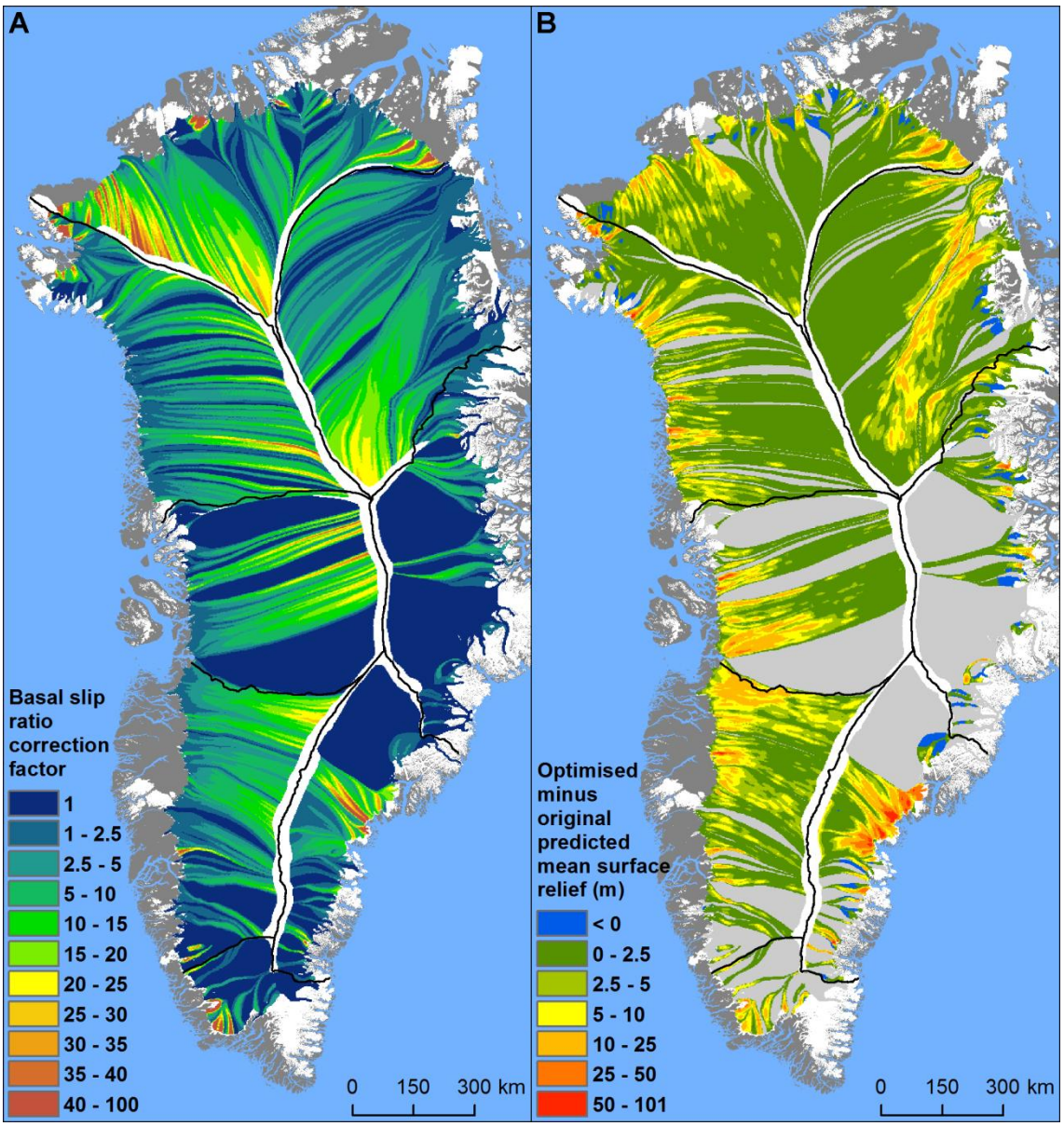

Figure 2.12 (A) Basal slip ratio correction factor (*b*) map. (B) The difference between the predicted mean surface reliefs calculated using the original and the optimised basal slip ratios was only calculated where the correction factor was larger than 1. Regions where the correction factor was below 1 are masked out (pale grey).

2.4. Discussion

2.4.1. Factors controlling the transfer of basal variability to the ice sheet surface

The overall decrease of the observed mean surface relief towards the interior of the GrIS (Fig. 2.6) confirms the theoretical expectation that the transfer of basal topographical and slipperiness variability to the ice sheet surface is attenuated by thicker ice and lower ice surface slopes (Gudmundsson, 2003; Raymond and Gudmundsson 2005). The visible correlation between high observed mean surface relief and high basal slip ratio also confirms the theoretical expectation that high basal slip ratio enables more

efficient basal variability transfer to the surface (Gudmundsson, 2003; Raymond and Gudmundsson 2005). Finally, the correlation between the predicted and observed mean surface relief confirms that the theory of bed-to-surface variability transfer (Gudmundsson, 2003) and its non-stationary extension (Ng et al., 2018) could be used to estimate the topographical variability of the ice sheet surface using currently available datasets in Greenland.

According to the transfer functions T_{sb} and T_{sc}, the surface topographical response to basal slipperiness perturbations is significantly weaker than the response to basal topographical perturbations across the GrIS at the wavelengths investigated (Gudmundsson, 2003; De Rydt et al., 2013; Ng et al., 2018). In other words, the surface topographical relief is controlled predominantly by basal topographical perturbations, i.e. via T_{sb} in Eq. (2.1), while the ice thickness, basal slip ratio and surface slope modulate this control. This theoretical expectation is confirmed by my sensitivity experiments, showing the relative surface response to potential basal slipperiness perturbations of the same magnitude and phase as the observed basal topography perturbations (Section 2.2.6). These demonstrate that the relative mean surface relief response to potential basal slipperiness perturbations – compared to the total surface relief response – is below 25% for typical GrIS conditions today, assuming similar magnitude basal topography and slipperiness perturbations (Section 2.3.3). The fact that the predicted mean surface relief – calculated neglecting the bed-to-surface slipperiness transfer – reproduces the large-scale spatial pattern of the observed mean surface relief (Fig 2.6) also supports the dominance of basal topographic perturbations in controlling the surface relief. However, the exclusion of the bed-to-surface slipperiness transfer could explain – to some extent – the general underestimation of the observed mean surface relief by the predicted relief dataset.

2.4.2. Factors affecting the accuracy of the predicted mean surface relief

The qualitative explanatory power of the theory – and the numerical implementation – has been confirmed by the good visible correlation and the reasonable linear relationship between the observed and predicted mean surface relief (Fig. 2.6). However, there are considerable quantitative differences between the observed and predicted mean surface relief (Section 2.3.2). Predominantly the mean surface relief of the GrIS was underestimated (i.e. positive relief anomaly), while in some smaller regions overestimation (i.e. negative relief anomaly) was also observed (Fig. 2.8).

The exclusion of the bed-to-surface slipperiness transfer may explain some of the positive relief anomaly and why this is dominant across the GrIS. However, it is likely that the surface relief response to basal slipperiness perturbations is small compared to the surface relief response to basal topographical perturbations (Section 2.3.3). Therefore, I suggest that it is unlikely that the observed positive relief anomaly is entirely caused by the exclusion of the bed-to-surface slipperiness transfer. Furthermore, this exclusion cannot produce negative relief anomaly. Hence, I discuss several other reasons that may offer additional explanation for the overall mismatch between the predicted and observed surface relief, and to the spatial pattern of the relief anomaly.

2.4.2.1. Spatial variations in the surface mass balance and snow/firn compaction rates

Firstly, my method is based exclusively on the transfer theory, thus other surface relief production processes are not incorporated. For example, redistribution of snow/firn on the ice sheet surface by strong winds can cause sastrugi to form, which could not be captured by the transfer theory. However, these are transient and have relatively small amplitude and wavelength, thus they only mildly increase the surface relief (Whillans, 1975). Spatial variations in surface mass balance and snow/firn compaction rates can also modify the shape of larger surface topographical undulations, which initially form due to the bed-to-surface transfer of basal variability. However, these processes are unlikely to affect the position and phase of these larger undulations significantly (Black and Budd, 1964; Gow and Rowland, 1965; Whillans, 1975; Medley et al., 2015). Hence, I propose that surface processes only exert a secondary feedback on the magnitude of surface relief. This is supported by the fact that I can predict the pattern of surface relief well without incorporating their effects.

2.4.2.2. Basal slip ratio underestimation

Some of the mismatch between predicted and observed mean surface relief is attributable to overall underestimation of the true basal slip ratios due to the assumption of fully temperate ice and the exclusion of summer ice-flow accelerations (Section 2.2.7). This would cause an underestimation of the surface relief, as faster basal slip promotes efficient transfer of basal variability (Gudmundsson, 2003); indeed, most of the ice sheet is characterized by positive relief anomalies (Fig. 2.8).

My results demonstrate that the exclusion of summer speed-up events from representative surface velocities (MacGregor et al., 2016) causes considerable basal slip ratio underestimation (around 18.6%) while the resulting reduction of the predicted mean surface relief is moderate (around 6.6%). However, this test was carried out very close to the ice sheet margin in SW Greenland (Fig. 2.11) and even within this area the underestimation, especially in the case of predicted mean surface relief, increases towards the margin (Fig. 2.11). Thus, underestimation of the basal slip ratio, and especially the predicted mean surface relief, due to the exclusion of summer ice-flow acceleration events is likely to be negligible further inland.

The optimal basal slip ratio correction factors show that the basal slip ratio underestimation – due to the assumption of temperate ice across the GrIS – generally increases towards the ice sheet divide (Fig. 2.12). This agrees well with the assumption that the ice is colder further inland. Furthermore, especially in SW Greenland, the value of the correction factor roughly falls in the range of what I expect due to the decreasing ice temperature and creep parameter, which could be more than 10 times smaller near the ice divide than around the margin of the ice sheet (Cuffey and Paterson, 2010; Harrington et al., 2015; Ng et al., 2018). The maximum correction factors, which are found near the ice divides, also increase towards the north (Fig. 2.12A) where the ice is colder compared to lower latitudes (Rignot and Mouginot, 2012).

However, the increasing trend of correction factors towards the ice divide is not clear everywhere across the ice sheet. Most notably the optimal basal slip ratio correction factor was found to be 1 over large areas, extending from the ice sheet margin to the ice divide (Fig. 2.12A). These areas correspond to flowlines which intersect major negative relief anomalies (Figs. 2.12A and 2.8), where the observed surface relief is significantly overestimated by the predicted relief, even before artificially increasing the basal slip ratio. Thus, increasing the basal slip ratio any further will just raise the overall mismatch between the observed and predicted undulations along these flowlines, due to the more effective transfer of basal variability at high basal slip ratios (Gudmundsson, 2003). In some cases, the correction factor rises towards the sheet margin, instead of increasing towards the ice divide. This is most evident in SE Greenland (Fig. 2.12) and corresponds to areas where the relief anomaly is strongly positive (Fig. 2.8). Thus, I propose that in these cases the correction factor compensates for the underestimation of the surface relief, e.g. due to unknown or poorly resolved basal features.

In conclusion, my results show that the predicted surface relief decreases more rapidly towards the ice sheet divides of the GrIS due to the assumption of fully temperate ice. This also contributes to the overall underestimation of observed surface relief. However, my standard prediction still captures the large-scale spatial pattern of the observed mean surface relief (Fig. 2.6). Hence, even though the ice sheet-wide calculation of basal slip ratio correction factors provided useful insights, they will not be used in subsequent analyses due to their incoherent spatial pattern discussed above.

2.4.2.3. Constant viscosity assumption

A further potential cause of the systematic spatial pattern of over- and underestimation of surface relief is the assumption of constant viscosity – linear stress-strain relationship (i.e. linearly viscous medium) – in the transfer calculation (Gudmundsson, 2003; Ng et al., 2018). Where strain rates are high, the ice viscosity decreases according to Glen's flow law (Fig. 2.13). The attendant faster internal deformation would more strongly attenuate the upward transfer of basal perturbations, causing a smoother surface than predicted. This hypothesis is supported by the correspondence of negative relief anomalies with high strain rate magnitudes, mostly in the vicinity of high velocity outlet glaciers (Fig. 2.8). Where strain rates are low, more rigid ice than assumed (Fig. 2.13) would act as a stress guide to cause stronger transfer (Raymond and Gudmundsson, 2005). This expectation is consistent with the dominance of positive anomalies in the ice sheet interior (Fig. 2.13). However, such nonlinear rheological effects mainly change the quantitative strength of the bed-to-surface transfer, not its qualitative pattern (Raymond and Gudmundsson, 2005). This is supported by the overall correlation between the observed relief map and the predictions.

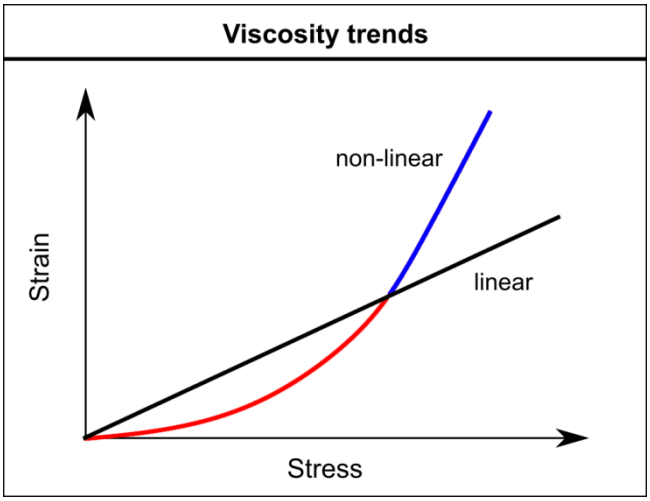

Figure 2.13 Stress-strain graphs of a linearly viscous medium, assumed by the theory, and a non-linearly viscous shear-thinning medium, which is a more precise representation of glacier flow. Negative relief anomalies (blue) are suggested to correspond with areas where the linear approximation overestimates viscosity, at high stress-strain rates, and vice versa (red).

2.4.2.4. Uncertainties of the bed topography and three-dimensional effects on the transfer of basal variability

Other factors responsible for the relief anomalies are bed DEM uncertainty, 3D effects on the transfer of basal variability and the presence of deeply incised subglacial valleys. The BedMachine mass conservation algorithm is less precise (Morlighem et al., 2014, 2017b) and basal topographical features could be missed (Ross et al., 2018), where the spatial density of ice thickness measurements is low. My method will under-predict the amplitude of surface undulations in such data-sparse regions. Accordingly, I observe the dominance of positive relief anomalies in the GrIS interior (Fig. 2.8) where ice thickness measurements are scarce (Morlighem et al., 2014, 2017b). Also, De Rydt et al. (2013) demonstrated that the actual 3D transfer of basal variability is weaker than described by the 2D approximations along flowlines. This "dampening" effect, which would induce negative relief anomalies, is expected to be significant around laterally-confined ice flow features that show strong lateral variations in basal properties (Sergienko, 2012; De Rydt et al., 2013). The effect is evidenced by the frequent alignment of deeply incised subglacial valleys with the computed negative relief anomalies, e.g. the Jakobshavn Glacier in W Greenland and the Helheim Glacier in the SE (Fig. 2.8D-F, G-I). SE Greenland is especially interesting, as strongly positive amplitude anomalies aligned with high strain rates and a disconnected system of subglacial depressions are found directly inland of deep fjords along the ice sheet

margin (Fig. 2.8G-I). I propose that areas such as this have poorly resolved bed topography and overlie yet undiscovered major subglacial valleys.

2.5. Summary

It is possible to predict the large-scale pattern of surface relief on the GrIS from ice sheet-wide bed topography, ice thickness and basal slip ratio datasets, by using a non-stationary integral method (Ng et al., 2018) employing Gudmundsson's (2003) linearised transfer functions. The mismatch found between the observed and predicted surface relief – or 'relief anomaly' – arises from unknown basal slipperiness variations, uncertainties of the bed topography and basal slip ratio datasets, surface processes on the ice sheet, the assumption of a linearly viscous medium, and 3D effects on the transfer of basal variability. The spatial pattern of the relief anomaly is consistent with the expected consequences caused by the assumption of linearly viscous fully temperate ice, the precision of the bed DEM and the 2D approximations of the transfer of basal variability. My results also suggest that surface processes, basal slipperiness perturbations and the seasonal variability of ice flow exhibit only a secondary influence on mesoscale surface topographical undulations.

CHAPTER 3: SPATIAL CORRELATION OF SURFACE RELIEF AND SURFACE DRAINAGE ON THE GREENLAND ICE SHEET

3.1. Introduction

Surface topography is believed to be the first order control on the spatial structure of surface drainage (e.g. Lüthje et al., 2006; Banwell et al., 2012; Leeson et al., 2012; Joughin et al., 2013; Karlstrom and Yang, 2016), while meltwater production and runoff – i.e. exogenic controls – determine the seasonal evolution (e.g. Lüthje et al., 2006; Leeson et al., 2012; Lampkin and VanderBerg, 2014; Clason et al., 2015; Poinar et al., 2017) (Section 1.2.2). Despite some inaccuracies, the large-scale spatial pattern of surface relief can be predicted using the non-stationary extension of Gudmundsson's (2003) transfer theory (Chapter 2). This supports the hypothesis that the bed-to-surface transfer of basal variability is the main control on the surface topography of the GrIS at scales comparable to the local ice thickness (Section 1.2.3). Therefore, bed-to-surface transfer – an endogenic control – might also influence the large-scale spatial structure of surface drainage. Accordingly, I also hypothesise that the non-stationary transfer theory can be used to infer the large-scale spatial structure of surface drainage. Although this aligns well with previous suggestions and observations about the control of basal topography on surface drainage (e.g. Lampkin and VanderBerg, 2011; Karlstrom and Yang, 2016) (Section 1.2.2), it is still unclear whether the scales at which bed-to-surface transfer controls surface topography (Chapter 2) are relevant to the routing of surface meltwater. As this has not been tested before (Section 1.2.2), here I examine the correlation between the spatial structure of surface drainage and the predicted/observed surface relief calculated in Chapter 2, and also explore whether surface runoff modulates the correlation (Section 1.3, O3).

Besides the direct feedback surface drainage exerts on the SMB (e.g. Greuell et al., 2002; Lüthje et al., 2006) (Section 1.1), the spatial structure – and of course the seasonal evolution – of surface drainage also controls the location and characteristics of surface-to-bed meltwater connections (Selmes et al., 2011; Kingslake et al., 2015; Smith et al., 2015; Yang and Smith, 2016), which in turn influence the evolution of subglacial drainage (e.g. Banwell et al., 2016) (Section 1.1). Therefore, understanding the factors that control the spatial structure of surface drainage on the GrIS – i.e. the distribution, density and dimensions of lakes, streams and moulins – is a prerequisite for evaluating

the long-term effects of hydrological processes on GrIS mass balance and dynamics (Section 1.1, Section 1.2.2).

3.2. Methods

3.2.1. Surface lakes, rivers and moulins derived from satellite imagery

To evaluate the influence of the bed-to-surface variability transfer on the surface drainage structure of the GrIS, I compared the observed and predicted mean surface relief with the observed distribution (i.e. derived from satellite imagery) of surface lakes, surface rivers and moulins in the ablation zone of the ice sheet in SW Greenland. These features were derived from Landsat-8 panchromatic imagery – with 15 m horizontal resolution – acquired on 19 August 2013 for a 22,788 km^2 area in SW Greenland by Yang and Smith (2016). I note that moulins were delineated indirectly by Yang and Smith (2016), by assuming a moulin at the end of every surface river which did not terminate in a surface lake.

In order to control for the influence of surface meltwater runoff on the distribution of surface drainage features derived from Landsat-8 imagery, modelled monthly runoff data from Modèle Atmosphérique Régional (MAR, version 3.5.2; 5 km grid resolution) – forced by European Centre for Medium Range Weather Forecast Re-analysis (ERA-Interim) – were obtained for August, 2013 (Fettweis et al., 2013, 2017).

3.2.2. Deriving potential surface lakes, rivers and moulins from surface DEMs and ice flow velocity datasets

The Landsat-8 derived datasets of Yang and Smith (2016) only provide a one-day snapshot of the temporal evolution of the surface drainage in SW Greenland. In reality, surface drainage evolves in time as meltwater production varies across the ice sheet, governed by changing atmospheric conditions and surface energy balance (Yang and Smith, 2016). Therefore, I estimated the maximum potential distribution of lakes, rivers and moulins by delineating closed surface depressions (Section 3.2.2.1), surface rivers (Section 3.2.2.2) and moulins (Section 3.2.2.3) from high-resolution surface DEMs that overlap with the domain of the Landsat-8 survey in SW Greenland.

Crucially, this approach also allows me to carry out ice sheet-wide comparisons of the observed/predicted surface relief and potential surface lake, river and moulin sites, even where the formation of such drainage features is inhibited due to current

atmospheric conditions (e.g. in the interior of the GrIS where surface runoff is currently negligible). However, it is important to note that a more indirect approach – using ice flow velocity instead of a surface DEM – is necessary to create an ice sheet-wide dataset indicating potential moulin sites (discussed in Section 3.2.2.3).

3.2.2.1. Potential surface lakes

Closed surface depressions represent potential sites for surface lake formation (e.g. Leeson et al., 2012, 2015). Thus, to estimate the maximum potential distribution of surface lakes, I consider every closed surface depression as a potential surface lake. Closed depressions were surveyed by filling the sinks of the GIMP-DEM, posted at 30 m resolution (Howat et al., 2014; 2017). The closed surface depression dataset was filtered to remove false depressions caused by noise in the DEM, and depressions that are unlikely to host surface lakes. Small (≤ 0.125 km^2) (Yang et al., 2015), very shallow (mean depth ≤ 1.5 m), very deep (mean depth ≥ 50 m) depressions, and depressions located on thin (≤ 10 m) and ungrounded ice according to BedMachine v.2 data (Morlighem et al., 2014) were removed.

To test the reliability of the surface depression inventory as a surface lake proxy, it was compared with contemporary ice sheet wide surface lake surveys derived from Moderate Resolution Imaging Spectroradiometer (MODIS) satellite imagery. These were provided by Selmes et al. (2011) and Leeson et al. (2013) for the period 2003–2009. The spatial coincidence between depressions and surface lakes was assessed and expressed as recall (percentage of surface lakes with matching depressions) and precision (percentage of depressions hosting surface lakes) values (Livingstone et al., 2013) for each main catchment of the GrIS – delineated by the Goddard Ice Altimetry Group (Zwally et al., 2012) – above and below the current equilibrium-line altitude (ELA). The average of the monthly modelled SMB datasets for the period of 2000-2009, obtained from MAR v.3.5.2 forced by ERA-Interim (Fettweis et al., 2013, 2017), was used to derive the current ELA.

I also surveyed closed surface depressions from the ArcticDEM (Release 5, DigitalGlobe Inc., 2017) – which is widely regarded as one of the best large-scale high-resolution surface DEM for the Arctic areas – in order to test the reliability of the GIMP-DEM derived dataset. I intend to use the GIMP-DEM – instead of the ArcticDEM – for my main analyses as ArcticDEM data are not available for some small regions of the GrIS (i.e. there are “holes” in the DEM). As a first step the Arctic DEM

granules were downsampled from 5 m (the original grid resolution) to 25 m using bilinear interpolation, in order to restrict the computational requirements of my data operations. Then, the downsampled DEM granules were merged and the closed surface depressions were delineated, as described above. The subsequent comparisons with the surface lake surveys were carried out in the same manner as previously described.

3.2.2.2. Potential surface rivers

In order to estimate the potential maximum spatial coverage of rivers on the GrIS, I used standard hydrologic analysis tools in ArcGIS 10.1. First, a flow accumulation raster was derived from the GIMP-DEM, after filling the sinks not included in the GIMP-DEM derived surface depression dataset (Section 3.2.2.1). Next, the river vectors were extracted from the flow accumulation raster using a minimum catchment area. The resultant river network is highly sensitive to the choice of this minimum catchment area, thus the extraction of rivers was carried out using a variety of catchment areas (0.1, 0.2, 0.3, 0.4, 0.5 and 1 km^2). These GIMP-DEM derived river networks were then compared with the Landsat-8 derived river dataset, surveyed by Yang and Smith (2016) in SW Greenland, to find the optimal minimum catchment area (Section 3.3.2.2).

3.2.2.3. Potential moulins

As moulins are point-like (i.e. have small spatial dimensions), they are hard to detect on moderate resolution surface DEMs such as the GIMP-DEM. Hence, they were mapped manually (S. Livingstone, personal communication, 2017) using a high resolution Surface Extraction with TIN-based Search-space Minimization (SETSM) DEM (Noh and Howat, 2015; 2 m grid resolution) which is available for a 14,576 km^2 area in SW Greenland – retrieved mostly in 2011 – largely overlapping with the Landsat-8 domain. In contrast to the previous two approaches (Section 3.2.2.1 and 3.2.2.2) and also the study of Yang and Smith (2016), this survey directly yields the sites of large (> 2m diameter) active (i.e. transporting meltwater from the surface to the bed) or inactive moulins. As soon as a moulin becomes inactive (i.e. loses its meltwater supply) it starts to close due to inward freezing – if it remains water-filled – and/or creep closure (Catania and Neumann, 2010). This could limit my ability to capture the true maximum distribution of moulins. However, Catania and Neumann (2010) have shown that the very top (i.e. close to the ice surface) of moulins could remain partially

open even if the moulin is inactive. Therefore, I propose that the SETSM-DEM derived moulin dataset does estimate the maximum distribution of large moulins accurately.

However, high resolution DEMs are not available for the whole GrIS, moulins are restricted to areas where the surface melt is currently high, and it is labour intensive to survey moulins manually. In order to overcome these limitations and estimate the ice sheet-wide maximum potential distribution of moulins, an ice sheet-wide principal strain rate map was derived from the mean of MEaSUREs ice flow velocity datasets (Version 2) for the winters of 2007-2009 (Joughin et al., 2010; 2017) following the approach of Poinar et al. (2015) (A. Sole, personal communication, 2017). The formation of moulins due to hydrofracture requires an initial crack (e.g. a crevasse) at the ice sheet surface, which is propagated to the ice sheet bed by tensile stresses due to meltwater infilling (Das et al., 2008; Krawczynski et al., 2009). The spatial distribution of crevasses has been shown to correspond well with areas of principal strain rates above +0.005 yr^{-1} (Joughin et al., 2013; Poinar et al., 2015). My principal strain rate map thus allows a first order investigation of the connection between surface relief and potential sites for hydrofracture – and thus moulin formation – at the ice sheet scale.

3.2.3 Comparing the observed mean surface relief with the surface hydrological features of SW Greenland

To compare the observed mean surface relief with surface lakes, rivers and moulins – derived either from satellite imagery or surface DEMs – in SW Greenland, first the observed surface relief was binned using exponentially increasing bin limits (with 2 as the base and the exponents increasing by 0.5). Then, the relative spatial coverage of surface lakes, the density of rivers and the density of moulins – all of them derived from Landsat-8 imagery by Yang and Smith (2016) – were calculated for every observed surface relief category. The same approach was repeated on spatial subsets – corresponding to the domain of the Landsat-8 survey of Yang and Smith (2016) – of the GIMP-DEM derived closed surface depression and surface river datasets. In the latter case, river densities were obtained using different minimum catchment areas and compared with the Landsat-8 derived river densities in order to find the optimal minimum catchment area. As the SETSM-DEM largely overlaps with the Landsat-8 domain, the approach was repeated on the complete SETSM-DEM derived moulin dataset.

In order to control for runoff, first the MAR derived runoff (Fettweis et al., 2013, 2017) was binned into three categories (100-300 mm/month, 200-400 mm/month, 300-500 mm/month; water-equivalent) – approximately centred at the mean (297 mm/month) with ranges slightly higher than 1 standard deviation (167 mm/month) – then the analysis described above was repeated for each runoff category. The three surface DEM derived datasets were excluded from these analyses (i.e. controlling for the runoff) as they estimate the maximum potential distribution of surface hydrological features, and thus are time-integrated. After filtering out surface relief categories with small areas (< 160 km^2), which occurred close to the minimal and/or maximum surface relief in some cases, statistical tests were carried out on the resultant datasets.

3.2.4 Comparing the observed and predicted mean surface relief with the surface hydrological features of the whole GrIS

The ice sheet-wide comparisons were carried out somewhat differently than the comparisons in SW Greenland. The observed and predicted mean surface relief datasets were binned using exponentially increasing bin limits with 2 as the base – which agrees with the procedure described in Section 3.2.3 – the exponents were increased by 1 instead of 0.5. Furthermore, only categories smaller than 4500 km^2 were removed (as opposed to 160 km^2 in SW Greenland). Finally, the retrieved metrics of the surface hydrological features also differ to some extent. Besides the relative spatial coverage of surface depressions and the density of surface rivers, the mean area of surface depressions and the mean link length of surface rivers were also calculated for each relief category. Metrics from the principal strain rate map – i.e. the mean absolute strain rate and the relative coverage of the area where the strain rates exceed +0.005 yr^{-1} – were retrieved for every observed/predicted mean surface relief category. As the ice sheet-wide comparisons included regions where surface melt is currently negligible (as opposed to the Landsat-8 domain in SW Greenland which lies completely in the ablation zone), they were not controlled for runoff.

3.3 Results

Here, I test the hypothesis that bed-to-surface variability transfer controls the spatial pattern of surface drainage at the ice sheet scale. This is crucial as it enables me to use the predicted mean surface relief – obtained by employing the theory of bed-to-surface variability transfer – as a proxy for estimating palaeo/future surface drainage

structures. Comparing the predicted mean surface relief and the surface drainage is the most direct way of doing this. However, mismatches between the observed and predicted mean surface relief – due to known limitations of the theory and the input data – will bias these relationships. Hence, I also compare the surface drainage with the *observed* mean surface relief, which has been shown to be controlled by the bed-to-surface variability transfer in Chapter 2. This approach allows me to circumvent the aforementioned bias and provides flexibility for palaeo/future predictions where data uncertainties (e.g. knowledge of bed topography and other properties) will vary.

3.3.1 Comparison of closed surface depressions and surface lakes

First, I quantify how well the sites of surface lakes can be inferred from the GIMP-DEM derived closed surface depression dataset, as several subsequent analyses will utilize this dataset. The majority (81%) of observed surface lakes are located below the current ELA which agrees well with previous observations (e.g. Echelmeyer et al., 1991; Howat et al., 2013). Furthermore, it justifies my approach to restrict the comparisons to surface lakes and depressions below the current ELA.

A recall (percentage of surface lakes which fall within a depression) of 78% indicates that GIMP-DEM derived surface depressions can be used to predict the sites of contemporary surface lakes below the ELA accurately (Table 3.1). There are several reasons why the basin of a surface lake could be missed on surface DEMs. Some lakes might be present at the time of DEM retrieval, and some surface lakes may also survive the melt season and freeze at the beginning of the subsequent winter (Selmes et al., 2013, Koenig et al., 2015). Detecting the corresponding basins of such lakes is complicated as they are completely or partially filled with water/ice. Furthermore, some surface lakes might be very shallow, with a maximum depth of 1-2 m (Banwell et al., 2014). The basins – i.e. hosting surface depressions – of shallow lakes might also be shallow, which could make them difficult to detect on surface DEMs, especially considering that the mean vertical 1σ error of the GIMP-DEM is 1.56 m across the GrIS (Howat et al., 2017). However, even shallow surface lakes could cause sharp reflectivity gradients on optical satellite images, as there is a large difference in the albedo of ice and water (Sneed and Hamilton, 2007). In fact, removing false positives due to the presence of saturated firn (e.g. slush swamps) is a major challenge of satellite derived surface lake surveys (e.g. Johansson et al., 2013).

Table 3.1 Comparison of GIMP-DEM and ArcticDEM derived closed surface depressions and satellite derived contemporary surface lakes. [1]Only GIMP-DEM and ArcticDEM derived depressions and observed surface lakes below the current ELA, derived from ERA-Interim forced MAR over 2000–2009, were considered. [2]The percentage of the volume/area of GIMP-DEM and ArcticDEM derived depressions hosting surface lakes from the total depression volume/area of each catchment, only considering depressions below the ELA.

Catchment	N	NE	E	SE	S	SW	W	NW	Total
Total number of surface lakes	215	413	168	18	37	1347	363	415	**2976**
Surface lakes below the ELA (%)	95	84	61	78	78	80	79	84	**81**
GIMP-DEM									
Total number of depressions	1404	1917	3661	1513	439	2688	1468	2353	**15443**
Recall below the ELA[1] (%)	69	76	91	57	72	74	84	90	**78**
Precision below the ELA[1] (%)	19	43	16	6	15	40	34	27	**31**
Precision of volume below the ELA[1,2] (%)	49	84	49	15	31	76	74	56	**68**
Precision of area below the ELA[1,2] (%)	45	75	44	10	31	73	69	54	**63**
ArcticDEM									
Total number of depressions	1414	1874	3309	1539	441	2637	1428	2320	**14962**
Recall below the ELA[1] (%)	71	76	83	57	69	75	81	88	**78**
Precision below the ELA[1] (%)	19	46	17	6	14	42	34	28	**32**
Precision of volume below the ELA[1,2] (%)	42	83	50	16	32	76	73	56	**67**
Precision of area below the ELA[1,2] (%)	45	76	44	12	31	73	69	54	**64**

A precision (percentage of depressions hosting surface lakes) of 31% indicates that even below the ELA a lot of GIMP-DEM derived depressions currently do not host surface lakes (Table 3.1). Low precision is expected because a range of factors could hinder the formation of surface lakes in depressions, e.g. the presence of crevasses, moulins and narrow surface channels draining the lakes – none of which are visible on the GIMP-DEM due to its moderate spatial resolution (Howat et al., 2014, 2017) and/or the transient thermal incision of surface streams (Karlstrom and Yang, 2016) – and/or inadequate meltwater supply. Surveys using satellite imagery could have also missed surface lakes due to limited availability and/or moderate spatial resolution of the MODIS imagery, and the short lifetime of some surface lakes (Selmes et al., 2011; Leeson et al., 2013; Cooley and Christoffersen, 2017). However, depressions below the

ELA where surface lakes were not detected are significantly smaller than depressions where surface lakes were present. Although only 31% of the surface depressions below the ELA have corresponding surface lakes, these depressions account for 68% and 63% of the total volume and area of the depressions below the ELA, respectively (Table 3.1).

The performance of the GIMP-DEM was very similar to the ArcticDEM (Table 3.1), thus giving me confidence in the reliability of the GIMP-DEM derived depression dataset. The catchment-specific recall and precision values also demonstrate that the GIMP-DEM derived surface depression dataset performs relatively well in all catchments of the GrIS, though the accuracy is not homogenous (Table 3.1). It is worth noting that the precision – and also the precision weighted by the area/volume of the depressions – is rather low in SE Greenland, meaning that only a small portion of the detected closed surface depressions below the ELA hosts lakes. I attribute this to the large thickness of the firn layer, which facilitates the formation of a vast firn aquifer system and restricts the evolution of surface lakes and rivers in SE Greenland (Howat et al., 2013; Poinar et al., 2017). Based on the ice sheet-wide recall (78%) and precision (63-68% when depressions are weighted by their area and volume, respectively), I propose that the GIMP-DEM derived surface depressions could be used to infer the distribution, especially the volume and area, of surface lakes below the ELA with acceptable – below 40% – uncertainty (Table 3.1).

3.3.2 The observed mean surface relief and surface drainage of SW Greenland

3.3.2.1 Landsat-8 derived surface lakes and GIMP-DEM derived surface depressions

The spatial density of Landsat-8 derived surface lakes and GIMP-DEM derived closed surface depressions in SW Greenland is highest in areas displaying moderate observed surface relief; around 25 m (Fig. 3.1D). This result is found also for the subsets of the Landsat-8 lakes corresponding to different runoff intervals (Fig. 3.1D) though the 100-300 mm interval lacks relief exceeding 32 m (Fig. 3.1C). GIMP-DEM derived depressions have a higher overall spatial coverage than Landsat-8 derived lakes, though the trends are very similar (Fig. 3.1D). The runoff interval subsets indicate that the overall lake coverage decreases with higher runoff (Fig. 3.1D).

In the context of the null hypothesis – that these features are randomly distributed in relation to the surface relief – the maximum standard score (maximum standardised deviation from the mean) of the spatial coverage of lakes is statistically significant for the full Landsat-8 domain (Table 3.2). Depressions and subsets of lakes for different runoff categories yielded similar, albeit statistically less significant, results (Table 3.2). These results indicate a strong control on surface lake and depression structure by the surface relief, somewhat biased by runoff.

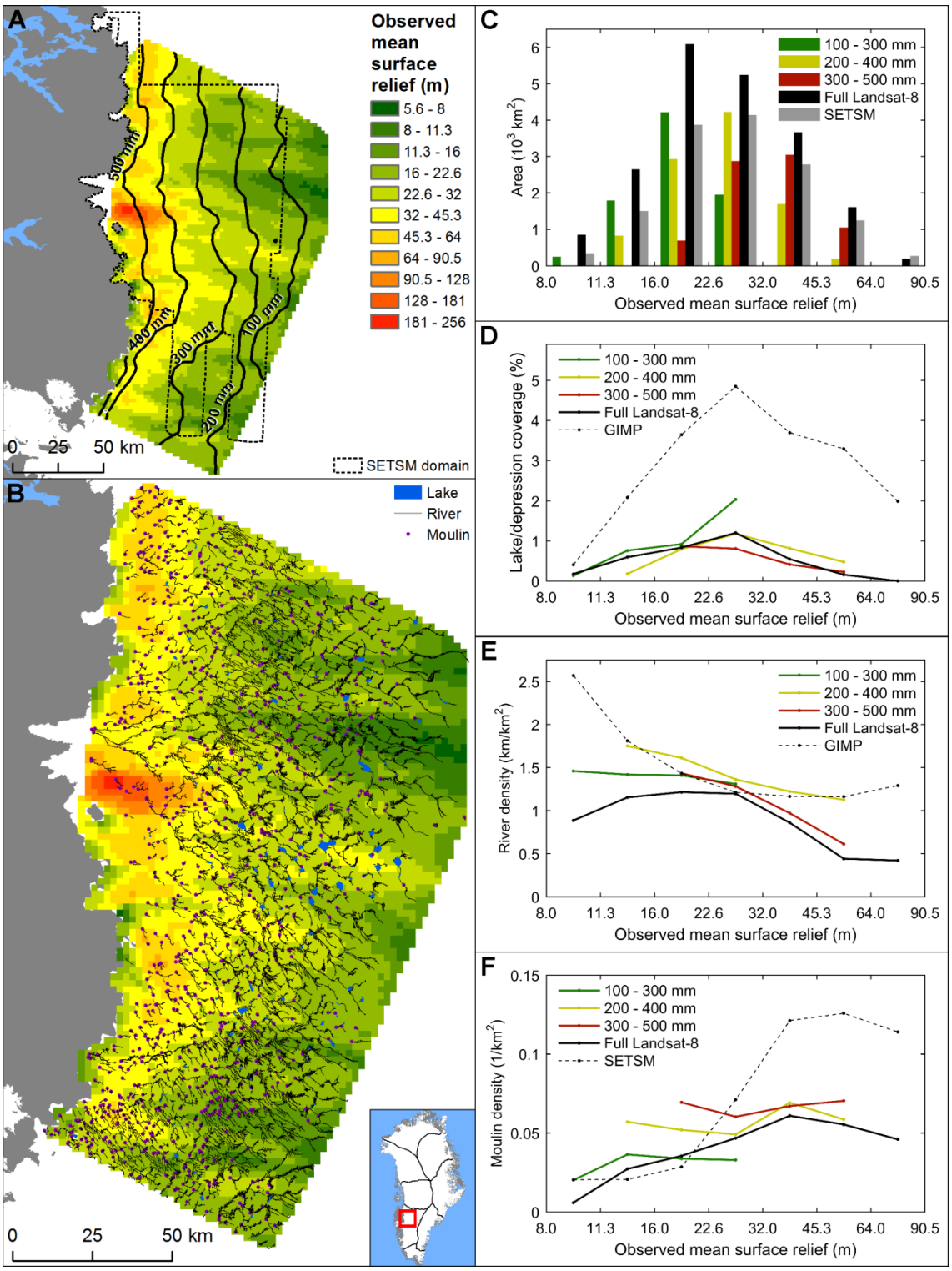

Figure 3.1 (A) Observed mean surface relief map for the full Landsat-8 survey domain combined with the outlines of the SETSM domain (dashed boundary) and contours representing different levels of the modelled Aug, 2013 runoff. (B) Observed mean surface relief compared with the distribution of Landsat-8 derived surface lakes, rivers and moulins in SW Greenland. (C) Area histograms of the observed mean surface relief categories of the full Landsat-8 domain, SETSM domain, and different runoff intervals of the Landsat-8 domain; categories smaller than 160 km^2 and in the case of the SETSM domain above the relief of 90.5 m are excluded. (D) Landsat-8 derived lake coverage and GIMP-DEM derived depression coverage, (E) Landsat-8 and GIMP-DEM derived river density, (F) Landsat-8 and SETSM-DEM derived moulin density corresponding to observed mean surface relief categories. (D, E, F) To control for runoff, subsets of Landsat-8 derived lakes, rivers and moulins were created for the runoff intervals of 100-300 mm, 200-400 mm and 300-500 mm.

Table 3.2 Coefficients of determination (R^2) and *p*-values of the quadratic models fitted on different inferential characteristics (e.g. density, coverage) of the Landsat-8, GIMP-DEM and SETSM-DEM derived surface drainage features, principal strain rates and observed mean surface relief. Models were fitted on ice sheet wide datasets, subsets for the Landsat-8 domain and subsets for different runoff intervals within the Landsat-8 domain. *P*-values of the maximum and minimum standard scores, describing the probability of getting such values assuming a normal distribution, are also provided.

Landsat-8 domain	Quadratic trend (R^2)	Quadratic trend (p)	Maximum standard score (p)	Minimum standard score (p)
Landsat-8 lake coverage	0.49	0.26	0.05	0.12
GIMP depression coverage	0.67	0.11	0.09	0.05
Landsat-8 river density	0.72	0.08	0.16	0.09
GIMP river density	0.80	0.04	0.02	0.24
Landsat-8 moulin density	0.93	0.00	0.13	0.04
SETSM moulin density	0.94	0.00	0.13	0.15
Runoff interval (mm)	**Runoff controlled Landsat-8 lake coverage**			
100 - 300	0.96	0.21	0.09	0.15
200 - 400	0.76	0.24	0.10	0.09
300 - 500	0.95	0.23	0.18	0.13
	Runoff controlled Landsat-8 river density			
100 - 300	0.96	0.21	0.18	0.08
200 - 400	0.99	0.01	0.10	0.14
300 - 500	1.00	0.05	0.16	0.10
	Runoff controlled Landsat-8 moulin density			
100 - 300	0.73	0.52	0.22	0.07
200 - 400	0.20	0.80	0.06	0.15
300 - 500	0.50	0.70	0.21	0.08
Full GrIS				
GIMP depression coverage	0.62	0.09	0.06	0.15
GIMP mean depression area	0.15	0.66	0.08	0.15
GIMP river density	0.91	0.00	0.13	0.12
GIMP mean river length	0.80	0.02	0.10	0.16
Mean absolute strain rate	0.99	0.00	0.02	0.27
Coverage of high strain rate	0.99	0.00	0.02	0.25

3.3.2.2 Landsat-8 and GIMP-DEM derived surface rivers

Before discussing the comparison of the observed mean surface relief and surface rivers, I introduce my results concerning the choice of the optimal minimum catchment area as these have direct consequences on the GIMP-DEM derived river dataset, used for the subsequent comparisons. Since the GIMP-DEM derived rivers should approximate the maximum potential density of the Landsat-8 derived rivers, I propose that a minimal catchment area of 0.3 km^2 provides the best estimation (Fig. 3.2). Thus 0.3 km^2 will be used as the minimum catchment area in my subsequent

analyses. However, there are systematic differences between the river densities derived from Landsat-8 and the GIMP-DEM at low and high surface relief (discussed in Section 3.4). I also note that the river density trends associated with the different GIMP-DEM derived river datasets – employing different minimal catchment areas – are quite similar (Fig. 3.2). Therefore, I expect that my final outputs are not influenced significantly by the choice of a minimal river catchment area.

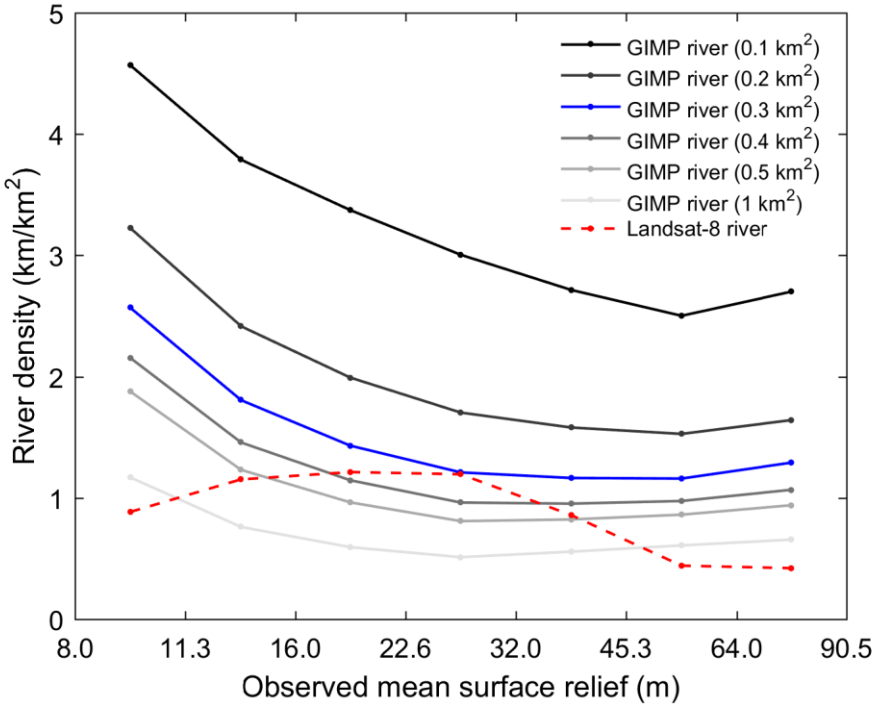

Figure 3.2 River densities corresponding to observed mean surface relief categories. Rivers have been obtained from the Landsat-8 survey (dashed red line) and from the GIMP-DEM using different minimal catchment areas (indicated on the legend).

Similarly to surface lakes and depressions, the Landsat-8 derived rivers of the full Landsat-8 domain have their highest spatial density in areas with moderate surface relief (Fig. 3.1E), though the corresponding maximum standard score has a relatively low statistical significance (Table 3.2). This relationship is less clear when considering GIMP-DEM derived rivers, and Landsat-8 derived river subsets for different runoff intervals (Fig. 3.1E). These suggest that the density of surface rivers generally decreases with increasing surface relief (Fig. 3.1E). The decreasing trends could be described by statistically significant quadratic equations, except for the low runoff subset (Table 3.2). In general the Landsat-8 derived river densities are lower than the GIMP-DEM derived river densities, especially at low and high surface relief (Fig. 3.1E). This situation is also apparent in the case of the Landsat-8 derived river subsets corresponding to low

and high runoff (Fig. 3.1E). However, Landsat-8 derived river densities corresponding to moderate runoff are very similar to the GIMP-DEM derived river densities (Fig. 3.1E). The limited coherence between the different trends suggests additional controlling factors besides surface relief.

3.3.2.3 Landsat-8 and SETSM-DEM derived moulins

Moulin density extracted from Landsat-8 and the SETSM-DEM increases with surface relief (Fig. 3.1F). The SETSM-DEM reveals a higher overall moulin density, which is not surprising given its time-integrated nature and higher spatial resolution (Fig. 3.1F). Both trends can be described by statistically significant quadratic equations (Table 3.2). However, Landsat-8 derived moulin densities of different runoff intervals exhibit statistically insignificant increasing trends with surface relief (Fig. 3.1F, Table 3.2), which suggests that surface relief is not the main control on moulin density. Nevertheless, these trends are offset from each other, implying that moulin density increases with runoff (Fig. 3.1F).

3.3.3 The observed mean surface relief and surface drainage of the whole GrIS

The ice sheet wide distribution of the GIMP-DEM derived surface depressions has the highest relative spatial coverage around moderately high surface relief (Fig. 3.3E), while depressions are the largest around moderately low surface relief (Fig. 3.3F). Maximum standard scores of the depression coverage and the mean depression area have statistical significance levels just above the conventional 0.05 boundary (Table 3.2). The ice sheet wide density and mean link length of the GIMP-DEM derived surface rivers decrease with increasing surface relief, following statistically significant quadratic equations (Fig. 3.3G-H, Table 3.2). The absolute principal strain rates and the coverage of principal strain rates above +0.005 yr^{-1} – the latter of which could be considered as proxy for crevasses (Poinar et al., 2015) and moulins (provided there is enough melt) – increase monotonically with the observed surface relief (Fig. 3.3I-J), following quadratic equations (Table 3.2). These results, approximating the relationship between the observed surface relief and the maximum potential ice sheet wide surface drainage, resemble the relationships observed in SW Greenland (Section 3.3.2).

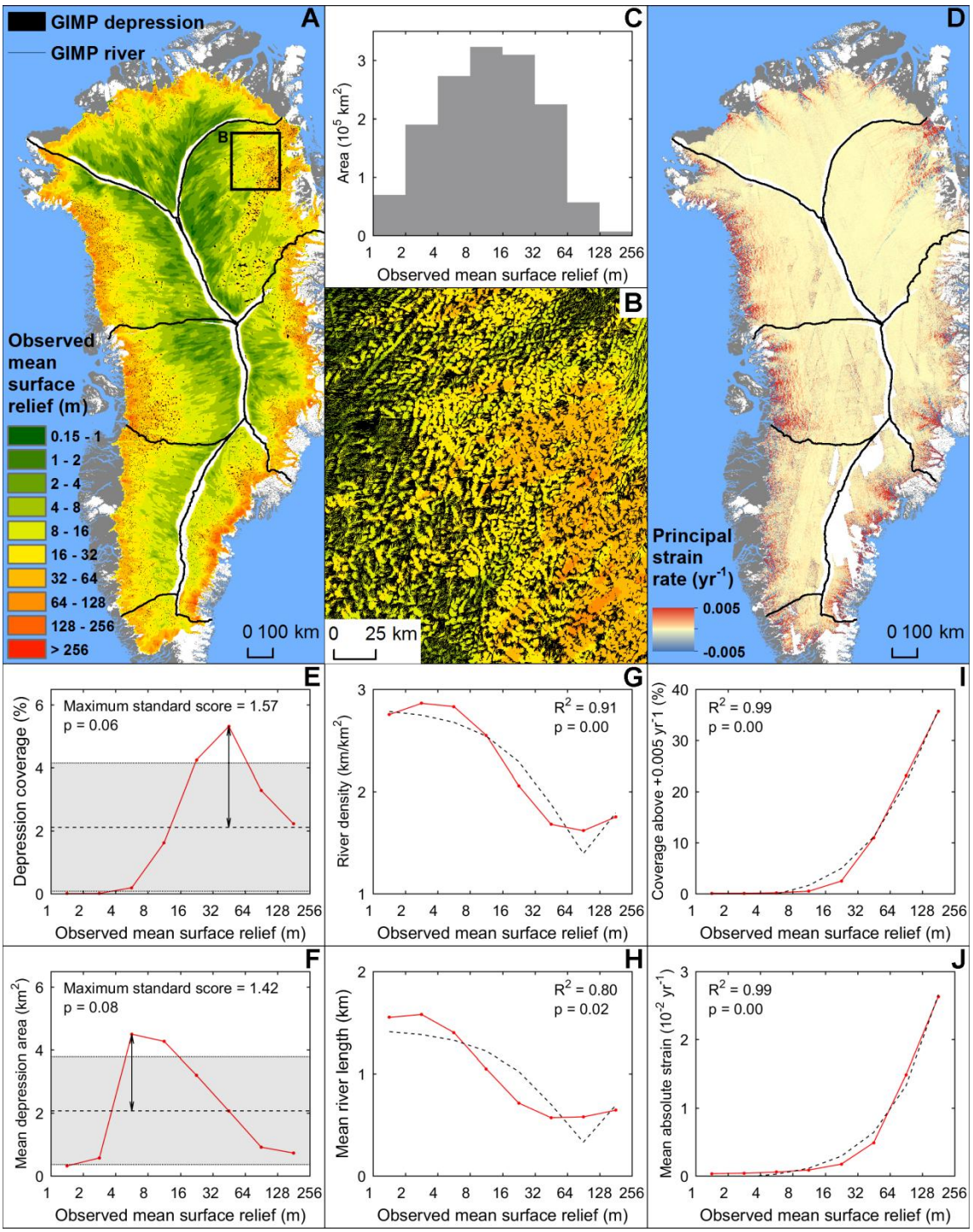

Figure 3.3 (A) Observed mean surface relief map compared with the distribution of GIMP-DEM derived closed surface depressions of the whole ice sheet (B) and GIMP-DEM derived rivers of NE Greenland. (C) Area covered by the observed mean surface relief categories of the GrIS is also shown; categories smaller than 4500 km^2 have been removed. (D) The ice sheet wide principal strain rate is also shown. (E) The coverage (F) and mean area of the GIMP-DEM derived depressions corresponding to observed mean surface relief categories has been calculated from the ice sheet wide depression dataset. (G) The density (H) and mean link length of the GIMP-DEM derived rivers, (I) the mean absolute principal strain rate (J) and the coverage of the area where principal strain rates exceed +0.005 yr^{-1} are also provided in the same manner for the whole ice sheet. Maximum standard scores, with their corresponding p-values, and the best-fit quadratic trends (dashed line), with their corresponding R^2 and p-values, are shown where applicable.

3.3.4 The predicted mean surface relief and surface drainage of the whole GrIS

Relationships between the predicted mean surface relief and the different aspects of surface drainage features (Fig. 3.4) are similar to the ones described in Section 3.3.3, though the precise trends are somewhat different. In the case of mean absolute strain rates and the coverage of principal strain rates above +0.005 yr^{-1}, there are no major differences between the trends calculated using the observed and the predicted mean surface relief (Figs. 3.3I-J and 3.4I-J).

River density and mean river link length show decreasing trends with greater surface relief, both for the observed and the predicted relief dataset (Figs. 3.3G-H and 3.4G-H). However, in the case of the predicted relief dataset, high river density and high mean river link length do not persist at low surface relief – as they do below ~8 m in the case of the observed relief dataset – due to the underestimation of the mean surface relief in the interior of the ice sheet (Chapter 2).

Large depressions (i.e. high mean depression area) correspond to the lowest predicted surface relief categories, whereas the same categories of the observed surface relief have small depressions (Figs. 3.3F and 3.4F). However, the mean area of the depressions generally decreases with surface relief in both cases, though only above ~6 m in the case of the observed relief dataset (Figs. 3.3F and 3.4F). Relative depression coverage is the highest at moderate predicted surface relief, which is similar to the observed relief dataset, though the maximum is offset by ~30 m (Figs. 3.3E and 3.4E). I propose that these differences are caused by the general underestimation of the mean surface relief, especially in the interior of the ice sheet.

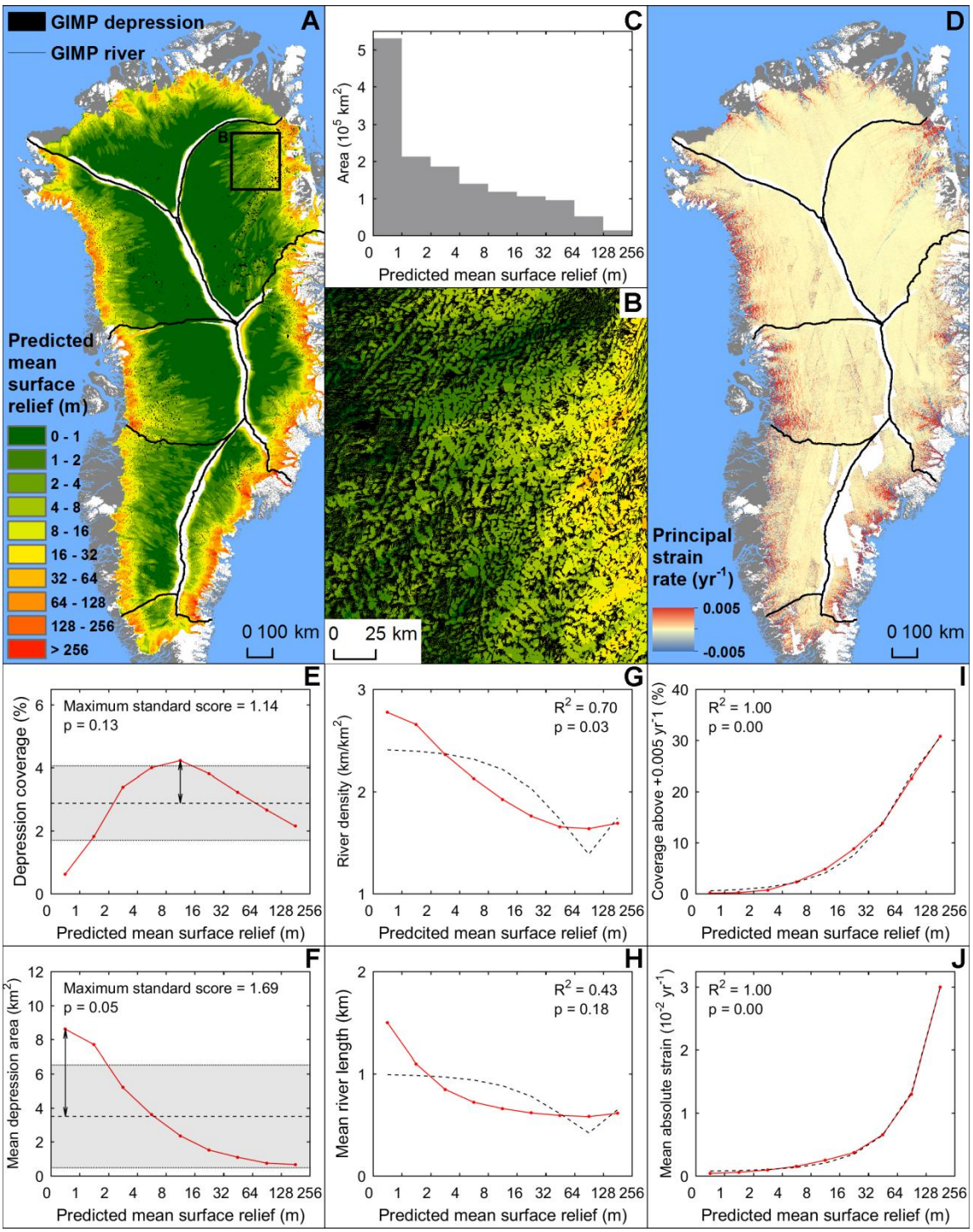

Figure 3.4 (A) Predicted mean surface relief map compared with the distribution of GIMP-DEM derived closed surface depressions of the whole ice sheet (B) and GIMP-DEM derived rivers of NE Greenland. (C) Area covered by the predicted mean surface relief categories of the GrIS is also shown; categories smaller than 4500 km^2 have been removed. (D) The ice sheet wide principal strain rate is shown as well. (E) The coverage (F) and mean area of the GIMP-DEM derived depressions corresponding to predicted mean surface relief categories has been calculated from the ice sheet wide depression dataset. (G) The density (H) and mean link length of the GIMP-DEM derived rivers, (I) the mean absolute principal strain rate (J) and the coverage of the area where principal strain rates exceed +0.005 yr^{-1} are also provided in the same manner for the whole ice sheet. Maximum standard scores, with their corresponding p-values, and the best-fit quadratic trends (dashed line), with their corresponding R^2 and *p*-values, are shown where applicable.

3.4 Discussion

Based on my results, I suggest that surface depressions form preferentially in areas with moderate surface relief (Figs. 3.1 and 3.3). Here, surface undulations are large enough to form deep closed surface depressions – which act as potential sites for surface lakes (Section 3.3.1) – but not too large to restrict the formation of closed depressions due to the high regional surface slope associated with large amplitude surface undulations. Despite the very similar trend to GIMP-DEM derived depressions, Landsat-8 derived lakes have a lower overall spatial coverage in SW Greenland (Fig. 3.1D). This is expected because the topographic depressions delineate the maximum potential lake coverage, whereas the Landsat-8 snapshot records actual lakes in existence on 19 Aug 2013. The relationship between the distribution of surface lakes and surface relief is only mildly biased by surface runoff, as the relative spatial coverage trends of the surface lake subsets for different runoff intervals are very similar in SW Greenland (Fig. 3.1D). However, there is a slight overall reduction of the relative lake coverage with increasing runoff (Fig. 3.1D), which is expected due to the higher potential for the rapid drainage of lakes where more meltwater is available (Krawczynski et al., 2009; Selmes et al., 2011; Stevens et al., 2015). In conclusion, I propose that – similarly to surface depressions – surface lakes also form preferentially in areas with moderate surface relief.

According to my findings, especially those derived from the GIMP-DEM (Figs. 3.1E and 3.3G-H), the surface river network becomes progressively more fragmented as surface relief increases towards the ice sheet margin, as a result of the more efficient transfer of basal perturbations (Gudmundsson, 2003) (Chapter 2). However, other factors also influence the structure of the observed (i.e. Landsat-8 derived) river network. Firstly, at high elevations where both the runoff and the surface relief are generally low, the river density is smaller than expected as not all potential river channels fill with meltwater due to the low runoff. Furthermore, at low elevations where both the runoff and the surface relief are generally high, the formation of crevasses and moulins – partly due to more frequent hydrofracture caused by the higher meltwater supply – fragments the river network further. These processes are indicated by the divergence of the Landsat-8 and GIMP-DEM derived river densities at low and high surface relief (Fig. 3.1E), as the GIMP-DEM derived river survey cannot fully capture such effects. The aforementioned suggestions are also supported by the fact that the Landsat-8 derived river densities corresponding to the low and high runoff subset (i.e.

100-300 mm, 300-500 mm) are generally lower than the GIMP-DEM derived river densities (Fig. 3.1E).

My results also demonstrate a general increase in moulin density with surface relief. This is due to enhanced crevassing in these regions (Poinar et al., 2015), which is supported by the ice sheet wide comparison of surface relief and principal strain rates (Fig. 3.3I-J). However, this relationship seems to be the most biased by runoff (Fig. 3.1F), due to enhanced potential for hydrofracture and subsequent moulin formation when more meltwater is available (Krawczynski et al., 2009; Poinar et al., 2017). Perhaps this is due to the positive feedback between surface-to-bed meltwater injection events, tensile stress perturbations, and hydrofracturing (Christoffersen et al., 2018; Hoffman et al., 2018).

In general, comparisons using the predicted and observed mean surface relief yielded similar results, though the trends were offset due to the overall underestimation of the observed mean surface relief by the predictions. Hence, I suggest that comparisons using the predicted mean surface relief are relevant to palaeo/future applications where the bed topography is not known accurately and the transfer theory is used to obtain the mean surface relief, which are both likely to cause the prediction to underestimate the actual surface relief.

3.5 Summary

My analyses show that basal topography preconditions the large-scale structure of the surface drainage system on the GrIS, while other factors such as surface runoff generation and crevassing influence the temporal evolution of drainage within a particular melt season (i.e. when, where and to what degree surface drainage develops compared to the maximum potential). Although I suggest that surface relief affects the distribution of all elements of the surface drainage system on the GrIS, the highest degree of control was demonstrated in the case of surface lakes (and surface depressions). Surface depressions and lakes have the largest coverage in areas with moderate surface relief, while the spatial density of surface rivers decrease and the density of moulins increase with increasing surface relief. In conclusion, I suggest that the greatest potential for surface meltwater injections into the subglacial drainage system occurs where the bed-to-surface topography transfer and thus the surface relief are moderately high, due to the aligned presence of a high density surface drainage system and moulins/crevasses.

CHAPTER 4: FUTURE DISTRIBUTION OF SURFACE LAKES ON THE GREENLAND ICE SHEET

4.1. Introduction

Analyses in Chapter 3 demonstrate that bed-to-surface transfer influences the large-scale spatial structure of the surface drainage, though this is modulated by runoff. In particular, the spatial distribution of surface lakes is strongly controlled by the transfer of basal variability, which agrees well with previous observations of lakes re-occurring annually at the same locations (e.g. Echelmeyer et al., 1991) and also with the intuitive idea that surface lakes require closed topographical basins to form (Section 1.2.2). In accordance with previous investigations (e.g. Leeson et al., 2015) that have modelled the surface drainage of the GrIS (Section 1.2.4), I here restrict my future surface drainage projections to surface lakes. This is justified because lakes are crucial to the hydrological system of the GrIS due to their role in facilitating the formation of surface-to-bed meltwater connections, especially at high elevations (e.g. Clason et al., 2015). Thus predicting the future distribution of surface lakes is of key importance regarding the dynamic response of the GrIS to changing surface melt rates (Section 1.1).

Although several studies have modelled the contemporary seasonal evolution of surface lakes, only Leeson et al. (2015) projected their future distribution – until 2060 – by extrapolating ice sheet-wide trends from a small region in SW Greenland (Section 1.2.4). Here, I expand upon the findings of Leeson et al. (2015) by incorporating ice sheet-wide differences in surface depression availability and future SMB into my projections about the changing distribution of surface lakes during the 21st century. In order to accurately capture the effects of surface depression distribution on future surface lakes, I initially assume a stationary ice sheet surface topography during the 21st century which allows me to use accurate contemporary ice sheet-wide surface depression surveys (O4). As the rapid drainage of lakes is a key process in the formation of high elevation surface-to-bed meltwater connections (e.g. Clason et al., 2015), I also estimate the potential for rapid lake drainage by considering elastic fracture mechanics (e.g. Krawczynski et al., 2009) and surface crack presence (Poinar et al., 2015) (O4).

However, in reality, surface relief is expected to change on the GrIS due to the evolving ice thickness, basal slip ratio and surface slope, caused by the warming climate

(e.g. Vizcaino et al., 2014) (Section 1.2.4). In Chapter 3 it was demonstrated that surface relief strongly influences the spatial distribution of surface depressions. Hence, the validity of surface lake projections assuming stationary ice surface topography is temporally restricted (Section 1.2.4). In order to quantify this limitation, first I estimate future changes in surface relief between 1980-2300 from ice sheet model outputs and contemporary bed topography, using techniques introduced in Chapter 2. Then, I evaluate the impact of such changes on the distribution of surface lakes during the 21st century, which quantifies the uncertainty caused by the assumption of stationary ice sheet surface topography for the 21st century (O4). I also provide an extended projection – up until 2300 – of the changing distribution of surface lakes, which incorporates the effects of the changing surface topography of the GrIS (Section 1.2.4, O5).

4.2. Methods

4.2.1 Predicting surface lake distribution and volume with fixed ice surface topography

First, I describe my approach for projecting the changing distribution and volume of surface lakes during the 21st century. The ice sheet-wide closed surface depression survey derived from the contemporary GIMP-DEM (Section 3.2.2.1) – which has been shown to correlate well with the distribution of surface lakes below the ELA (Section 3.3.1) – and modelled future SMB datasets (Fettweis et al., 2013, 2017) form the basis of these projections. This assumes that the surface topography/relief of the GrIS – and the distribution of surface depressions – will not change significantly during the 21st century. Although the GrIS currently experiences considerable thinning rates – 0.12 m yr^{-1} and 0.84 m yr^{-1} in slow and fast flowing regions respectively (Pritchard et al., 2009) – these will not lead to substantial relative thinning over 100 years in regions with large ice thickness, e.g. in the case of >1 km thick ice, typical for 73.6% of the ice sheet (Morlighem et al., 2017a, b), the aforementioned thinning rates will lead to <1.2-8.4% relative thinning over 100 years. I propose that relative ice thinning below 10% will not modify the surface relief significantly, thus larger surface relief changes will be restricted to regions close to the ice sheet margin where the contemporary ice thickness is low. This idea will be tested further in Section 4.3.2. Despite this uncertainty, using a contemporary surface depression inventory – hence

assuming stationary ice surface topography – allows a more direct and precise estimation of the total volume of future surface lakes as the volume of contemporary surface depressions is known accurately from surface DEMs. Using a fixed ice sheet surface topography is also consistent with several other studies investigating future surface processes – including the distribution of surface lakes – on the GrIS (e.g. Fettweis, et al., 2013; Leeson et al., 2015; Ignéczi et al., 2016).

4.2.1.1 Estimating the volume of contemporary surface lakes

Although the spatial coincidence of closed surface depressions and surface lakes has been evaluated (Section 3.2.2.1 and 3.3.1), it still remains a challenge to estimate the potential volume of lakes that typically form in surface depressions. Most depressions are not filled to the lip with water (e.g., McMillan et al., 2007; Leeson et al., 2012) due to the rapid or slow drainage of lakes over the ice sheet surface (via lip incision) or to the bed (via hydrofracture) and/or the inadequate surface meltwater supply (Selmes et al., 2011, 2013). A lake can drain and refill multiple times during the melt season (e.g. Fitzpatrick et al., 2014), meaning that the volume of a particular surface lake changes temporally. To account for these effects, I compared the volume of depressions with the maximum volume of coinciding observed surface lakes. This approach allows me to estimate the maximum amount of meltwater a depression typically contains, when hosting a surface lake.

A radiative transfer model (Eq. 4.1) (Sneed and Hamilton, 2007) was used to calculate water depths for the pixels of MODIS band 1 (620–670 nm) images from 2003, 2005, 2006, and 2007 in N, NE, and SW Greenland (Ignéczi et al., 2016), using a similar method to that employed by Langley et al. (2016). MODIS Level-1B Calibrated Radiances (MOD02) data were processed using the technique of Gumley et al. (2007).

$$z = \frac{\ln(A_d - R_\infty) - \ln(R_w - R_\infty)}{g} \qquad \text{(Eq. 4.1)}$$

In the radiative transfer model (Eq. 4.1) z is the water depth, R_w is the reflectance of the pixel of interest, and R_∞ is the reflectance of optically deep water, estimated from the open sea visible on each image. The quantity g is best estimated as 2 K_d (Maritorena et al., 1994), where K_d is the diffuse attenuation coefficient for down-welling light and found to be 0.30945 and 0.43045 for the wavelengths of 620 and 670 nm, respectively (Smith and Baker, 1981). A_d is the lake substrate albedo estimated for each image based on the pixels directly adjacent to lakes delineated using a MODIS band 3 to band 1 ratio

of 1.2 (Box and Ski, 2007; Banwell et al., 2014). Best estimates for water depths were calculated using mean R_∞ and A_d where K_d was the average of K_d^{620} and K_d^{670}. Using the water depth data, which were extracted from 24 to 40 MODIS images per melt season, the maximum volume of each surface lake in each melt season was recorded. Then the mean of these 4 maximum volumes was calculated for each surface lake – estimating the maximum meltwater a lake typically contains – and compared with the volume of the host depression.

4.2.1.2 Assessing the potential for rapid lake drainage

Besides estimating the volume of meltwater contained in closed surface depressions, I also assessed the theoretical potential (Krawczynski et al., 2009) for surface depressions to host lakes that can drain rapidly to the ice sheet bed due to hydrofracture. Hydrofracture and consequently rapid lake drainage, requires a crack on the ice sheet surface – with an initial depth above 1-7 m – and sufficient meltwater to keep this crack completely filled as it propagates to the ice sheet bed (Das et al., 2008; Krawczynski et al., 2009; Poinar et al., 2015, 2017). The propagation of water-filled cracks to the ice sheet bed is driven by the tensile stress at the tip of the crack caused by meltwater infilling, due to the density contrast of water and ice (Krawczynski et al., 2009).

First, I assessed whether surface cracks could form at the sites of surface depressions, as the presence of an initial surface crack is a precondition for rapid lake drainage. As mentioned in Section 3.2.2.3, crevasses have been observed to occur preferentially in areas where the principal strain rates are over +0.005 yr^{-1} (Joughin et al., 2013; Poinar et al., 2015). Hence, the probability of surface crack formation at a certain location was estimated by calculating the relative spatial coverage of areas with principal strain rates (derived in Section 3.2.2.3) above +0.005. As both extensive and compressive principal strain rates show a distinctive decreasing trend with elevation (Poinar et al., 2015), principal strain rates were binned according to the surface elevation of the ice sheet. Then, the relative spatial coverage of principal strain rates above +0.005 yr^{-1} was calculated for every elevation bin. This binning was carried out separately in every major catchment of the GrIS (Zwally et al., 2012) in order to retain regional variations. The probability of a surface crack in a certain surface depression was estimated from the catchment-specific trend of high principal strain rate coverage with elevation. This is likely a conservative estimation, as the transient effects of tensile

shocks – which are triggered by initial rapid lake drainage events and form surface cracks over large distances (Christoffersen et al., 2018; Hoffman et al., 2018) – have not been considered.

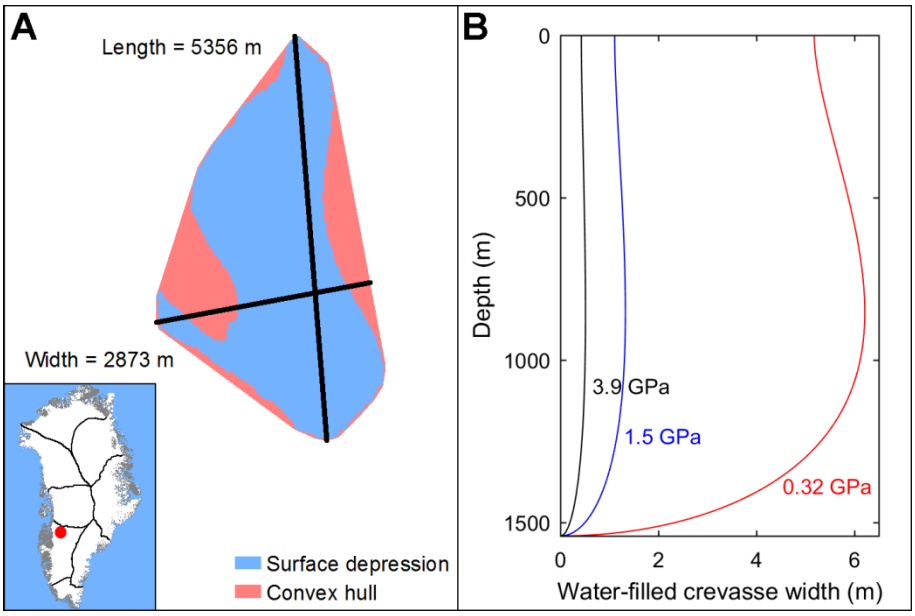

Figure 4.1 (A) The length and width of a convex hull of a depression in W Greenland; the average of the length and width of the convex hull was prescribed as the length of the potential water-filled crack forming at the depression. (B) The width profile of a potential water-filled crevasse at the depression – calculated using three different shear moduli – the depth of the potential crevasse is set to the mean ice thickness at the depression.

To calculate the volume of meltwater required to keep surface cracks forming in surface depressions filled with water until they reach the ice sheet bed, first I calculated the width profile (i.e. crack opening width) of potential water-filled cracks (Fig. 4.1B) according to the approach of Krawczynski et al. (2009), which is based on elastic fracture mechanics (Weertman, 1971, 1973, 1996). The depth of the potential water-filled cracks was prescribed as the ice thickness at the sites of surface depressions (Fig. 4.1B) as the depth of cracks completely filled with meltwater is unbounded (Krawczynski et al., 2009). Besides the depth of a crack, the elastic shear modulus of the ice also controls the width profile of a water-filled crack; the lower the shear modulus (i.e. less rigid ice) the wider the crack (Krawczynski et al., 2009). The shear modulus of thick ice sheets varies due to the properties of ice (e.g. strain rate, temperature, grain size, impurities). As these conditions are not well quantified for the GrIS, the width profile of potential water-filled cracks was calculated using a realistic range of shear moduli: 0.32, 1.5 and 3.9 GPa (Vaughan, 1995; Krawczynski et al., 2009) (Fig. 4.1B). As the elastic fracture mechanics model assumes planar cracks (Krawczynski et al., 2009), the average of the width and length of the convex hull of

each depression – created by the Minimum Bounding Geometry tool in ArcGIS 10.1 – was prescribed as the length of the water-filled crack potentially forming at each depression (Fig. 4.1A).

Volumes of potential water-filled cracks at each depression were calculated by integrating the width profiles – calculated using the three different shear moduli at each depression – and multiplying them by the length of the cracks. Then, the three different potential volumes of water-filled cracks were compared with the total volume of the corresponding surface depression, in order to determine whether it could host enough meltwater to hydrofracture to the ice sheet bed. Although most surface depressions are not filled completely with meltwater (Section 4.2.1.1), the total volume of each surface depression was used for these comparisons as the typical meltwater infilling percentage of surface depressions – quantified in Section 4.2.1.1 – is strongly influenced by rapid lake drainage (Section 4.2.1.1). Hence, this approach allows the estimation of the full potential for rapid drainage. Only considering elastic fracture mechanics, hydrofracture at a particular surface depression was considered to be likely (probability = 1), possible (probability = 0.5) and unlikely (probability = 0), if the volume of the depression was larger than all three, at least one, or none of the corresponding water-filled crack volumes calculated using the three different shear moduli. Finally, the probability of rapid lake drainage at every depression was estimated by multiplying the probability of surface crack presence and the probability of hydrofracture.

4.2.1.3 Surface mass balance and surface lake projections

The majority of surface lakes on the GrIS form below the ELA (Section 3.3.1) and their inland expansion correlates well with the rising ELA (Howat et al., 2013). Thus, in order to obtain robust estimates of the maximum distribution of surface lakes on the GrIS, only surface depressions located below modelled ELAs – obtained from MAR v.3.5.2 outputs (Fettweis et al., 2013, 2017) – were assumed to host surface lakes when projecting into the future or reconstructing the past. The total amount of meltwater contained in the depressions – that were assumed to host lakes – was calculated from the total volume of the depressions and the typical present-day meltwater infilling proportion (Section 4.2.1.1). Based on my comparisons between surface depressions and observed surface lakes, the overall uncertainty of these volumes is around 40% (Section 3.3.1). Furthermore, the potential for hydrofracture and rapid

lake drainage was assessed (as described in Section 4.2.1.2) for the depressions below the respective modelled ELA.

Monthly modelled SMB from MAR v.3.5.2 outputs (Fettweis et al., 2013, 2017) was used to obtain the ELAs between 1980 and 2099. MAR v.3.5.2 was forced by ERA-Interim from 1980 to 2009, and by the outputs of three general circulation models (GCMs): Canadian Earth System Model (CanESM2), Norwegian Climate Center's Earth System Model (NorESM1), and Model for Interdisciplinary Research on Climate (MIROC5) from 1980 to 2099. Mid- and high-range future greenhouse gas scenarios – representative concentration pathway (RCP) 4.5 and 8.5 respectively – were used to force the three GCMs from 2006 to 2099 (Fettweis et al., 2013, 2017). Mean SMB data sets, with a temporal resolution of 5 years for the historical period of 1980–2009 and 10 years for the projected period of 2010–2099, were calculated from the model outputs. To avoid using average ELAs for large areas, SMB was investigated at each depression to determine whether it fell above or below the ELA. When reporting summary statistics, the mean of all surface lake volume projections from 1980 to 2009 is considered as the current reference. The future state – from 2070 to 2099 – is calculated separately for the two representative concentration pathways.

4.2.2 Predicting surface lake distribution and volume with evolving ice surface topography

The distribution of surface depressions and lakes is controlled by surface relief (Chapter 2), which in turn is controlled by the bed topography, ice thickness, basal sliding and surface slope (Chapter 3). Hence, temporally-evolving ice sheet geometry (i.e. ice thickness, surface slope) and dynamics (i.e. basal sliding) could cause significant changes in the surface relief and in the distribution of surface depressions and lakes, especially over longer time-scales. My approach to predict the long-term future evolution – until 2300 – of surface relief on the GrIS is largely based on Chapter 2. However, in this chapter, I also use the predicted surface relief datasets – derived from contemporary bed topography and ice sheet model projections – as proxies for surface depressions and lakes, based on the outcomes of Chapter 3. I also check the accuracy of my surface lake projections for the 21st century assuming fixed ice sheet surface topography (section 4.2.1) by quantifying the effect of changing surface relief on surface lake distribution.

4.2.2.1 Predicting changes in the surface relief

In order to estimate the future evolution of surface relief on the GrIS, I obtained ice thickness, surface elevation, SMB, basal and surface ice-flow velocity data (with 10 km horizontal resolution) from the ice sheet model outputs of Vizcaino et al. (2014). This particular GrIS simulation was chosen as the thermo-mechanical ice sheet model (SICOPOLIS 3.0) is bi-directionally coupled to an atmosphere-ocean general circulation model (AOGCM) – European Centre Hamburg 5.2/Max Planck Institute ocean model (ECHAM5.2/MPI-OM) – and unphysical corrections were not employed during the initialisation (Vizcaino et al., 2014). Furthermore, Vizcaino et al. (2014) provided extended projections up until 2300 using various greenhouse gas emission scenarios. These include standard RCPs and Extended Concentration Pathways (ECPs); the latter are used to force the AOGCM beyond 2100.

The modelled average ice thickness, surface elevation, SMB, and basal- and surface velocity were acquired for three time slices, 1980-1999 (with historical greenhouse gas concentrations), 2080-2099 (with both RCP 4.5 and 8.5 considered) and 2280-2299 (with only RCP-ECP 8.5 considered). Similar to the procedure outlined in Section 2.2.2 – using manually delineated seed-points – over 5000 flowlines were derived from the average modelled surface ice-flow velocity data of each time slice, yielding four separate flowline datasets (1980-1999, 2080-2099 RCP 4.5, 2080-2099 RCP 8.5 and 2280-2299 RCP 8.5). Then, the average modelled ice thickness, surface elevation, and basal- and surface velocity of each time-slice were sampled along the flowlines at a spacing of 250 m. The basal slip ratio along the flowlines was calculated according to Gudmundsson et al. (1998), using the formula u_b/u_d (u_b: basal velocity, u_d: deformational velocity) where u_b is readily available from the model outputs of Vizcaino et al. (2014) and u_d was estimated by subtracting the modelled basal velocity from the modelled surface velocity. The contemporary bed topography – acquired from the IceBridge BedMachine Greenland, Version 3 dataset (Morlighem et al., 2017a, 2017b) – was also sampled at a spacing of 250 m along the flowlines of all time-slices.

Background variables and perturbations were separated as described in Section 2.2.3. The SICOPOLIS 3.0 model is based on the SIA, and the model outputs have a horizontal resolution of 10 km (Vizcaino et al., 2014). Hence, the smoothing distance optimisation procedure, which is described in Section 2.2.5, could not be applied here. However, in Section 2.3.1, I demonstrated that a smoothing distance of 20 km yields the optimal match between the predicted and observed mean surface relief of the

contemporary GrIS, using observed datasets. This is in accordance with the theoretical expectation that the smoothing distance should be over 10 times the mean ice thickness (Ng et al., 2018), which is 1632 m along the flowlines derived for the contemporary GrIS from observed datasets. This thickness is comparable to mean ice thickness values of 1579, 1609, 1603 and 1571 m, calculated along the flowlines derived from the 1980-1999, 2080-2099 RCP 4.5, 2080-2099 RCP 8.5 and 2280-2299 RCP 8.5 ice sheet model outputs respectively. Thus, a smoothing distance of 20 km was used for all time-slices and greenhouse gas emission scenarios to ensure consistency in the results here and throughout the thesis.

Although basal topographic perturbations are known from the high resolution BedMachine v.3 data, mesoscale basal slipperiness perturbations cannot be derived from the model outputs of Vizcaino et al. (2014). This situation is similar to the observed contemporary GrIS (Section 2.2.3), though the reasons are different. In the model projections, basal slipperiness perturbations are unknown due to the usage of the SIA and the limited spatial resolution of the ice sheet model outputs. Therefore, I excluded basal slipperiness perturbations when calculating the predicted mean surface relief of the future GrIS from the basal topographic perturbation and background (i.e. smoothed ice thickness, ice surface slope and basal slip ratio) profiles (as described in Section 2.2.3 and 2.2.4). The effects of excluding basal slipperiness perturbations on the predicted mean surface relief is estimated to be moderate, below 25% (Section 2.3.3). Thus, I expect that this will not significantly limit the accuracy of the surface relief projections. Furthermore, given the same initial limitations, my predicted mean surface relief projections and contemporary predicted surface relief datasets are directly comparable.

4.2.2.2 Inferring the future distribution of surface lakes from surface relief projections, and estimating the potential for rapid lake drainage

As shown in Chapter 3, mean ice surface relief can be used as a proxy for surface depressions and thus surface lakes. Here I employed this principle to estimate the changing future distribution of GrIS surface lakes beyond 2100, up until 2300. First, I estimated the changing relative spatial coverage, average depth and average size of surface depressions from the predicted mean surface relief datasets – obtained from ice sheet model outputs (Section 4.2.2.1) – using ice sheet-wide empirical relationships between the contemporary mean surface relief and surface depressions (Chapter 3). As

shown in Chapter 2, the predicted and observed mean surface relief differ systematically due to inaccuracies of the BedMachine v.3 data (Morlighem et al., 2017a, 2017b) and the transfer theory. This affects the empirical relationships between the mean surface relief and the surface depressions/drainage (Section 3.4.1). As I also used the BedMachine v.3 data and the transfer theory to predict the changing mean surface relief in the future (Section 4.2.2.1), the aforementioned bias applies here too. To account for this, I used the empirical relationships between the contemporary predicted mean surface relief and surface depressions (Fig. 4.2A-C, Section 3.3.4) for the calculations described below. Datasets describing the changing characteristics of surface depressions in the future were also used to estimate the changing potential for hydrofracture at surface depressions (similar to Section 4.2.1.2). Finally, using the datasets obtained here and modelled SMB from the outputs of Vizcaino et al. (2014) I estimated the changing maximum – i.e. during a given melt season – coverage and volume of surface lakes.

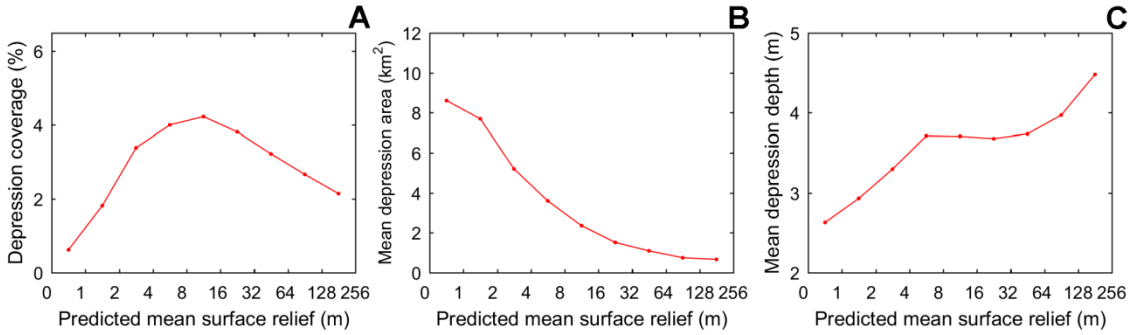

Figure 4.2 (A) The relative spatial coverage (B) mean area (C) and mean depth of the GIMP-DEM derived depressions corresponding to the predicted mean surface relief categories of the GrIS (Section 3.3.4).

Firstly, the predicted mean surface relief (Section 4.2.2.1) was converted to fractional depression coverage (i.e. the relative spatial coverage of depressions in a particular cell) (Fig. 4.3), mean depression depth (i.e. the typical mean depth of a single depression in a particular cell) and mean depression area (i.e. the typical volume of a single depression in a particular cell) using the relationships between the predicted mean surface relief and surface depressions, obtained for the contemporary GrIS (Fig. 4.2A-C). Net surface depression volume (i.e. the volume of depressions in a particular cell) was calculated from the fractional depression coverage and mean depression depth. Net surface lake volume was calculated below the modelled ELAs – from the outputs of Vizcaino et al. (2014) – by applying the typical present-day meltwater infilling ratio of depressions (Section 4.2.1.1) to the net depression volume. In order to estimate changes in surface lake distribution attributable to the changing SMB alone – thus partitioning

into dynamical (i.e. changing surface relief) and SMB induced changes – net surface lake volume was also derived while holding the surface relief constant at the 1980-1999 level.

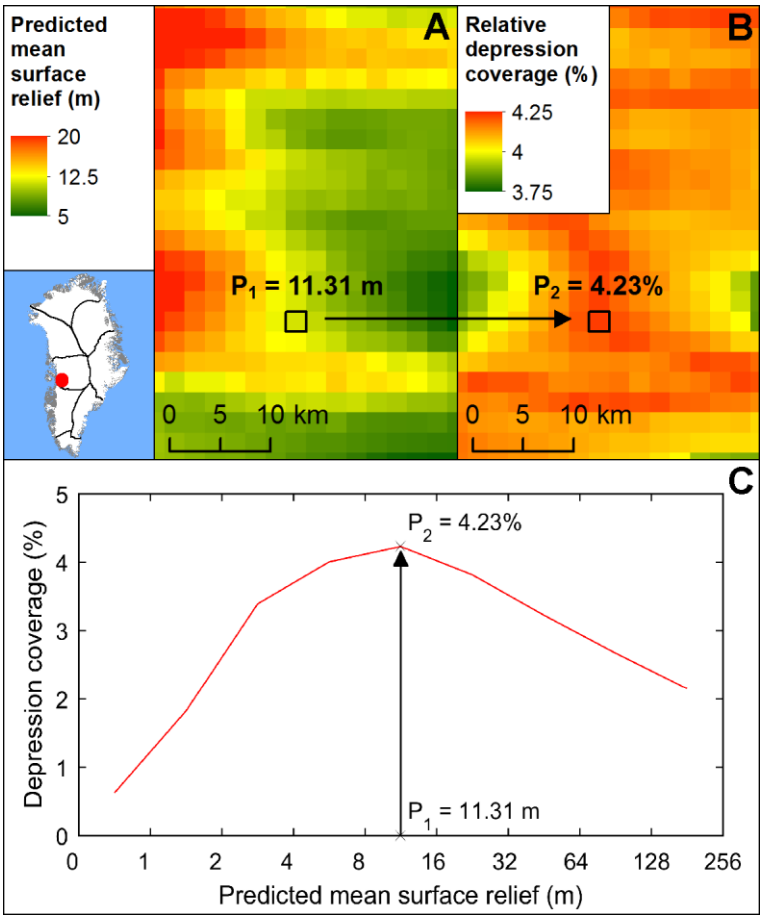

Figure 4.3 Illustration of the conversion of predicted mean surface relief – calculated using the SICOPOLIS 1980-1999 dataset – to fractional depression coverage. Panel (A) shows the predicted mean surface relief of a small area in W Greenland, while panel (B) shows the converted pixels – representing the fractional coverage of depressions – of the same area. Panel (C) shows the relationship – used for the conversion – between the predicted mean surface relief and the fractional depression coverage, derived for the contemporary GrIS in Chapter 3. The conversion of a single pixel is highlighted on all three panels.

The changing potential for hydrofracture was also assessed. First, mean depression volume (i.e. the typical volume of a single depression in a particular cell) was calculated from the mean depression depth and mean depression area. Then, mean depression diameter (i.e. the typical diameter of a single depression in a particular cell) was calculated from the mean depression area, assuming circular depressions. The volume of potential water-filled cracks (i.e. the typical volume of a single water-filled crack in a particular cell) was calculated from the mean depression diameter, the local ice thickness and the width profile of a potential water-filled crack at that particular location (Section 4.2.1.2). Finally, the mean depression volume was compared with the

water-filled crack volume. Hydrofracture of an average depression at a particular cell was considered to be likely, possible or unlikely as described in Section 4.2.1.2. The potential presence of surface cracks was estimated by calculating principal strain rates from the modelled surface velocity of each time-slice (Vizcaino et al., 2014) according to Section 3.2.2.3. Given the uncertainties in each of these methods – which are expected to be larger than in Section 4.2.1 due to the usage of ice sheet model outputs – I have not combined these measures to estimate the overall probability of rapid lake drainage, as per Section 4.2.1.2.

I also estimated the accuracy of the approach outlined above. In addition to the net surface depression volume calculated from the 1980-1999 SICOPOLIS outputs, net surface depression volume was also calculated from the predicted mean surface relief dataset derived for the contemporary GrIS (Chapter 2) using the same approach described above. Total depression volumes (i.e. sums of the net depression volume) were normalised by the area of the surface relief domain, as the surface relief datasets do not completely cover the GrIS. Finally, these volumes were compared with the total surface depression volume of the GrIS, which was directly derived from the GIMP-DEM (Section 3.2.2.1) and normalised by the area of the GrIS.

4.3 Results

4.3.1 Surface lake projections with fixed ice surface topography

4.3.1.1 Contemporary distribution of closed surface depressions on the GrIS

This section examines the contemporary ice sheet-wide distribution of GIMP-DEM derived surface depressions, as these represent the basis for projecting lake locations forward until 2100 assuming constant ice topography. I have identified 15,443 closed surface depressions on the GrIS using the GIMP-DEM (Table 4.1 and Section 3.3.1). Most depressions occur close to the ice sheet margin – 58.6% are within 25 km and 75.2% are within 50 km (Fig. 4.4). However, there are certain regions where large numbers of surface depressions occur in the far interior of the ice sheet, the most striking example of which is on the Northeast Greenland Ice Stream (Fig. 4.4). These depressions are typically also larger than the depressions closer to the ice sheet margins (Fig. 4.4).

The majority of surface depressions on the GrIS are capable of hosting enough meltwater to initiate hydrofracture to the bed of the ice sheet. Using the methods described in Section 4.2.1.2, hydrofracture is "likely" for 71.2% and "possible" for 28.4% of the closed surface depressions – after weighting the depressions with their volumes – on the GrIS (Table 4.1). Only 0.5% of the surface depressions are unlikely to host enough volume to initiate hydrofracture to the ice sheet bed (Table 4.1). In general, the potential for hydrofracture decreases towards higher elevations due to thicker ice (Fig. 4.4), although regional variations do occur (Table 4.1). Most notably, the percentage of depressions where hydrofracture is likely is significantly lower than average in the S and SE (Table 4.1), where most of the depressions are found at high elevations overlying thick ice (Fig. 4.4). The relative spatial coverage of strain rates above +0.005 yr^{-1} decreases with elevation, similar to the hydrofracture potential (Fig. 4.4). This trend also varies between catchments (Fig. 4.4). The relative spatial coverage of strain rates above +0.005 yr^{-1} is especially low in the N and NE and decreases rapidly with elevation. Conversely, the coverage is very high in the S and SE, and remains so even at high elevations (Table 4.1).

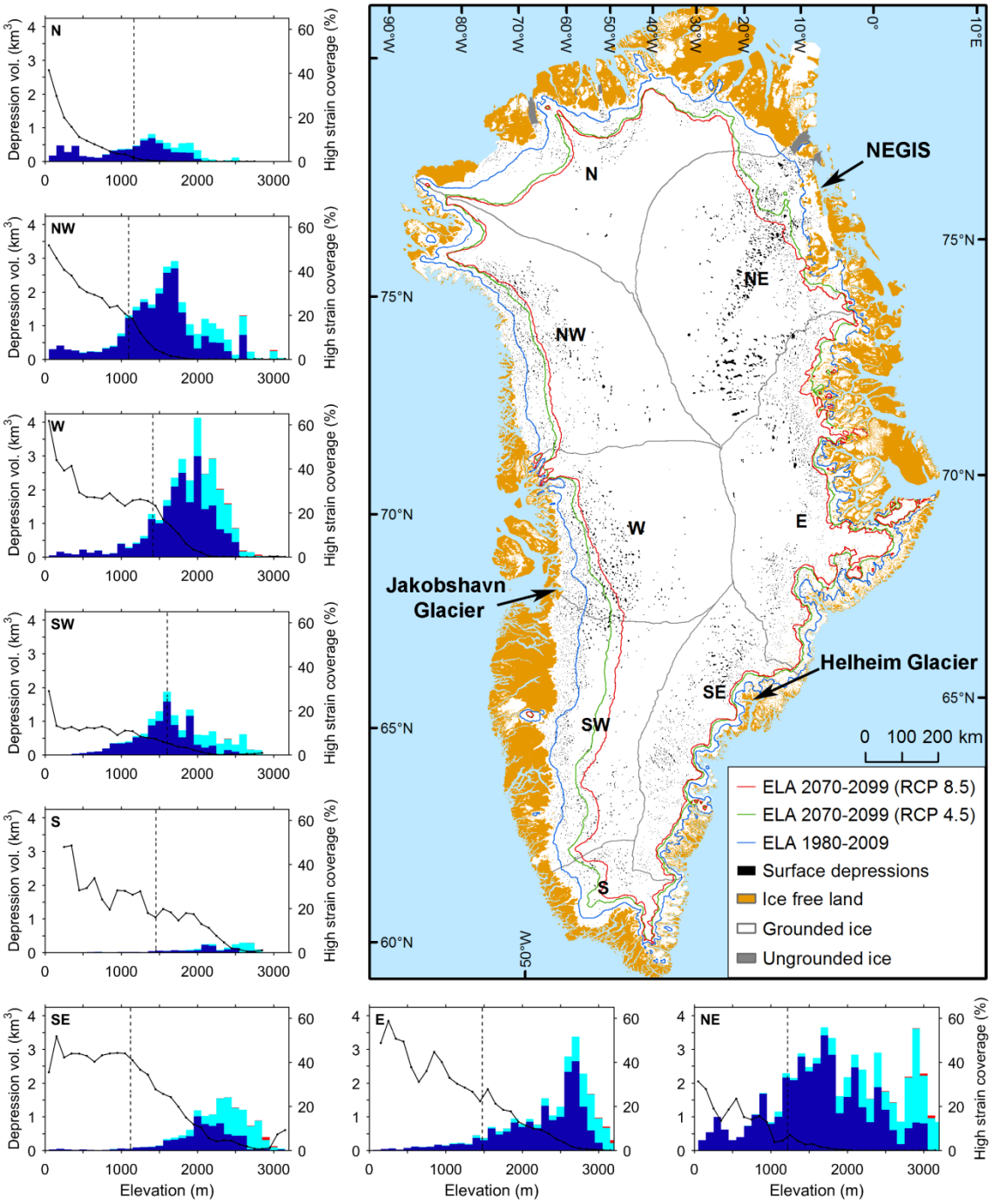

Figure 4.4 The map panel shows the distribution of surface depressions on the GrIS, and mean ELAs of 1980-2009, 2070-2099 (RCP 4.5) and 2070-2099 (RCP 8.5), derived from MAR outputs forced by ERA-Interim, CanESM2, NorESM1 and MIROC5 (Section 4.2.1.3). The bar plots show the volume of depressions derived from GIMP-DEM and sampled by their elevation with a bin size of 100m for each catchment. Depressions which are likely, possible or unlikely to initiate hydrofracture are represented by dark blue, light blue and red bars, respectively. The current ELA, derived from ERA-Interim forced MAR over 2000–2009, is indicated by dashed vertical lines on the bar plots. The relative spatial coverage of principal strain rates above +0.005 yr^{-1} is also indicated for every elevation bin (solid black lines).

Table 4.1 Characteristics of the contemporary GIMP-DEM derived closed surface depressions. [1]The ELA was derived from ERA-Interim forced MAR over 2000–2009. [2]Prior to calculating the percentages, the depressions were weighted with their volumes

Catchment	N	NE	E	SE	S	SW	W	NW	Total
Area of catchments (10^3 km^2)	252	311	261	153	58	193	225	268	**1721**
Total number of depressions	1404	1917	3661	1513	439	2688	1468	2353	**15443**
Relative spatial coverage of depressions (%)	0.8	3.2	1.9	2.1	1.2	2.0	2.1	1.8	**2.0**
Depression below the ELA (%)[1]	56	33	18	9	36	76	52	52	**41**
Relative spatial coverage of high strain rate (%)	1.1	1.2	4.2	10.6	10.0	3.2	3.6	3.8	**3.4**
Depressions with likely hydrofracture (%)[2]	78.2	71.9	72.3	50.9	57.5	68.1	70.7	80.0	**71.2**
Depressions with possible hydrofracture (%)[2]	21.8	27.7	27.0	47.9	42.2	31.8	28.7	19.8	**28.4**
Depressions with unlikely hydrofracture (%)[2]	0.0	0.3	0.7	1.2	0.2	0.1	0.7	0.2	**0.5**

4.3.1.2 Comparing the volume of contemporary surface depressions and lakes

To estimate the volume of surface lakes from the volume of depressions when projecting into the future, I first determine the volumes of spatially coincident contemporary GIMP-DEM-derived surface depressions and MODIS-derived surface lakes (Fig. 4.5). Around 5-10% of the depressions in each of the three study sites are almost completely full at some point during the melt season (Table 4.2). This is likely due to the presence of meltwater and/or frozen meltwater in the depressions at the time of the DEM survey, making the depressions appear shallower. However, depressions could also fill completely with meltwater if the corresponding lake drains slowly across the ice sheet surface – due to lip incision – instead of rapidly to the ice sheet bed. The distribution of maximum meltwater infilling proportions – the ratio between the volumes of spatially coinciding surface lakes and depressions – is relatively similar in the N and NE regions, with median values of 14% and 18% respectively (Fig. 4.5, Table 4.2). However, in the SW region the maximum meltwater infilling proportions are somewhat higher, with a median of 25% (Table 4.2). These differences are likely to be caused by the longer melt season and higher amount of available meltwater towards the south (Sundal et al., 2009; Fettweis et al., 2013, 2017).

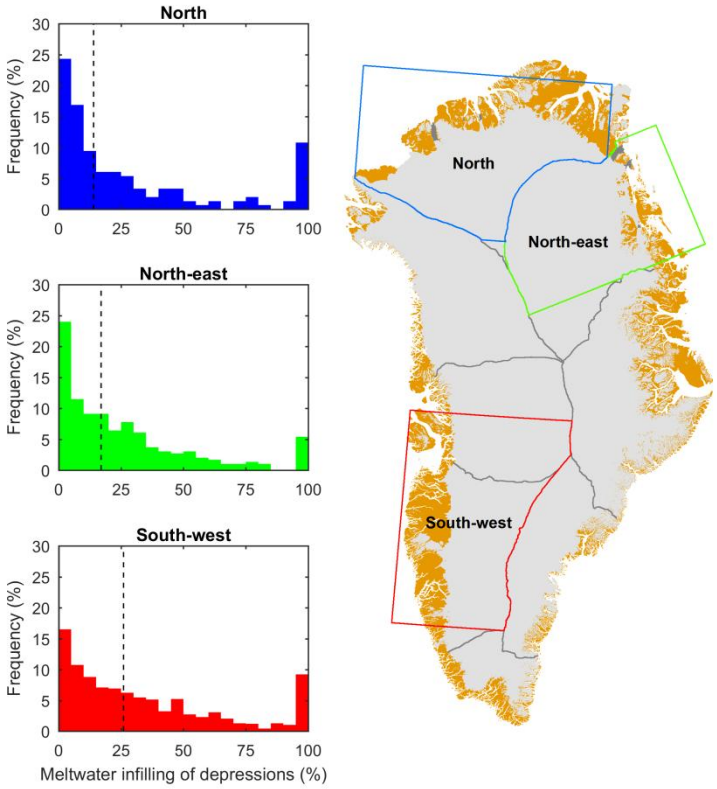

Figure 4.5 Relative frequency histograms showing the ratio of the volumes of spatially coinciding depressions and SGLs as percentages (meltwater infilling proportions), using a bin size of 5%. The three study areas, shown on the map inset, were plotted separately. Median values of the meltwater infilling proportions were also plotted for each study area (dashed black lines).

Based on these results, the maximum volume of meltwater that could typically be contained in depressions during a melt season was calculated by considering a 20% meltwater infill proportion of each depression. This is somewhat lower than the ice sheet-wide median (Table 4.2), and longer melt seasons with higher runoff are expected in the future (e.g. Fettweis et al., 2013), which is also likely to be enhanced by the increasingly efficient runoff from firn-covered regions (Machguth et al., 2016). Hence, my predictions should be considered conservative. Although my projections miss the intricacies of seasonal surface lake volume evolution, they place a conservative upper bound on the amount of meltwater that could get to the ice sheet bed via rapid lake drainage events.

Table 4.2 Summary statistics of the meltwater infilling proportions for the three study areas (delineated on Fig. 4.5) and for the whole dataset.

	NE	SW	N	Total
Depression number	296	1181	148	**1602**
Mean infilling proportion (%)	26.2	33.7	28.7	**32.3**
Median infilling proportion (%)	17.9	24.9	14.1	**23.1**
Full depressions (no.)	14	94	14	**122**
Full depressions (%)	4.7	8.0	9.5	**7.6**

4.3.1.3. The changing volume and rapid drainage probability of surface lakes during the 21st century with fixed surface topography

Total ice sheet and catchment-specific surface lake volume reconstructions and projections were obtained by summing the volume of every GIMP-DEM-derived depression below the relevant ELA and assuming that lakes fill 20% of every depression (Fig. 4.6). Estimations from 1980 to 2009 are in good agreement with earlier observations by Howat et al. (2013), who showed a strong increase in surface lake coverage after 2000, especially in the SW, W, and NW catchments. This agreement gives me confidence in the method's ability to capture ice sheet wide trends in future surface lake coverage. The majority of the projections show an increase in surface lake volume with time (Fig. 4.6) which is consistent with a warming climate causing a rising ELA throughout the GrIS (Fig. 4.4). Taking the mean of the projection outputs and assuming 40% overall uncertainty (Section 3.3.1), the maximum volume of meltwater that could be contained in surface lakes of the GrIS by the end of the 21st century (2070–2099) is estimated to be 10.8 ± 4.3 km^3 and 14.7 ± 5.9 km^3 under moderate (RCP 4.5) and high (RCP 8.5) climate change scenarios, respectively. This is a 172% (RCP 4.5) and 270% (RCP 8.5) increase relative to 1980–2009 (4 ± 1.6 km^3) respectively (Table 4.3).

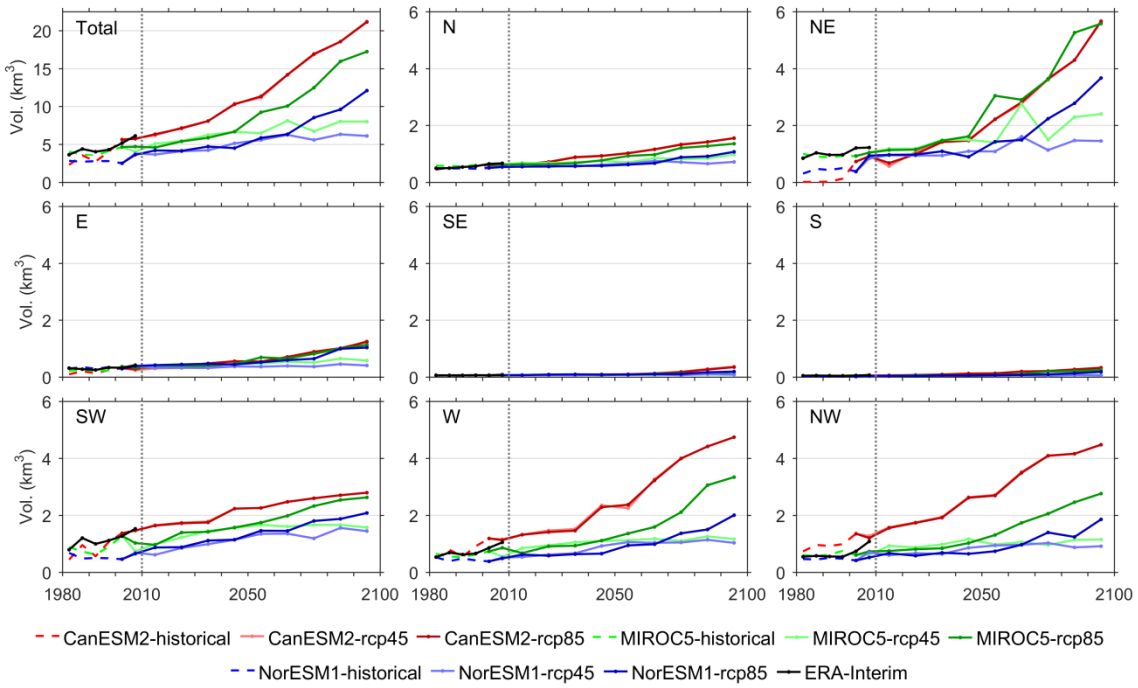

Figure 4.6 Ice sheet-wide and catchment specific surface lake volume reconstructions and projections for the period of 1980–2099 using various climate model outputs (described in Section 4.2.1.3). Surface lake volumes were calculated from the GIMP-DEM-derived surface depression dataset, assuming 20% meltwater infilling of the depressions below the respective ELAs. The dashed vertical lines on all panels represent the year 2010.

Although surface lake volumes increase across the whole GrIS, there are significant regional variations in the projected surface lake volume and the rate of increase (Fig. 4.6, Table 4.3). In the E, SE, and S catchments the current volume of surface lakes is very low (Table 4.3), which is in agreement with previous satellite derived observations (Selmes et al., 2011). Furthermore, surface lake volumes in these catchments are predicted to remain relatively low by the end of the 21st century – 0.14-0.67 km^3 (RCP 4.5) and 0.19-0.97 km^3 (RCP 8.5) – despite the large relative increase which ranges between 133-275% (RCP 4.5) and 208-469% (RCP 8.5) (Table 4.3). It is also important to note that these projected volumes are well below the full potential volume of surface lakes – which is calculated by assuming that all depressions host surface lakes, not just those below the ELA – in the E and SE catchments (Table 4.3). In the SW, W and NW catchments, where surface lakes are currently the most abundant (e.g. Selmes et al., 2011), the relative increase is smaller – 112-226% (RCP 4.5) and 163-334% (RCP 8.5) – though the projected surface lake volume is considerably higher – 1.91-2.21 km^3 (RCP 4.5) and 2.37-2.95 km^3 (RCP 8.5) – than in the E, SE and S catchments (Table 4.3). The projected surface lake volumes are also closer to their full potential in the W, NW, and especially in the SW (Table 4.3). The N and NE catchments behave differently to these two former groups. The relative increase in

surface lake volume is especially low in the N catchment – 80% (RCP 4.5) and 119% (RCP 8.5) – though the projected volume is only moderately low, 1 km^3 (RCP 4.5) and 1.68 km^3 (RCP 8.5). The NE is characterised by a very high relative surface lake volume increase – 265% (RCP 4.5) and 462% (RCP 8.5) – and also a very high projected lake volume, 2.65 km^3 (RCP 4.5) and 4.08 km^3 (RCP 8.5). Furthermore, the projected surface lake volumes of the NE catchment are well below the potential maximum, while in the N the projected volumes approach close to this limit by the end of the 21st century (Table 4.3).

Table 4.3 Reconstructed and projected surface lake volumes and the total potential volume of surface lakes – assuming that lakes fill 20% of every depression, where lakes are assumed to form – in every major catchment of the GrIS. The relative increase of surface lake volumes during the 21st century compared to 1980-2009. The volume of surface lakes within each catchment compared to the ice sheet-wide total surface lake volume.

	N	NE	E	SE	S	SW	W	NW	Total
Lake volume: 1980-2009 (km^3)	0.56	0.73	0.29	0.06	0.04	0.90	0.68	0.72	**4.0**
Lake volume: 2070-2099 RCP 4.5 (km^3)	1.00	2.65	0.67	0.15	0.14	1.91	2.21	2.09	**10.8**
Lake volume: 2070-2099 RCP 8.5 (km^3)	1.22	4.08	0.97	0.19	0.21	2.37	2.95	2.72	**14.7**
Total potential lake volume (km^3)	1.68	11.13	4.74	2.74	0.45	2.84	5.79	5.36	**34.7**
Relative change of lake volume: 2070-2099 RCP 4.5 (%)	80	265	133	142	275	112	226	189	**172**
Relative change of lake volume: 2070-2099 RCP 8.5 (%)	119	462	239	208	469	163	334	277	**270**
Relative lake volume: 1980-2009 (%)	14.0	18.3	7.2	1.5	0.9	22.7	17.1	18.2	
Relative lake volume: 2070-2099 RCP 4.5 (%)	9.3	24.5	6.2	1.4	1.3	17.6	20.4	19.3	
Relative lake volume: 2070-2099 RCP 8.5 (%)	8.3	27.7	6.6	1.3	1.4	16.1	20.0	18.5	

Due to the regional variations in surface lake expansion across the GrIS, the relative volume of surface lakes in the different catchments – compared to the ice sheet-wide total surface lake volume – will also change during the 21st century on the GrIS (Table 4.3). Most notably, the dominance of surface lake presence is predicted to shift from the SW towards the NE and to a lesser extent the W-NW during the 21st century (Table 4.3). Currently, the SW catchment has the highest proportion of surface lake volume on the GrIS (22.7%) – which is in agreement with satellite derived observations (Selmes et al., 2011) – while considerably smaller proportions of the ice sheet-wide surface lake volume are found in the NE (18.2%), W (17.1%) and NW (18.2%) (Table 4.3). However, by the end of the 21st century the SW is predicted to host 16.1-17.6% of the total volume of surface lakes on the GrIS, which is smaller than in the W (20-20.4%), NW (18.5-19.3) and NE (24.5-27.7%) (Table 4.3).

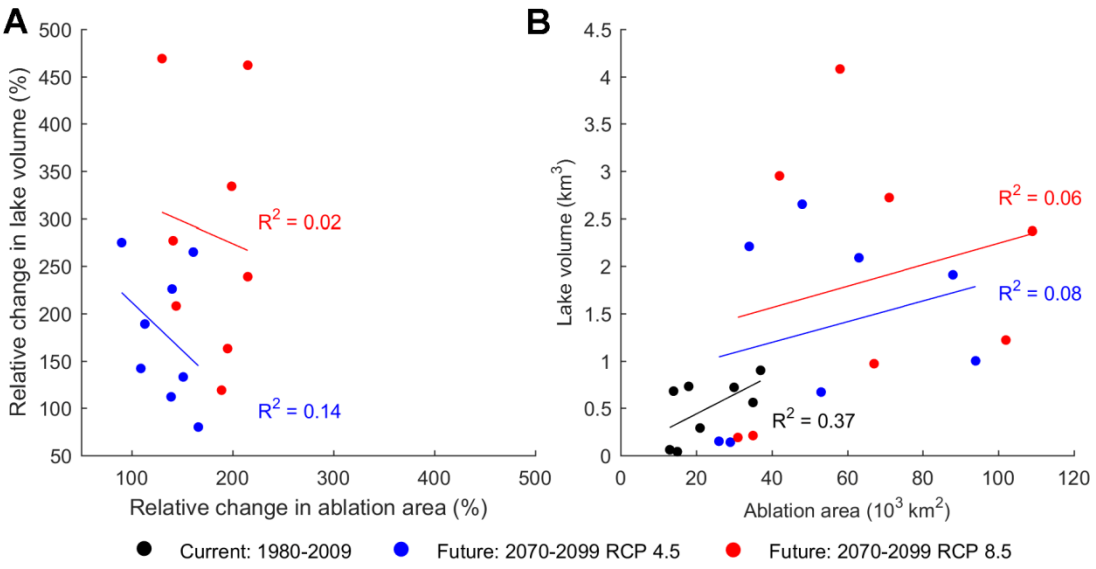

Figure 4.7 (A) The relative change in surface lake volume during the 21st century – i.e. 2070-2099 compared to 1980-2009 – for the different catchments of the GrIS, plotted against the relative change in ablation area. Two climate change scenarios were plotted separately: the RCP 4.5 (blue) and the RCP 8.5 (red). (B) The volume of surface lakes in the different catchments of the GrIS plotted against the size of the ablation area. Datasets from the different time-slices and climate change scenarios were plotted separately: 1980-2009 (black), 2070-2099 RCP 4.5 (blue) and 2070-2099 RCP 8.5 (red). Linear trends (solid lines) fitted on the different datasets, and the corresponding coefficients of determination (R^2) are also shown.

Table 4.4 The coverage of the ablation area in every major catchment of the GrIS. The relative increase in the coverage of the ablation area during the 21st century compared to 1980-2009. The coverage of the ablation area within each catchment compared to the ice sheet-wide total coverage of the ablation area.

	N	NE	E	SE	S	SW	W	NW	Total
Ablation area: 1980-2009 (10^3 km^2)	35	18	21	13	15	37	14	30	**184**
Ablation area: 2070-2099 RCP 4.5 (10^3 km^2)	94	48	53	26	29	88	34	63	**437**
Ablation area: 2070-2099 RCP 8.5 (10^3 km^2)	102	58	67	31	35	109	42	71	**516**
Relative change of the ablation area: 2070-2099 RCP 4.5 (%)	166	161	151	109	90	139	140	113	**138**
Relative change of the ablation area: 2070-2099 RCP 8.5 (%)	189	215	215	144	130	195	199	141	**181**
Relative coverage of the ablation area: 1980-2009 (%)	19.2	10.0	11.5	6.9	8.4	20.1	7.7	16.1	
Relative coverage of the ablation area: 2070-2099 RCP 4.5 (%)	21.5	11.1	12.2	6.0	6.7	20.2	7.8	14.5	
Relative coverage of the ablation area: 2070-2099 RCP 8.5 (%)	19.8	11.3	13.0	6.0	6.9	21.1	8.2	13.8	

Regional variations in the relative increase of surface lake volumes during the 21st century (Table 4.3) do not correlate well with the simultaneous relative expansion of the ablation area, especially in the case of the more severe RCP 8.5 climate change scenario (Fig. 4.7A, Table 4.4). I attribute this to regional variations in the distribution

of surface depressions (Section 4.3.1.1), as the relative expansion of the ablation area is roughly uniform across the GrIS (Fig. 4.7A, Table 4.4). This is well illustrated in the SE, S and NW catchments, where the lower than average relative expansion of the ablation area (Table 4.4) does not significantly restrict the relative increase of surface lake volumes. In fact, the relative increase in surface lake volumes is higher than average in all three of the aforementioned catchments (Table 4.3). Regional variations in catchment-wide surface lake volumes also do not correlate well with the size of the ablation area (Fig. 4.7B). This implies that the volume of surface lakes in a certain catchment is not strongly dependent on the size of the ablation area within the same catchment; e.g. NE Greenland has a relatively small ablation area but a high percentage of the total surface lake volume throughout the study period (Table 4.3 and Table 4.4). Furthermore, the correlation between the catchment-wide volume of surface lakes and the size of the ablation area is smaller in the future and in the case of the more severe climate change scenario, i.e. RCP 8.5 (Fig. 4.7B).

Table 4.5 Reconstructed and projected mean probability of rapid lake drainage, and the relative change of rapid lake drainage probability in each catchment of the GrIS during the 21st century compared to 1980-2009. The number of lakes and the relative change of lake numbers are also included.

	N	NE	E	SE	S	SW	W	NW	Total
Rapid drainage probability: 1980-2009	0.14	0.17	0.26	0.33	0.23	0.07	0.19	0.24	**0.20**
Rapid drainage probability: 2070-2099 RCP 4.5	0.10	0.12	0.22	0.27	0.17	0.06	0.16	0.20	**0.16**
Rapid drainage probability: 2070-2099 RCP 8.5	0.08	0.10	0.19	0.24	0.15	0.05	0.15	0.18	**0.14**
Relative change of rapid drainage probability: 2070-2099 RCP 4.5 (%)	-27	-28	-17	-17	-23	-18	-16	-18	**-20**
Relative change of rapid drainage probability: 2070-2089 RCP 8.5 (%)	-38	-43	-27	-26	-33	-23	-23	-26	**-29**
Lake number: 1980-2009	702	440	487	117	111	1627	667	1064	**5216**
Lake number: 2070-2099 RCP 4.5	1032	837	1054	267	215	2276	959	1550	**8190**
Lake number: 2070-2099 RCP 8.5	1184	1076	1434	342	264	2496	1098	1756	**9650**
Relative change of lake number: 2070-2099 RCP 4.5 (%)	47	90	116	129	93	40	44	46	**57**
Relative change of lake number: 2070-2099 RCP 8.5 (%)	69	144	194	193	137	53	65	65	**85**

In parallel with the inland expansion of surface lakes, the ice sheet-wide mean probability of rapid lake drainage – calculated by combining the probability of hydrofracture and surface crack formation (Section 4.2.1.2) – is predicted to decrease

from around 0.2 to 0.16-0.14 during the 21st century (Fig. 4.8, Table 4.5). The contemporary and projected probabilities of rapid lake drainage are smallest in the SW, and the highest in the SE (Fig. 4.8). The relative decrease in the probability of rapid drainage during the 21st century is similar in most catchments – between 17-23% (RCP 4.5) and 23-33% (RCP 8.5) (Fig. 4.8, Table 4.5). However, in the N and NE catchments the decrease is considerably higher than average – 27-28% (RCP 4.5) and 38-43% (RCP 8.5) respectively (Table 4.5) – mostly due to the strong decrease in the potential for surface crack formation with elevation (Fig. 4.4). Furthermore, the contemporary rapid lake drainage probability is also lower than average in these catchments (Fig. 4.8, Table 4.5). Therefore, the probability of rapid lake drainage is predicted to become relatively low in these catchments by the end of the century, 0.1-0.12 (RCP 4.5) and 0.8-0.1 (RCP 8.5) respectively (Fig. 4.8, Table 4.5). Although the overall probability of rapid lake drainage decreases, the number of surface lakes increases during the 21st century (Table 4.5). As the relative increase in lake number (Table 4.5 row 4-5) is larger than the relative decrease in rapid drainage probability (Table 4.5 row 9-10), the overall frequency of rapid lake drainage is likely to increase during the 21st century in every catchment of the GrIS.

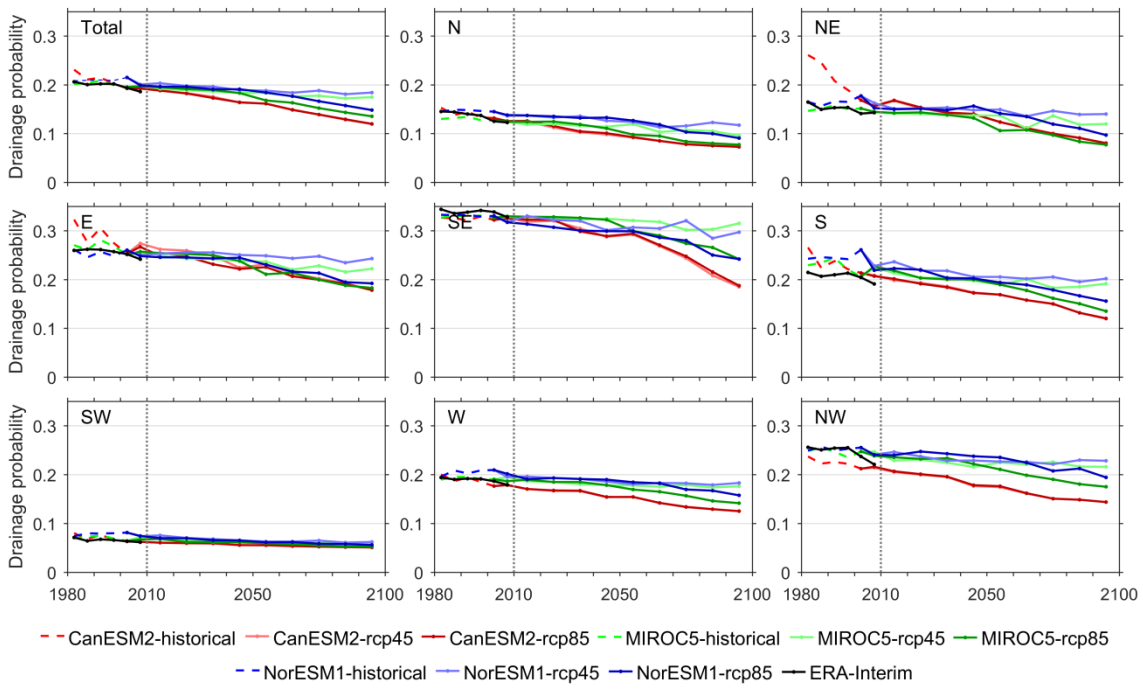

Figure 4.8 Ice sheet-wide and catchment specific reconstruction and projection of the probability of rapid lake drainage for the period of 1980–2099 using various climate model outputs. The dashed vertical lines on all panels represent the year 2010.

4.3.2. Surface lake projections with evolving ice surface topography

4.3.2.1. Evolution of the GrIS between 1980-2300, context from ice sheet model outputs

As the bed-to-surface transfer – and consequently the surface relief – is strongly influenced by the ice thickness and basal slip ratio, first I discuss the evolution of these parameters obtained from the ice sheet model outputs (Vizcaino et al., 2014) for 1980-2300. Generally, the GrIS thins between 1980 and 2300 (Fig. 4.9, Table 4.6). Although the ice sheet-wide mean decrease in ice thickness is modest during the 21st century, 5.8-9.2 m compared to 1980-1999 (Table 4.6), the rate of decrease speeds up after 2100, leading to a mean ice thickness decrease of 92.52 m by 2300 (Table 4.6). This trend is also reflected in the means and medians of the relative changes in ice thickness, except in the case of the moderate climate change scenario during the 21st century (Table 4.6). Conversely to ice thickness, the ice sheet-wide mean basal slip ratio increases between 1980 and 2300 (Fig. 4.10, Table 4.6). This increase is moderate (0.22-0.27) during the 21st century, but accelerates (2.19) between 2100 and 2300 (Table 4.6). Although relative changes in basal slip ratio generally reflect this trend, the means are distorted due to a small number of very high relative local changes. This is not surprising, as basal slip ratios commonly attain values close to zero, especially in the interior of the ice sheet (Fig. 4.10), thus even small absolute changes can lead to very high relative changes.

Table 4.6 The mean, median and standard deviation of the difference and relative difference of the ice thickness and basal slip ratio for different time periods, compared to 1980-1999.

Ice thickness	Difference (m)			Relative difference (%)		
	Mean	Median	Std. deviation	Mean	Median	Std. Deviation
2080-2099 (RCP 4.5)	-5.76	1.58	23.22	-1.72	0.06	14.14
2080-2099 (RCP 8.5)	-9.20	-0.15	26.01	-2.46	-0.01	13.06
2280-2299 (RCP 8.5)	-92.59	-59.89	125.46	-9.69	-3.27	20.48
Basal slip ratio	**Difference**			**Relative difference (%)**		
	Mean	Median	Std. deviation	Mean	Median	Std. Deviation
2080-2099 (RCP 4.5)	0.27	0.00002	5.13	1755	0.60	52755
2080-2099 (RCP 8.5)	0.22	0.00004	4.70	906	0.82	30015
2280-2299 (RCP 8.5)	2.19	0.00120	8.98	5000	11.92	79424

Significant relative ice thinning is restricted to areas close to the ice sheet margin during the 21st century, though in the W-NW and NE these areas extend farther inland (Fig. 4.9). Elsewhere on the GrIS, relative ice thickness change is minimal during the 21st century, except for some small areas – most notably individual outlet glaciers along the E and S coastline – where thickness is predicted to increase considerably (Fig. 4.9). However, between 2100 and 2300 greater areas experience large relative ice thinning, especially in the W-NW, N, NE and SE (Fig. 4.9), while a small relative increase is also predicted in the interior of the N, E and S sections of the GrIS (Fig. 4.9). The basal slip ratio changes considerably over relatively large areas of the GrIS – especially in the W, NW, N, NE and SE – even during the 21st century (Fig. 4.10). Generally, the basal slip ratio increases during the 21st century, though it also decreases in smaller regions close to the ice sheet margin in most sections of the GrIS (Fig. 4.10). Between 2100 and 2300 the magnitude of the relative basal slip ratio increase is greater than during the 21st century (Fig. 4.10), while the spatial pattern of the increase does not change significantly, except for a 100-250 km inland expansion in the N and NE (Fig. 4.10). However, the basal slip ratio only decreases close to the ice sheet margin in S, E and N Greenland between 2100 and 2300, conversely to the 21st century when basal slip ratio decrease is prevalent along the entire margin of the ice sheet (Fig. 4.10).

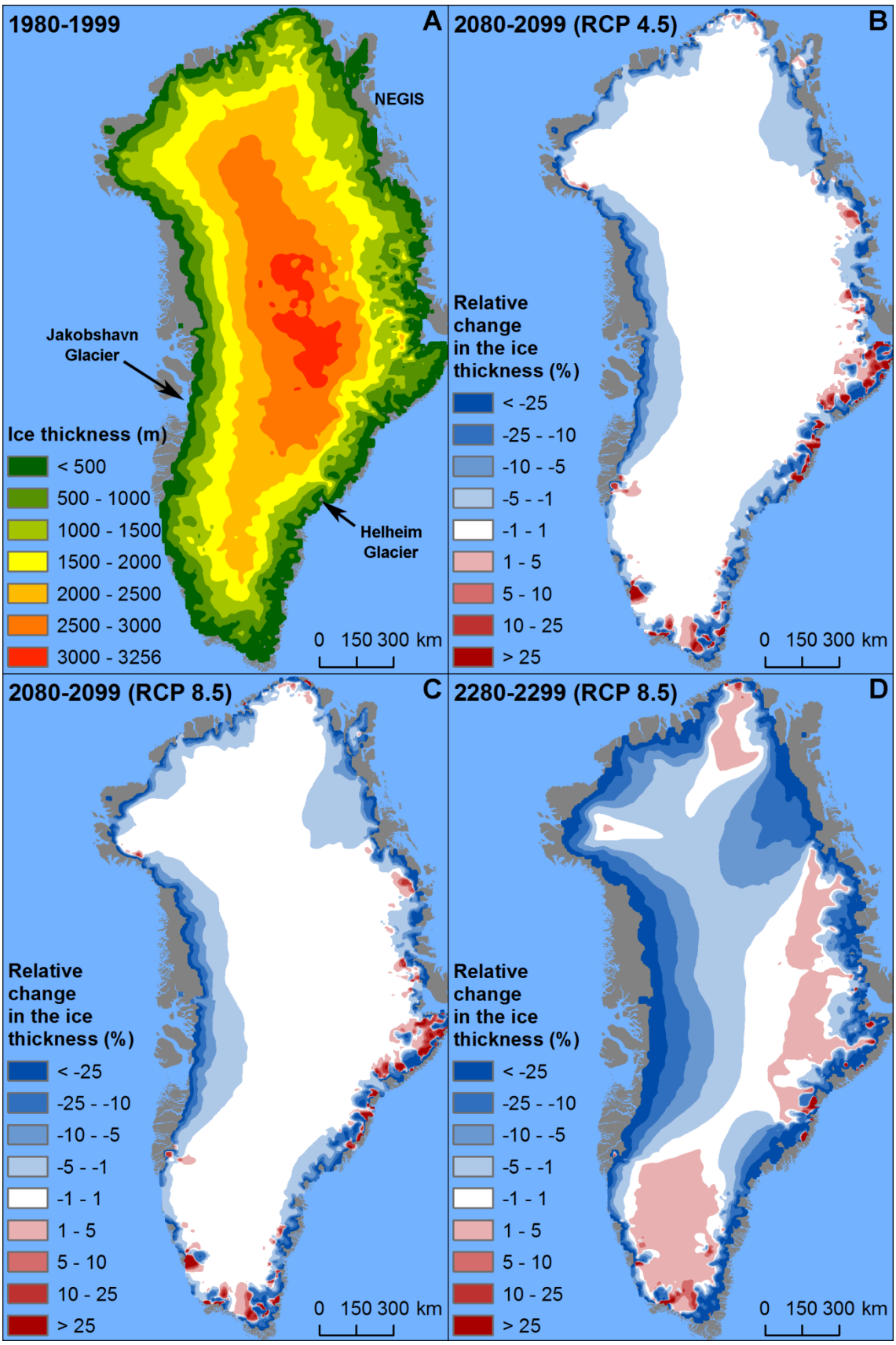

Figure 4.9 (A) Ice thickness of the GrIS calculated by the SICOPOLIS ice sheet model for 1980-1999. (B-D) Relative changes of the ice thickness compared to 1980-1999.

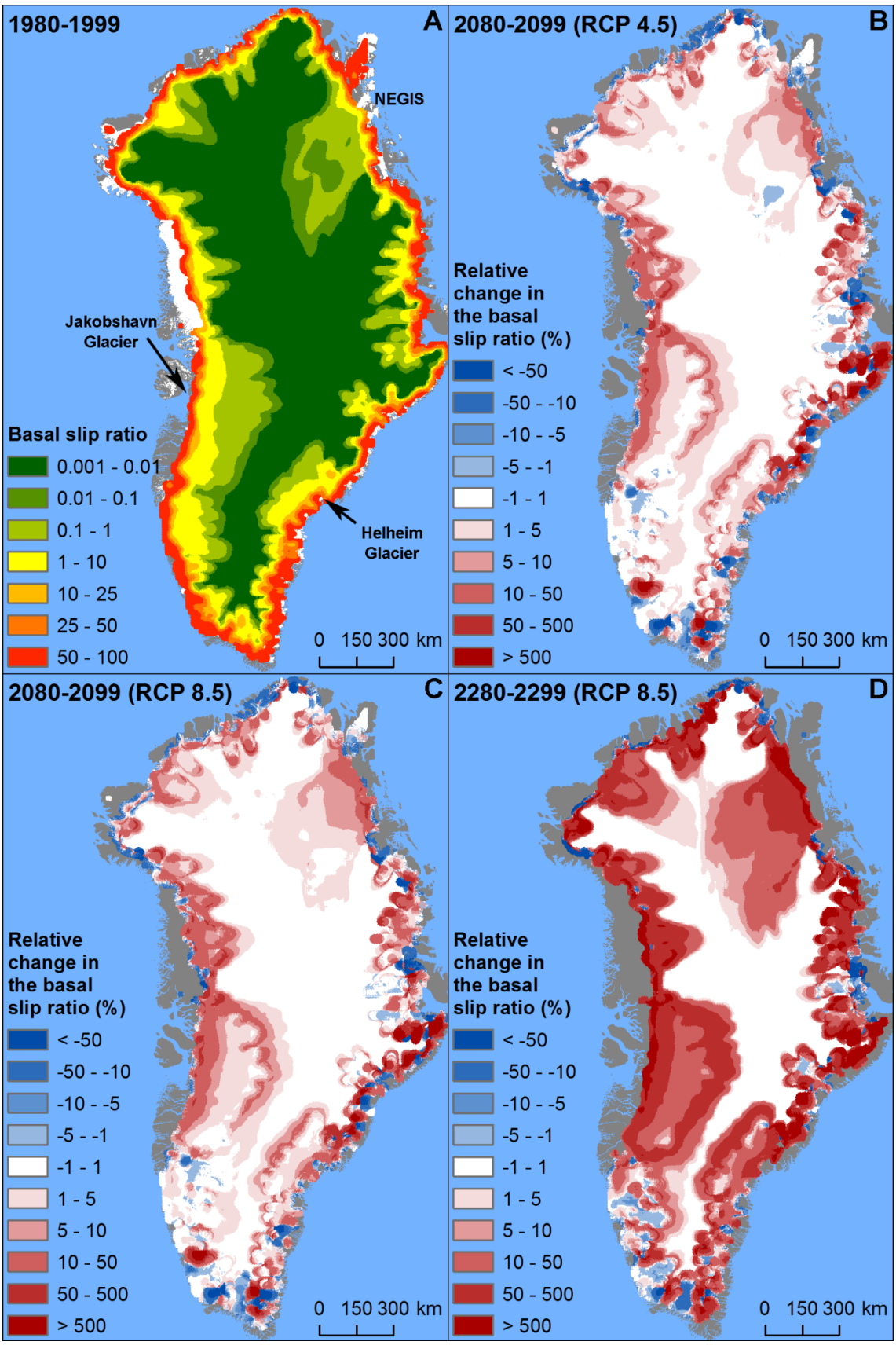

Figure 4.10 (A) Basal slip ratio of the GrIS calculated by the SICOPOLIS ice sheet model for 1980-1999. (B-D) Relative changes of the basal slip ratio compared to 1980-1999.

4.3.2.2. Changing surface relief of the GrIS between 1980-2300

The large-scale spatial distribution of predicted mean surface relief derived from SICOPOLIS 3.0 ice sheet model outputs (Vizcaino et al., 2014) is similar for all time-slices (Fig. 4.11). Generally, the mean surface relief decreases towards the interior of the GrIS. However, high surface relief extends far from the margins in the NW, W and NE segments of the ice sheet (e.g. upstream Jakobshavn Glacier, Northeast Greenland Ice Stream) (Fig. 4.11). This pattern is very similar to the large-scale spatial distribution of the observed and predicted mean surface relief of the contemporary GrIS (Section 2.3.2). This gives confidence in the ability of the approach to project the future surface relief of the GrIS.

Although there is little apparent change between the predicted mean surface relief of 1980-1999 and 2280-2299 (RCP 8.5) (Fig. 4.11), closer investigations reveal distinct trends (Fig. 4.12). In general, the predicted surface relief increases between 1980 and 2300 (Table 4.7), although there are also examples of stagnation or slight decreases in certain smaller regions, mostly in S and E Greenland, and very close to the ice sheet margin elsewhere (Fig. 4.12). Changes in surface relief are modest during the 21st century, with an ice sheet-wide mean surface relief increase of +0.37 m for the moderate (RCP 4.5) and +0.46 m for the high (RCP 8.5) climate change scenario, compared to 1980-1999 (Table 4.7). These changes represent relative increases of +2.63% and +3.52% respectively (Table 4.7). However, surface relief change accelerates substantially after 2100, as the ice sheet-wide mean surface relief increases +6.9 m by 2300 (RCP 8.5) compared to 1980-1999, representing a relative increase of +36.4% (Table 4.7).

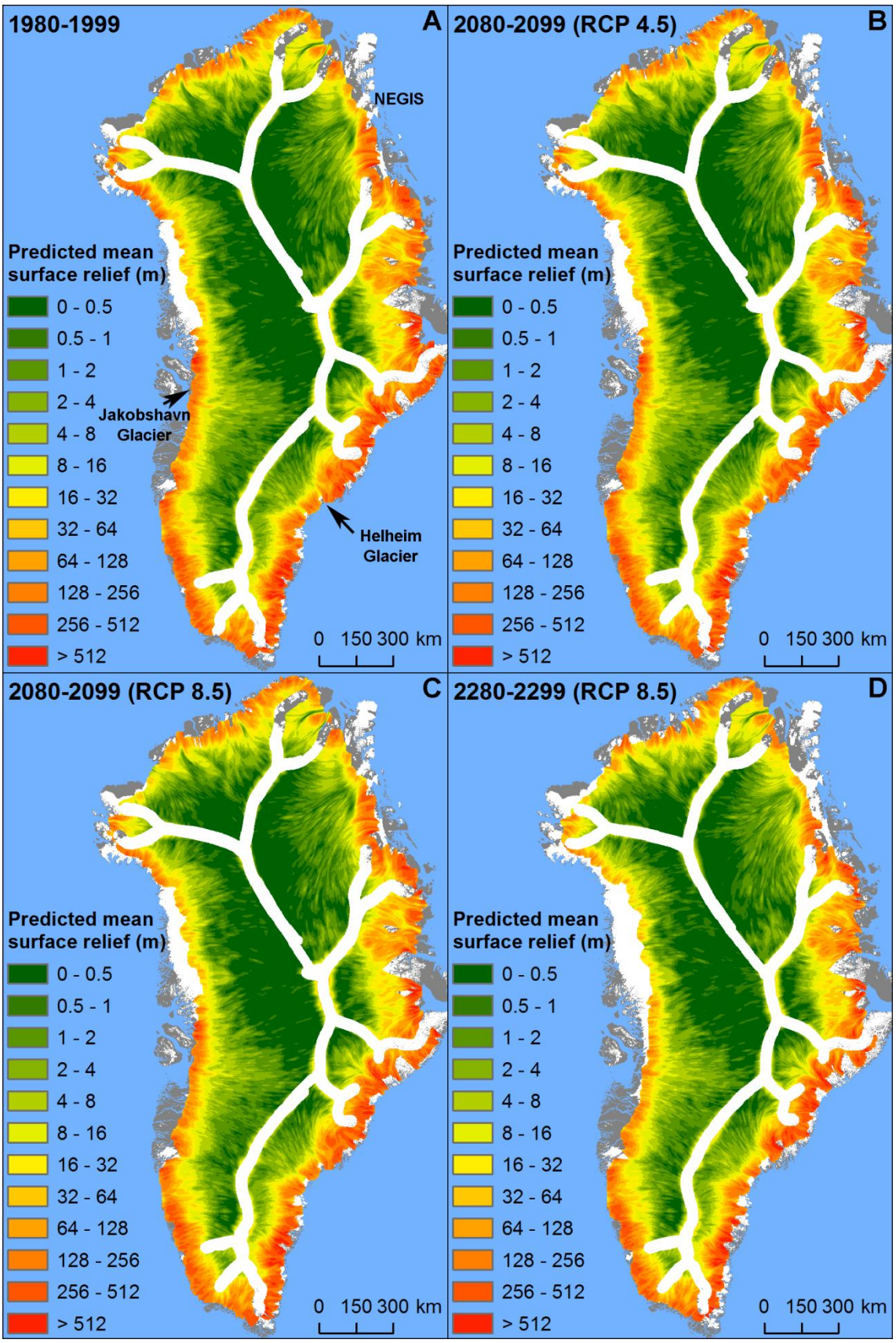

Figure 4.11 (A-D) Predicted mean surface relief of the GrIS, calculated using SICOPOLIS ice sheet model outputs for different time periods.

Table 4.7 The mean, median and standard deviation of the difference and relative difference of the predicted surface relief for future time periods, compared to 1980-1999.

	Difference (m)			Relative difference (%)		
	Mean	Median	Std. deviation	Mean	Median	Std. Deviation
2080-2099 (RCP 4.5)	0.37	0.01	19.07	2.63	1.66	14.01
2080-2099 (RCP 8.5)	0.46	0.02	19.78	3.52	2.49	15.19
2280-2299 (RCP 8.5)	6.90	0.29	35.84	36.40	22.47	65.45

Besides the ice sheet-wide trends, the changing surface relief also exhibits different regional tendencies. By 2100, the surface relief is predicted to increase considerably along the western edge of the GrIS, relatively close to the ice sheet margin, and on several outlet glaciers of the East Greenland coast (Fig. 4.12A-B, D-E). Compared to 1980-1999, this increase will generally be in the order of 0.5-10 m (Fig. 4.12A-B), though values as high as 10-100 m are found closer to the ice sheet margin (Fig. 4.12A-B). However, these changes rarely exceed +75% in relative terms during the 21st century (Fig. 4.12D-E). Between 2100 and 2300 surface relief increases extend to larger areas of the GrIS, and the magnitude of the increase is also predicted to become greater, though the S and E segments of the GrIS remain largely exempt from this (Fig. 4.12C, F). The surface relief increases by 10-100 m over large areas along the margins of the GrIS by 2300 (Fig. 4.12C). Furthermore, in certain regions – e.g. Jakobshavn Glacier and Helheim Glacier – the increase is higher than 100 m (Fig. 4.12C). Relatively, these changes exceed +75% over vast areas of the GrIS (Fig. 4.12F). Although the increase is generally smaller towards the interior of the GrIS (Fig. 4.12C, F), the surface relief is predicted to increase considerably – by 0.5-10 m – far from the ice sheet margin in the SW-W and NE segment of the ice sheet by 2300 (Fig. 4.12C). This is especially apparent in the NE, where large relative surface relief increases of >75% are expected in the vicinity of the ice sheet divide by 2300 (Fig. 4.12F).

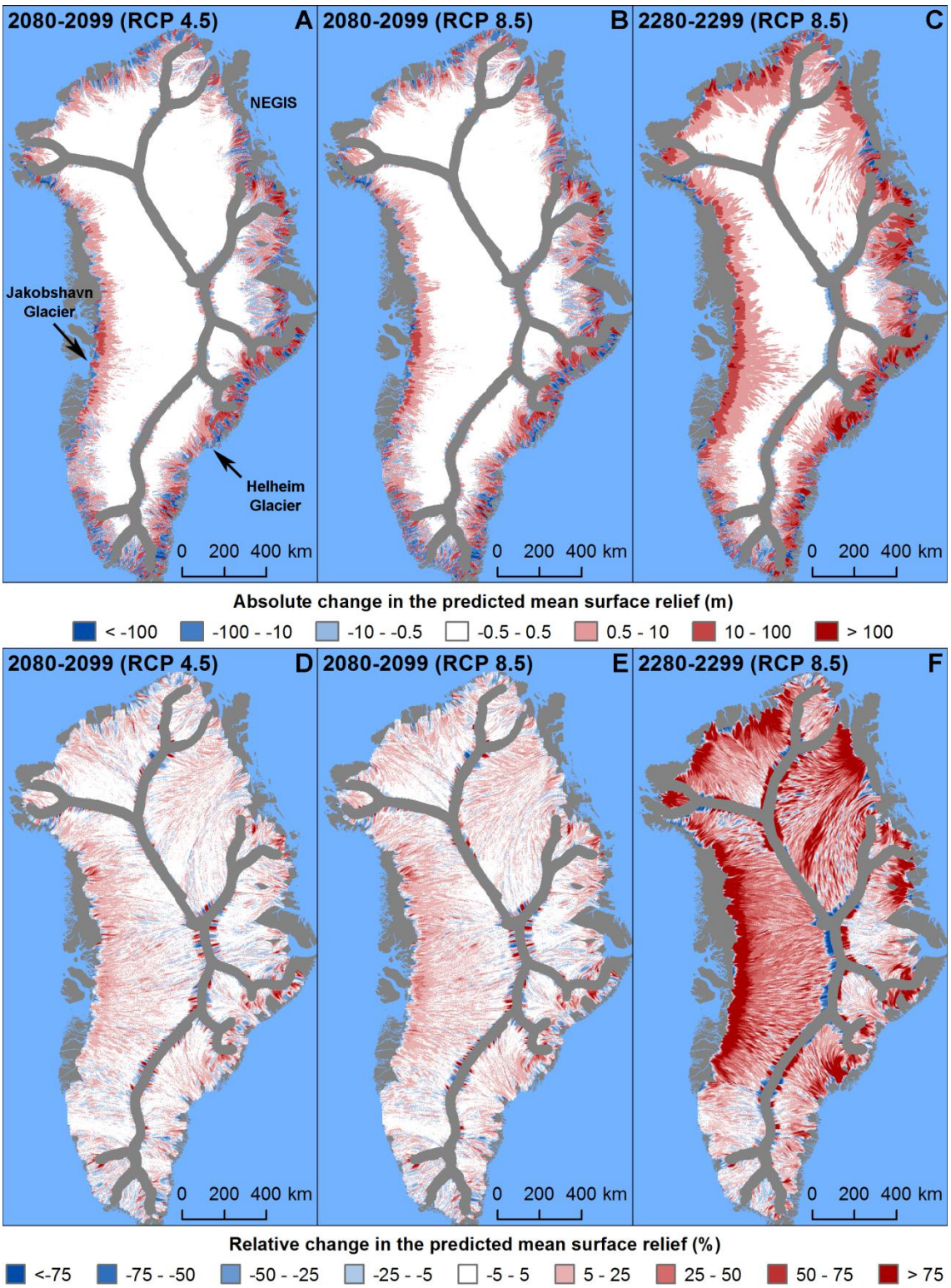

Figure 4.12 (A-C) Absolute and (D-F) relative change in the predicted mean surface relief of the GrIS, calculated from SICOPOIS ice sheet model outputs, compared to 1980-1999.

4.3.2.3. The accuracy of surface depression volumes calculated from the surface relief

Here I test the ability to estimate the total depression volume of the GrIS from mean surface relief datasets (outlined in Section 4.2.2.2). Based on my results, the total volume of the surface depressions on the GrIS – derived directly from the GIMP-DEM (Section 3.2.2.1) – can be estimated with an acceptable degree of underestimation: 35.6-37% (Table 4.8) from the predicted surface relief of the contemporary GrIS (created in Chapter 2). Normalising the total depression volumes – which accounts for the incomplete spatial coverage of the surface relief dataset – further enhances the match and yields an underestimation of 23.9-25.5% (Table 4.8).

Furthermore, the total depression volume of the contemporary GrIS – derived directly from the GIMP-DEM – can be estimated with similar precision from the predicted surface relief dataset calculated using SICOPOLIS (1980-1999) ice sheet model outputs. In this case the underestimation is 24%, and 21% after normalising the total depression volumes (Table 4.8). Hence, I conclude that the future volume of GrIS surface depressions can be inferred from the surface relief – using the empirical relationships derived in Chapter 3 – even when the surface relief is calculated using modelled ice sheet geometry.

Table 4.8 The total volume of surface depressions on the GrIS was estimated by converting the contemporary predicted surface relief dataset (created in Chapter 2) and the surface relief derived from SICOPOLIS 1980-1999 outputs. The total volume of surface depressions was also calculated directly from the GIMP-DEM. The total depression volumes were normalised by the area of the corresponding domain.

	Depression volume (km^3)	Depression volume normalised by the domain area (mm)
Predicted contemporary surface relief	111.8	76.8
SICOPOLIS 1980-1999 surface relief	132.0	79.7
Directly derived from GIMP-DEM	173.6	100.9

4.3.2.4. Changing surface depressions on the GrIS between 1980-2300

As surface depressions delineate the sites of potential surface lakes, first I discuss the changing future distribution of surface depressions caused by the changing surface relief on the GrIS. The predicted surface relief (Fig. 4.11) – corresponding to different ice sheet model time-slices (Vizcaino et al., 2014) – was converted to net surface depression volume, according to the approach outlined in Section 4.2.2.2 (Fig

4.13). As the depression volume is controlled by the surface relief (Chapter 3), the large-scale distribution of depressions is similar to the large-scale distribution of the surface relief (Fig. 4.11). However, as high surface relief limits the formation of closed surface depressions (Chapter 3), the highest depression volumes are attained slightly inland from the margin of the ice sheet (Fig. 4.13A). In general, the surface depression volume decreases rapidly away from the ice sheet margin (Fig. 4.13A). However, the W and NE sections of the GrIS (i.e. upstream Jakobshavn Glacier and the Northeast Greenland Ice Stream respectively) maintain high surface depression volumes far from the ice sheet margin (Fig. 4.13A).

Table 4.9 The total volume of surface depressions on the GrIS, calculated from the predicted surface relief datasets which were derived from different SICOPOLIS time-slices. The total volume of surface depressions are also normalised by the corresponding area of the predicted surface relief dataset, producing a unit (i.e. mm) independent of ice sheet area. Relative changes – compared to the 1980-1999 – are calculated as well.

	Total depression volume (km^3)	Relative change (%)	Total depression volume normalised by the domain area (mm)	Relative change (%)
1980-1999	132.0		79.7	
2080-2099 (RCP 4.5)	131.1	-0.7	79.8	0.2
2080-2099 (RCP 4.5)	130.7	-1.0	79.9	0.2
2280-2299 (RCP 8.5)	124.2	-5.9	80.8	1.4

Despite the general increase in surface relief on the GrIS during 1980-2300 (Section 4.3.2.2), the total volume of surface depressions decreases slightly (-0.7-1% compared to 1980-1999) by 2100, and moderately (-5.9%) by 2300 (Table 4.9). I attribute the decrease in the total volume of surface depressions on the GrIS to the shrinking size of the ice sheet. This is supported by the predicted increase in the normalised depression volume during 1980-2300 (Table 4.9), which is unaffected by the size of the ice sheet as the total depression volumes are normalised by the area of the corresponding predicted surface relief datasets. The increase in the normalised depression volume is very small (0.2%) during 1980-2100, but increases slightly (1.4%) during 2100-2300 (Table 4.9).

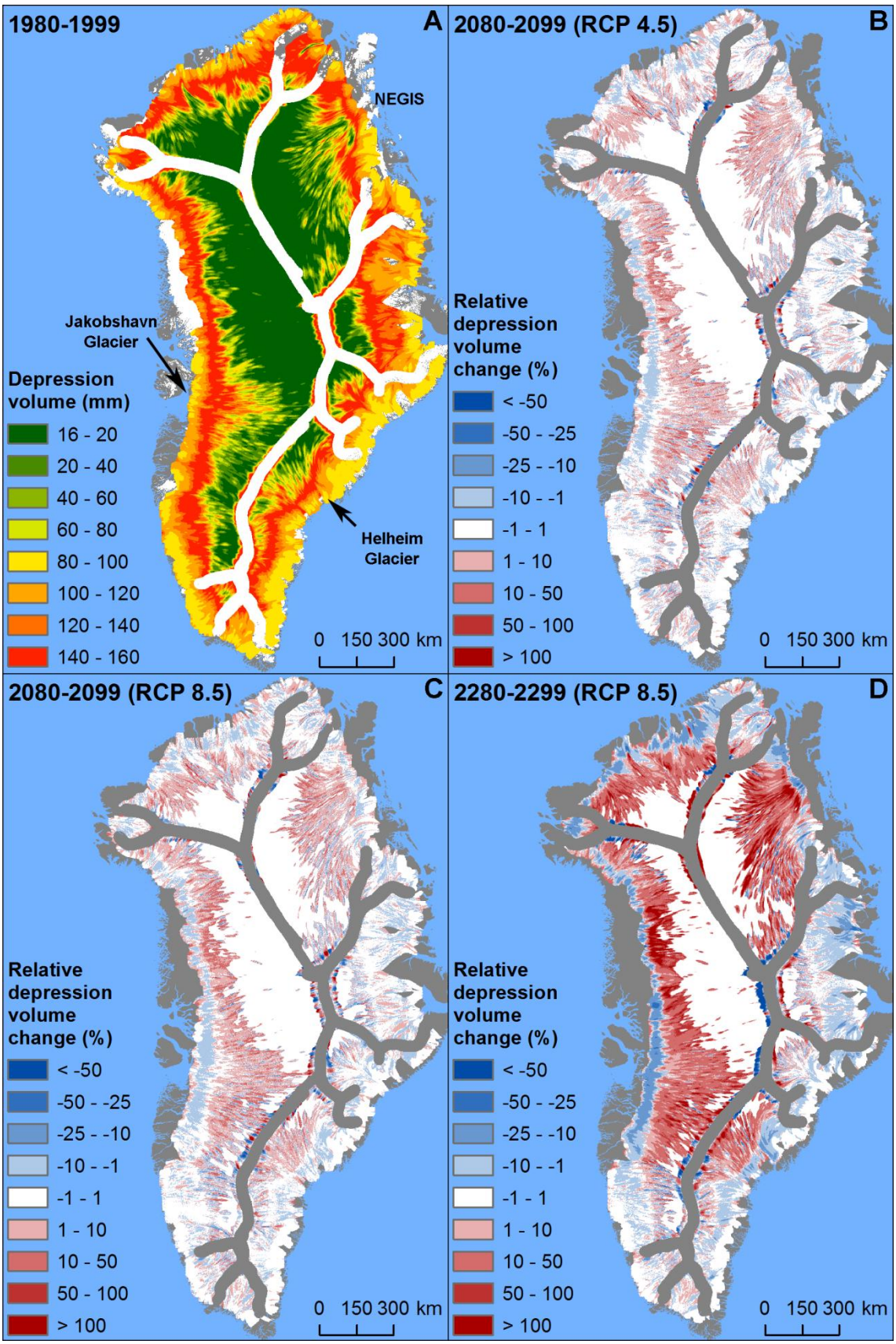

Figure 4.13 (A) The distribution of surface depressions on the GrIS, calculated using SICOPOLIS ice sheet model outputs for 1980-1999. The raw net surface depression volume raster (volume of depressions in a particular cell) was normalised by the cell area to produce a unit, independent of the raster resolution, for the map. (B-D) Relative changes in the net depression volume on the GrIS compared to 1980-1999.

Although the ice sheet-wide total volume of surface depressions – especially after correcting for the effects of the shrinking size of the ice sheet – is relatively stable during 1980-2300 (Table 4.9), the volume of surface depressions changes considerably in certain regions of the GrIS, especially after 2100 (Fig. 4.13). Close to the ice sheet margin across most of the GrIS, surface depression volume decreases by 10-25% during 1980-2300 though this change remains relatively modest (-1 to -10%) up until 2100 (Fig. 4.13). Conversely, the volume of surface depressions increases towards the interior (Fig. 4.13); typical increases of 1-10% (and not exceeding 50%) are predicted by 2100 (Fig. 4.13B-C), rising to 10-100% over large areas of the ice sheet by 2300 and exceeding 100% in the NW and NE (Fig. 4.13D). The S and E sections of the GrIS are largely insensitive to changes, showing an average overall decrease of ~1-10% in surface depression volume (Fig. 4.13). It is also important to note that the typical volume of individual surface depressions decreases across the GrIS during 1980-2300 (Fig. 4.14). Hence, the increasing total depression volume, discussed above, is caused by the increasing relative spatial coverage – i.e. density – of surface depressions.

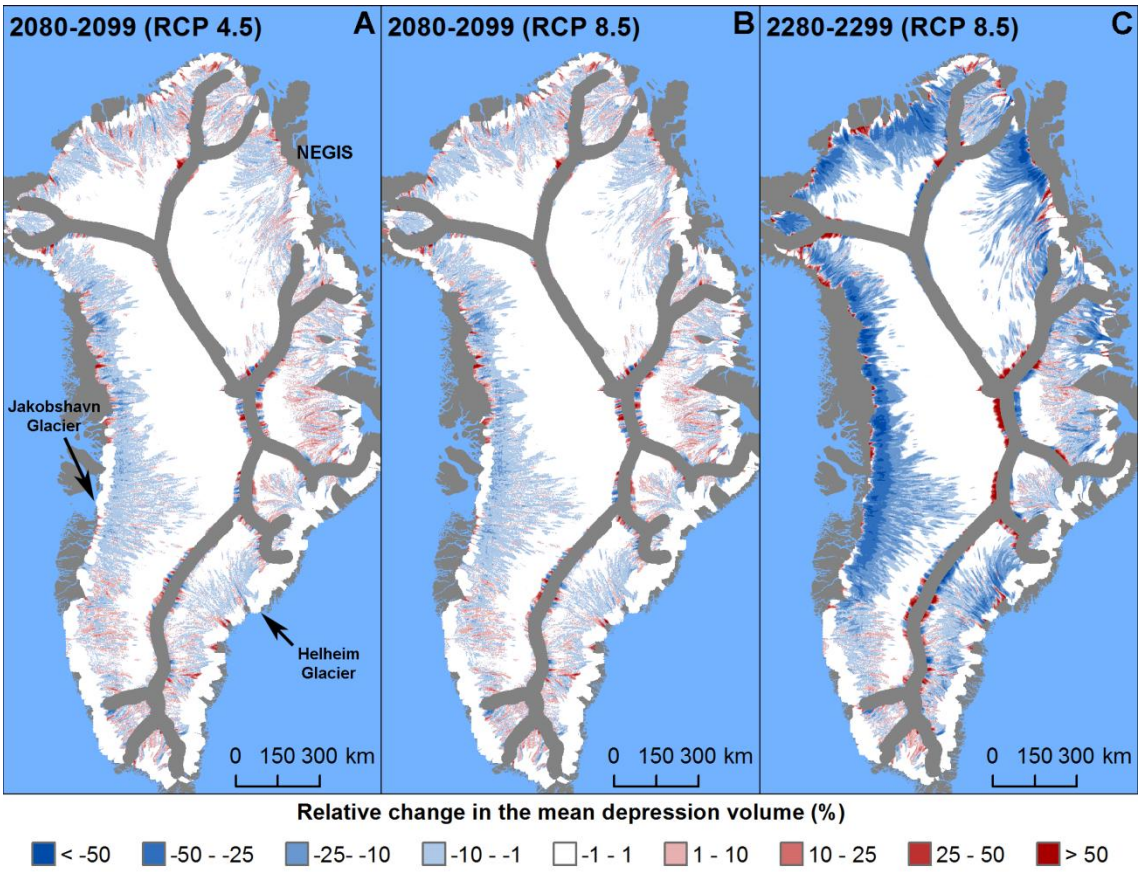

Figure 4.14 (A-C) Relative changes in the mean depression volume on the GrIS compared to 1980-1999.

4.3.2.5. Changing surface lakes on the GrIS between 1980-2300

The distribution of surface lakes is directly controlled by the distribution of surface depressions and surface mass balance, as the formation of surface lakes requires closed surface basins and sufficient runoff (Sections 1.2.2 and 3.3.1). Here I focus on the interplay between the changing ELA – obtained from the SICOPOLIS ice sheet model outputs (Vizcaino et al., 2014) – and changing surface depression volume, which is controlled by the changing surface relief (Section 4.3.2.4). Surface lakes – inferred from surface relief and SMB derived from SICOPOLIS outputs – are restricted to areas relatively close to the ice sheet margin over most of the GrIS during 1980-1999 (Fig. 4.15A). However, surface lakes expand considerably towards the ice sheet interior in the W, NW, N and NE sections of the GrIS by 2100 due to the rising ELA, especially in the case of a high climate change scenario (RCP 8.5) (Fig. 4.15B-C). The expansion of the ablation area during the 21st century predominantly affects regions where surface depressions – and thus surface lakes – have high volumes (Figs. 4.13 and 4.15B-C). After 2100, the ELA rises further causing the ablation area to expand to almost the entire NW half of the GrIS by 2300, though in the S, SW and E sections this expansion is more limited (Fig. 4.15D). Although the ablation area expands substantially during 2100-2300, this mostly affects regions where the surface depression and lake volumes are relatively low (Figs. 4.13 and 4.15D), which could limit the overall increase in surface lake volume during 2100-2300.

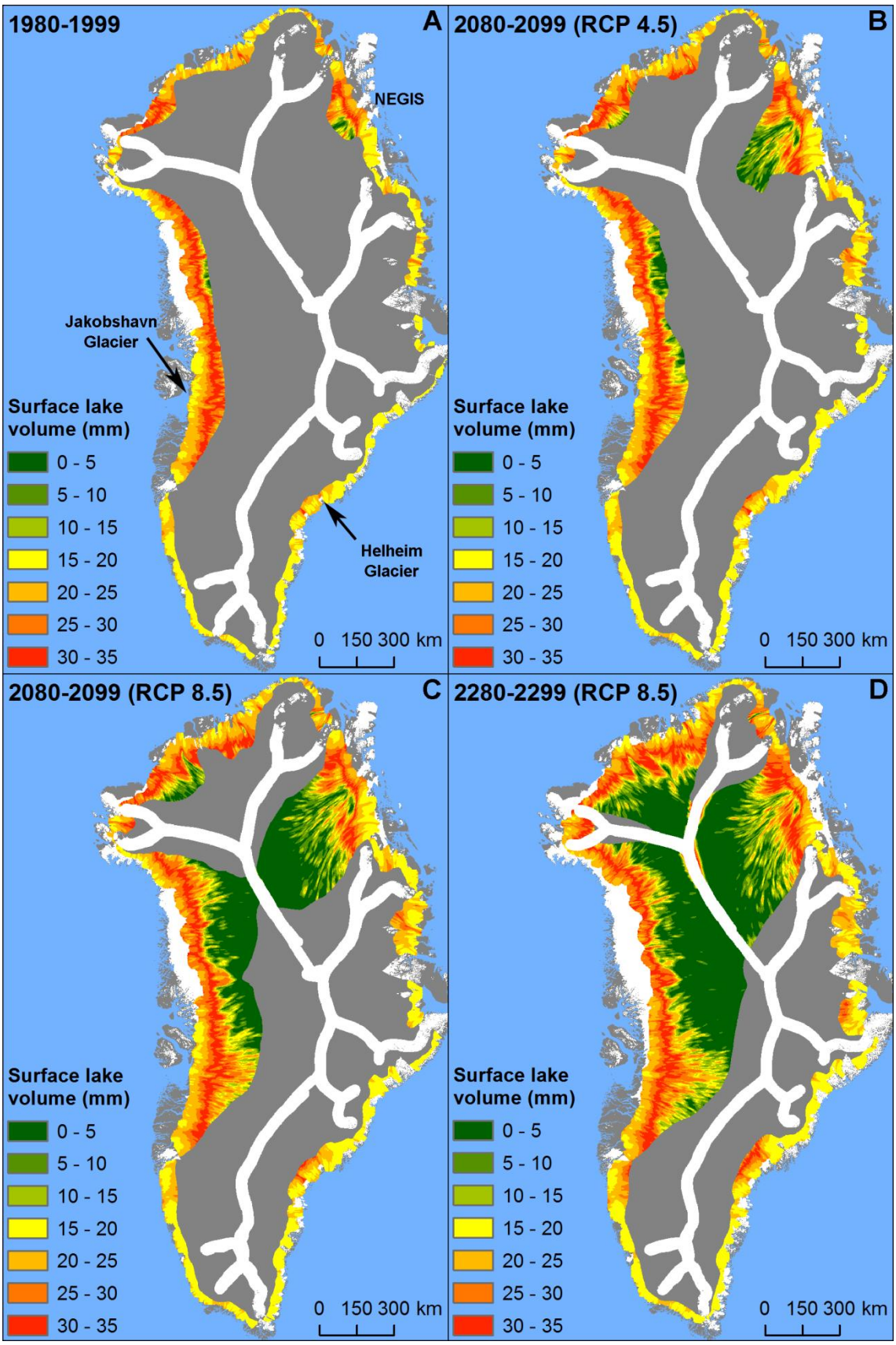

Figure 4.15 (A-D) The distribution of surface lakes on the GrIS, calculated using SICOPOLIS ice sheet model outputs for different time-slices. The raw net lake volume rasters (volume of lakes in a particular cell) were normalised by the cell area to produce a unit (i.e. mm), independent of the raster resolution, for the maps. The grey mask delineates areas above the ELA, where surface lake formation is not expected.

The maximum volume of meltwater that could be contained in surface lakes – during a given melt season – increases by 42.4 and 78.6% by 2100, compared to 1980-1999, under moderate (RCP 4.5) and high (RCP 8.5) climate change scenarios, respectively (Table 4.10). By 2300, the total volume of surface lakes is predicted to increase by 112.6%, but the rate of increase slows down after 2100 (Table 4.10). However, these figures are somewhat biased by the shrinking size of the GrIS. Accordingly, the increase in the normalised surface lake volume – which is unaffected by the size of the GrIS – is 1.3-2.3% higher than the increase in the total surface lake volume by 2100, but 16.6% higher by 2300 (Table 4.10). Evolving ice surface topography – and surface relief – also exerts a temporally varying degree of control on the volume of surface lakes. Although keeping the surface relief constant only causes a small (0.8-1.7%) underestimation of the total surface lake volume by 2100, this becomes more significant (13.3%) by 2300 (Table 4.10). Changing surface relief affects the normalised surface lake volumes even more strongly than the total surface lake volume. Neglecting the effects of the changing surface relief leads to a 0.8-1.8% underestimation of the increase of normalised surface lake volume by 2100, but this rises to 14.4% by 2300 (Table 4.10). As the distribution of surface depressions preconditions the distribution of surface lakes (e.g. Section 3.3.1), the effect of changing surface relief on surface lakes is the largest in regions where the increase in surface depression volume is the highest, e.g. in certain regions of the W, NW and NE it could be as high as ~100% by 2300 (Fig. 4.13, Section 4.3.2.4).

Table 4.10 The total volume of surface lakes on the GrIS – calculated using surface relief projections and modelled surface mass balance derived from SICPOLIS outputs – at different time periods. To investigate the influence of evolving surface topography on surface lake formation, the total volume of surface lakes are also calculated using a constant surface relief – set at the 1980-1999 level, derived from SICOPOLIS outputs – but changing surface mass balance. The total volume of surface lakes – calculated with both changing and constant surface relief – are normalised by the corresponding area of the predicted surface relief dataset. The relative changes – compared to the 1980-1999 – are also calculated.

	Changing surface relief		Constant surface relief	
Total lake volume	**Volume (km^3)**	**Relative change (%)**	**Volume (km^3)**	**Relative change (%)**
1980-1999	7.0			
2080-2099 (RCP 4.5)	9.9	42.4	9.9	41.6
2080-2099 (RCP 8.5)	12.5	78.6	12.4	76.9
2280-2299 (RCP 8.5)	14.9	112.6	13.9	99.3
Total lake volume normalised by the domain area	**Volume (mm)**	**Relative change (%)**	**Volume (mm)**	**Relative change (%)**
1980-1999	4.2			
2080-2099 (RCP 4.5)	6.1	43.7	6.0	42.9
2080-2099 (RCP 8.5)	7.6	80.9	7.5	79.1
2280-2299 (RCP 8.5)	9.7	129.2	9.1	114.8

Ice sheet model outputs for the period 1980 to 2300 have also been used to assess the potential for hydrofracture and surface crack formation (Section 4.2.2.2). The relative spatial coverage of high extensive principal strain rates (i.e. above +0.005 yr^{-1}) below the ELA – which indicate regions where the potential for surface crack presence is high – declines sharply during the 21st century, from 18.1% (1980-1999) to 9.4-14% (2080-2099 RCP 8.5 and 4.5 respectively) (Table 4.11). However, this decrease slows after 2100 as the relative coverage of high extensive principal strain rates below the ELA only decreases to 7.2% by the end of the 23rd century (Table 4.11). According to my experiments, which consider average depression dimensions and elastic fracture mechanics (Section 4.2.2.2), hydrofracture at an average depression below the ELA is likely or possible across the GrIS for all time-slices considered (Fig. 4.16). However, the potential for hydrofracture is not uniform across the GrIS. It is less likely in the interior of the ice sheet than closer to the margin, though the ELA only extends sufficiently far inland for this to be relevant at/after the end of the 21st century (Fig. 4.16). Although the area of likely hydrofracture expands inland during 1980-2300, the spatial coverage of this expansion is small (Fig. 4.16).

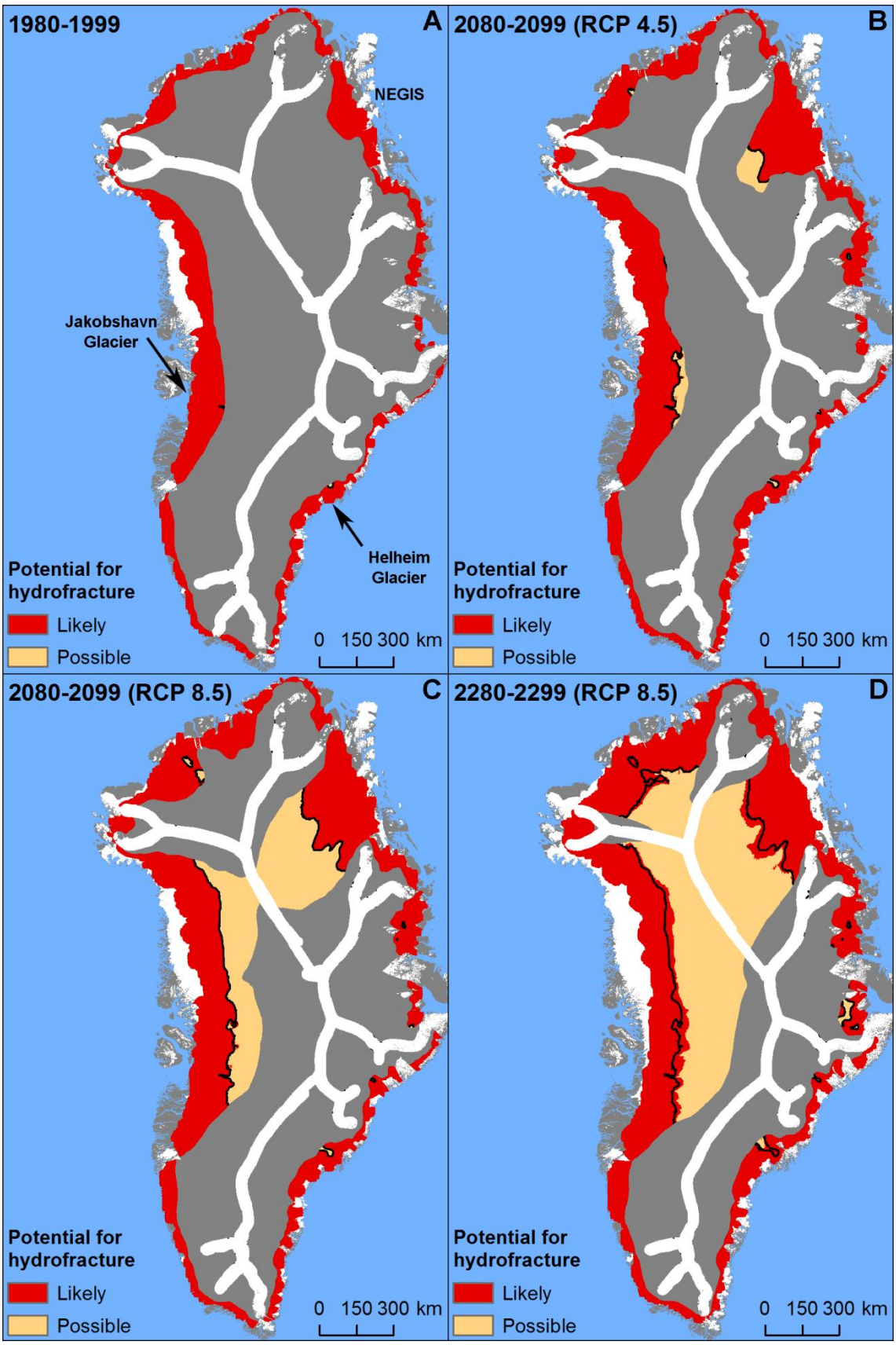

Figure 4.16 The potential for hydrofracture at typical surface depressions, whether an average depression could contain enough meltwater to propagate a surface crack to the ice sheet bed. The boundary between likely and possible hydrofracture during 1980-1999 is indicated (solid black line) on all three projections. The grey mask delineates areas above the relevant ELA.

Table 4.11 Size of the ablation area, the absolute and relative coverage of principal strain rates above +0.005 below the ELA; calculated from SICOPOLIS outputs.

	Ablation area (km^2)	Coverage of principal strain rates above +0.005 yr^{-1} below the ELA (km^2)	Coverage of principal strain rates above +0.005 yr^{-1} below the ELA (%)
1980-1999	302740	54675	18.1
2080-2099 (RCP 4.5)	461207	64700	14.0
2080-2099 (RCP 4.5)	721351	67475	9.4
2280-2299 (RCP 8.5)	969890	69975	7.2

4.4. Discussion

First I discuss the changing surface relief of the GrIS and the effect this exerts on the distribution and total volume of surface lakes (Section 4.4.1). Then, I move on to discuss two different projections of surface lake distribution, one assuming fixed surface relief between 1980 and 2100 (Section 4.4.2) and one which incorporates the effects of changing surface relief between 1980 and 2300 (Section 4.4.3). Although the projection incorporating the effects of changing surface relief is more comprehensive, fixed surface topography – and consequently surface relief – has been assumed by previous investigations (e.g. Leeson et al., 2015; Ignéczi et al., 2016) (Section 4.2.1). The uncertainties associated with this assumption, which could limit its applicability, are quantified in Section 4.4.1. Finally, I discuss the potential effects the changing future distribution of surface lakes could exert on the mass balance and dynamics of the GrIS (Section 4.4.4).

4.4.1. Changing surface relief of the GrIS between 1980 and 2300, and its effects on surface lake distribution

The ice sheet-wide overall magnitude and spatial pattern of changing surface relief during 1980-2300 (Section 4.3.2.2) correlate well with changing ice thickness and basal slip ratio (Section 4.3.2.1), as these two factors exert the key control on the efficiency of the bed-to-surface transfer (e.g. Gudmundsson, 2003) (Chapter 2). The ice sheet-wide overall increase of surface relief is small during the 21st century (Section 4.3.2.2) due to the small ice sheet-wide relative decrease in ice thickness and small relative increase in basal slip ratio (Section 4.3.2.1). However, between 2100 and 2300, the rates of these changes increase significantly (Section 4.3.2.1 and 4.3.2.2). The aforementioned changes are not uniform across the GrIS, most notably the increase in surface relief is larger than average – even far from the ice sheet margin – in the SW-W

and NE (Section 4.3.2.2), due to the large decrease in ice thickness and large increase in basal slip ratio in these regions (Section 4.3.2.1) which allows a more effective bed to surface transfer (Gudmundsson, 2003; Ng et al., 2018). On the other hand, significant changes are not common in the S and E sections of the GrIS. Furthermore, in some parts of the S and E, and also very close to the ice sheet margin elsewhere, the surface relief slightly decreases during 1980-2300 (Section 4.3.2.2). This is mostly due to the decreasing basal slip ratio and a slight increase in ice thickness, in these regions (Section 4.3.2.1).

My results demonstrate that the surface relief of the GrIS, which controls the distribution of surface depressions and lakes (Chapter 3), is quite robust and changes negligibly during the 21st century, except in the cases discussed in Section 4.3.2.2. However, the surface relief is predicted to change significantly between 2100-2300 (Section 4.3.2.2). Consequently, neglecting the changing surface relief only causes a 0.8-1.7% underestimation of the total surface lake volume by 2100, but a 13.3% underestimation by 2300. Underestimation of the ice sheet area normalised total volume of surface lakes – i.e. which shows the ice sheet-wide average volume of surface lakes – is larger, 0.8-1.8% and 14.4% respectively (Section 4.3.2.5). Hence, the effects of changing surface relief could be neglected for the majority of the ice sheet, except near the ice sheet margin and in areas where the SIA is inaccurate (e.g. major outlet glaciers) (Vizcaino et al., 2014), when investigating the changing distribution of surface lakes during the 21st century (e.g. Leeson et al., 2015; Ignéczi et al., 2016). Furthermore, my calculations assume that the surface relief has reached steady-state (Ng et al., 2018), whereas in fact the surface relief is a time-lagged response to changes in the perturbation (e.g. bed topography) and background variables (e.g. ice thickness) (Gudmundsson 2003). The relaxation timescale is typically <100 years along ice sheet flowlines, except near the ice divide (Ng et al., 2018). However, the relaxation timescale for longer non-dimensional wavelengths (λ/H), which have higher amplitudes and thus a larger effect on the surface relief, is just a couple of decades (Ng et al., 2018). Thus, the actual surface relief response to changes in ice thickness and basal slip ratio is expected to lag my surface relief predictions by around a couple of decades. This fact also supports my conclusion that the effects of changing surface relief could be neglected during the 21st century. However, the effects of the changing surface relief should be taken into consideration when projecting the distribution of surface lakes beyond 2100.

4.4.2. Changing surface lake distribution and rapid drainage between 1980-2100 assuming constant surface relief

First, I discuss my surface lake projections for the 21st century assuming fixed ice sheet surface topography (Section 4.3.1), which is valid over this timescale (Section 4.4.1). These projections utilize the surface depression survey, which was derived directly from the GIMP-DEM (Section 3.2.2.1), and are therefore more precise in estimating the volume of surface depressions than the projections which infer the volume of surface depressions indirectly from the surface relief (Section 4.2.2.2). Hence, I consider these projections as the primary source of information about the changing distribution of surface lakes during the 21st century.

Due to regional variations (Section 4.3.1.3), a notable shift in the relative distribution of surface lakes will occur on the GrIS during the 21st century, which has not been indicated by previous projections (Leeson et al., 2015). The W, NW and especially the NE will become the focus of surface lake formation on the GrIS by the end of the 21st century, while the importance of the SW catchment will decline. This could be further enhanced by large-scale climatic effects, such as the recent poleward shift of low albedo and high runoff on the GrIS (Tedesco et al., 2016). However, I have also found that the total volume of surface lakes – and its relative increase – in the different catchments of the GrIS is insensitive to the size and relative increase of the ablation area in the catchments (Fig. 4.7). Hence, I propose that the aforementioned shift in surface lake presence is mainly controlled by the regional distribution of surface depressions (Section 4.3.1.1). Furthermore, correlations corresponding to future predictions – especially in the case of the high climate change scenario, i.e. RCP 8.5 – are weaker than the contemporary correlation (Fig. 4.7). This could be explained by the future expansion of the ELA – and surface lake formation – towards higher elevations. In contrast to low elevations, surface depressions are generally scarce in these regions (Fig. 4.4), except where the bed-to-surface transfer is effective through thick ice e.g. W, NW, NE (Fig. 4.4, Chapter 3). Hence, the availability of surface depressions, controlled by the bed-to-surface transfer (Chapter 3), is expected to become an increasingly important control on the regional distribution of surface lakes in the future.

The contemporary (i.e. 1980-2009) ice sheet-wide mean probability of rapid lake drainage is estimated to be 0.2 (Section 4.3.1.3). This is comparable to the observed relative frequency of rapid lake drainage events across the ice sheet: 13% (Selmes et al., 2011), and in the W and SW: 1-28% (Liang et al., 2012; Morriss et al., 2013; Fitzpatrick

et al., 2014) – equivalent to an overall rapid lake drainage probability of 0.13 and 0.1-0.28 respectively. However, a recent study has shown that previous investigations have underestimated the actual relative percentage of rapid lake drainage events, due to the nebulous definition of rapid lake drainage, the limited availability of satellite imagery, and cloud coverage (Cooley and Christoffersen, 2017). After correcting for the underestimation caused by the aforementioned observation bias, the relative frequency of rapidly draining lakes was estimated to be around 36-45% in West Greenland (Cooley and Christoffersen, 2017), which differs significantly from my estimations (Section 4.3.1.3). This disparity indicates that either the potential for hydrofracture – which depends on the dimensions and the volume of the surface depressions, the thickness and the elastic properties of the ice – or the potential for surface crack presence limits the rapid drainage of surface lakes to a lesser degree than expected. I suggest that the latter is the key factor, as tensile shocks triggered by initial rapid lake drainage events could open up transient surface cracks over large distances (Christoffersen et al., 2018; Hoffman et al., 2018).

I attribute the decreasing overall probability of rapid lake drainage to the expansion of surface lakes towards higher elevations – due to the rising ELA – where the potential for hydrofracture and surface crack presence is lower (Fig 4.5, Section 4.3.1.1). Hence, as more surface lakes form at high elevations the overall rapid drainage probability decreases. This is in line with Poinar et al. (2015), who suggested that rapid lake drainage is hindered above 1600 m in West Greenland due to the limited presence of surface cracks, caused by lower extensive principal strain rates. However, Cooley and Christoffersen (2017) found that the relative frequency of rapid lake drainage does not decrease with elevation – even above 1600 m – in W Greenland, probably due to the effects of tensile shocks (Christoffersen et al., 2018; Hoffman et al., 2018) which are not incorporated into my calculations. Therefore, my results should be considered a conservative estimation of the future frequency of rapid lake drainage on the GrIS. Furthermore, I propose that further investigations about the rapid drainage of high elevation lakes are necessary, as surface lakes are expected to extend inland in the future (e.g. Leeson et al., 2015) and currently only a small number of lakes form at high elevations (Cooley and Christoffersen, 2017) which might limit our current ability to ascertain high elevation lake processes.

In conclusion, I suggest that the spatial distribution of surface depressions – and the proximity of both the contemporary and the projected ELA to up-glacier areas with a high number of surface depressions – is the primary factor controlling the changing

future distribution of surface lakes on the GrIS. As the spatial distribution of surface depressions is highly variable across the GrIS (Section 4.3.1.1), I caution against extrapolating the ice sheet-wide future evolution of surface lakes from a small study area (e.g. Leeson et al., 2015). Although the overall probability of rapid lake drainage is projected to decrease, a strict limit on the absolute number of rapid lake drainage events is not expected for the 21st century even when employing conservative estimations, as the number of surface lakes increases (Section 4.3.1.3, Table 4.5). Hence, I suggest that rapid lake drainages will remain widespread during the 21st century.

4.4.3. Changing surface lake distribution and rapid drainage between 1980-2300, accounting for the effects of the changing surface relief

The contemporary and projected SMB – and thus the ELA – of the MAR v.3.5.2 outputs of Fettweis et al. (2013, 2017) and the SICOPOLIS ice sheet model outputs of Vizcaino et al. (2014) differ considerably. The ELA derived from the outputs of Vizcaino et al. (2014) is higher than the MAR derived ELA in most cases, especially in the NE and W-NW (Figs. 4.4 and 4.15A). This is not surprising, given that the ice sheet surface topography is fixed in the MAR simulations (Fettweis et al., 2013, 2017), whereas SICOPOLIS incorporates the SMB-elevation feedback, which causes negative SMB anomalies over most of the ice sheet (Vizcaino et al., 2014). Furthermore, the largest decrease in ice thickness – and consequently the strongest elevation-melt feedback – is projected to occur in the NE and W-NW (Fig. 4.9), which explains the aforementioned larger than average difference between the SICOPOLIS and MAR derived ELAs in this region. Besides the differences in the SMB outputs, the spatial dimensions and coverage of the modelled GrIS do not match precisely with the observed contemporary ice sheet. Generally, the modelled ice sheet extends beyond the observed ice sheet margin, though in the NW the situation is the opposite (Vizcaino et al., 2014). Furthermore, ice sheet-wide total depression volumes calculated from surface relief datasets generally underestimate the ice sheet-wide total surface depression volume derived from the GIMP-DEM (Section 4.3.2.3). Hence, comparing the projected surface lake volumes derived directly from the GIMP-DEM and MAR ELA (Section 4.2.1), with the projected surface lake volumes inferred from the predicted surface relief datasets (Section 4.2.2) and the SICOPOLIS derived ELA (Vizcaino et al., 2014) for the overlapping time periods is difficult. However, relative changes in the surface lake

volume – i.e. 2100-2300 compared to the 21st century – can be evaluated from SICOPOLIS outputs, using the approach described in Section 4.2.2.2.

Between 2100-2300 the ice sheet-wide overall rate of surface lake volume increase slows down – compared to the 21st century – according to the SICOPOLIS derived outputs (Section 4.3.2.5). Although the actual magnitudes might differ from my projections (Table 4.10) – due to the factors discussed above – this scenario is likely for the following reasons. Firstly, surface depressions are generally scarce at high elevations in the interior of the GrIS, especially in the N and SW, according to both the GIMP-DEM and SICOPOLIS derived surface depression datasets (Figs. 4.4 and 4.13A). Thus a given increase in the ELA has a smaller effect on the total volume of surface lakes after 2100 as the ELA already attains a high elevation by 2100. Secondly, both the MAR and the SICOPOLIS SMB projections indicate that the ELA does not expand significantly into the ice sheet interior in S, SE and E catchments during the 21st century or between 2100-2300 (Vizcaino et al., 2014; Fettweis et al., 2013). Hence, surface depressions in this region – which have a significant total volume in the SE and E – are unlikely to host many lakes even after 2100 (Section 4.3.1.1 and Section 4.3.1.3), limiting the increase of the ice sheet-wide total surface lake volume. Finally, the shrinking size of the ice sheet, which is significant between 2100 and 2300, also limits the overall increase in surface lake volume (Sections 4.3.2.4 and 4.3.2.5).

On the other hand, GIMP-DEM derived projections suggest that only 36.7% of the full potential surface lake volume is attained in the NE by 2100 (Table 4.3). The situation is similar in the W and NW, though here a higher percentage (~51%) of the full potential surface lake volume is attained by 2100 (Table 4.3). Although these projections – using MAR outputs – do not account for the intensive positive feedback between melt and elevation in these regions (Vizcaino et al. 2014) which might cause a larger expansion of surface lakes than projected (Section 4.3.1), there is a large potential for surface lake expansion in these regions after 2100. Furthermore, around 13.3% of the ice sheet-wide total surface lake volume increase between 1980 and 2300 – as opposed to 0.8-1.7% between 1980 and 2100 – is caused by the increasing surface relief and consequently the increasing surface depression volume (Section 4.4.1). The largest relative increase in surface depression volumes – due to the changing surface relief – is observed in the W, NW and NE between 2100-2300, which further enhances the potential for surface lake expansion in this region beyond 2100 (Fig. 4.13). This is mostly due to the larger than average thinning of the ice sheet in this region (Fig. 4.9), partly due to the intensive melt-elevation feedback (Vizcaino et al., 2014). In

conclusion, I suggest that most of the surface lake volume increase after 2100 occurs in the NE and to a lesser degree in the W-NW due to the high number of depressions in the interior of the GrIS in these catchments. This is caused by the efficient contemporary bed-to-surface transfer in these regions – enabling the formation of a high number of depressions at high elevations – which is also projected to increase in the future.

Changing surface relief and ice thickness also affect the spatial extent of the region where hydrofracture is likely ('likely' hydrofracture is defined in Section 4.2.1.2). Greater surface relief makes surface depressions smaller and deeper (Fig. 4.2), slightly decreasing their mean volume (Fig. 4.14). At the same time, the horizontal length of water-filled cracks – corresponding to surface depressions – also decreases due to the smaller depression area. Furthermore, the thinning ice sheet – which is the predominant driver of the surface relief increase (Section 4.4.1) – causes the depth of water-filled cracks to decrease. Hence, similar to surface depressions, the volume of potential water-filled cracks decreases, but at a higher rate than the mean volume of surface depressions. Therefore, the region where hydrofracture is likely extends during 1980-2300, especially after 2100, though this extension is small (Fig. 4.16). Despite this finding, I propose that the overall probability of rapid lake drainage will continue to fall after 2100 due to the continuing inland expansion of surface lakes, caused by the rising ELA (Fig. 4.15). This leads to increasing average ice thickness directly beneath surface lakes, which limits the overall potential for hydrofracture (Fig. 4.16). Furthermore, the inland expansion of surface lakes and the increasing size of the ablation area also cause a decrease in the relative spatial coverage of high principal strain rates (i.e. above $+0.005\ yr^{-1}$) below the ELA (Table 4.11), as principal strain rates are generally low at high elevations (Poinar et al., 2015). Thus, the overall potential for surface crack presence also decreases, even after 2100.

The aforementioned processes are similar to those that were discussed in relation to the changing probability of rapid lake drainage during the 21st century (Section 4.4.2). However, the inland expansion of surface lakes slows after 2100, and thus the rate of increase in the effects that reduce the overall potential for hydrofracture and surface crack presence will also become smaller (Section 4.3.2.5, Table 4.11). Hence, the rate of decrease in the overall probability of rapid lake drainage is likely to slow as well after 2100. Future increases in the spatial coverage of high principal strain rates – and thus surface cracks (e.g. Colgan et al., 2011) – are, however, likely to be underestimated by the SICOPOLIS ice sheet model (Vizcaino et al., 2014), as the SIA neglects several factors which enhance extensional strain and crevassing, e.g.

longitudinal and transverse stress fields, hydrologically induced ice flow accelerations (Colgan et al., 2011; Stevens et al., 2015). This, in addition to the potential effects of tensile shocks (already discussed in Section 4.4.2), suggests that my estimations are conservative.

4.4.4. Consequences of the changing surface lake distribution on ice sheet mass balance and dynamics

The predicted expansion of surface lakes during and beyond the 21st century is likely to impact on the dynamics and mass balance of the GrIS. The projected future expansion of low albedo surface lakes towards high elevations (Section 4.3) will reduce the albedo and enhance surface melting over larger regions of the GrIS (Greuell et al., 2002; Lüthje et al., 2006; Tedesco et al., 2012). This is especially interesting when considering a potential saddle collapse on the GrIS, i.e. a runaway melt-elevation feedback occurring on a lowering saddle between two ice domes (Gregoire et al., 2012). According to ice sheet model projections (Vizcaino et al., 2014), two saddles will start to develop on the GrIS by 2300 due to intensive ice thinning near the ice sheet divide between the NW, NE and the SW, SE catchments (Fig. 4.9). The northerly saddle is especially important as the focus of surface lake presence – and thus lake induced albedo-melt feedback – is projected to shift towards this region (Figs. 4.6 and 4.15), due to the rising ELA and the high number of large surface depressions at high elevations. Although the contemporary bed-to-surface transfer is already efficient in this region – enabling the formation of high elevation depressions (Chapter 3) – the transfer is projected to enhance after 2100 due to ice thinning (Figs. 4.9 and 4.13). Thus even more surface depressions and lakes are expected to form in this region by 2300. In conclusion, the future expansion of low-albedo surface lakes – and the more prevalent presence of surface meltwater – is expected to enhance the melt-elevation feedback which could also set up a positive feedback with bed-to-surface transfer. This process is potentially another, so far overlooked, aspect of saddle collapse.

Besides the albedo effect, surface lakes could also influence ice flow (Section 1.1). The net influence of surface lakes on ice flow depends on two key considerations: the ability of surface lakes to drain to the bed through thick ice; and the seasonal/interannual evolution of the subglacial drainage system controlled by the net effects of the basal water pressure variations (e.g. Sole et al., 2013; Tedstone et al., 2015; Hoffman et al., 2017; Nienow et al., 2017) (Section 1.1). According to my

findings rapid lake drainage will remain widespread on the GrIS (Sections 4.4.2 and 4.4.3), especially at lower elevations. Although rapid lake drainage at high elevations could be somewhat hindered due to the lower potential for surface crack formation, there are factors which suggest that high elevation lakes could also drain rapidly to the ice sheet bed (Sections 4.4.2 and 4.4.3). Firstly, the theoretical expectation of Krawczynski et al. (2009) that hydrofracture and rapid lake drainage through thick ice is possible in most cases, has been confirmed by my calculations (Sections 4.2.1.2 and 4.2.2.2), which show that hydrofracture is likely or possible over most of the GrIS (Figs. 4.4 and 4.16). Secondly, despite the proposed rarity of surface cracks at high elevations (Fig. 4.4) – inferred from conservative estimations based on principal strain rates (Section 4.2.1.2) – several factors (e.g. tensile shocks) could enhance surface crack formation (discussed in Sections 4.4.2 and 4.4.3). Hence, in agreement with satellite derived observations (Cooley and Christoffersen, 2017), I suggest that rapid lake drainage events – and thus the influence of surface lakes on ice flow – could be common at high elevations, where a significant expansion of surface lakes is expected by 2300.

Whether the rapid drainage of surface lakes leads to ice flow acceleration or self-regulation is equivocal (Section 1.1). At high elevations, hydraulic gradients are lower – due to lower surface slopes – and ice is thicker, thus creep closure of subglacial channels and cavities is also likely to be faster than at low elevations (Chandler et al., 2013; Tedstone et al., 2015). Furthermore, I propose that the magnitude and spatiotemporal variance of surface-to-bed meltwater pulses are larger at high elevations. This is based on several considerations which apply to high elevations: (i) depressions and lakes are large and clustered (Sections 4.3.1.1 and 4.3.2.4) due to the strong spatial variance in the effectiveness of bed-to-surface transfer through thick ice (Chapter 3), (ii) tensile shocks are more important in triggering rapid lake drainage events (Christoffersen et al., 2018; Hoffman et al., 2018), (iii) and surface-to-bed meltwater transport is controlled predominantly by the rapid drainage of surface lakes as opposed to drainage through pre-existing crevasses (e.g. Clason et al., 2015). Hence, I suggest that the formation of effective subglacial drainage systems is hindered, and the spatiotemporally varying surface-to-bed meltwater injections overwhelm the subglacial system more easily at high elevations (e.g. Bartholomew et al., 2012; van de Wal et al., 2015). Furthermore, rapid lake drainage events might also cause significant cryohydrological warming at high elevations, due to the presence of frozen bed and/or cold ice in the ice column (Phillips et al., 2010; Doyle et al., 2014; Harrington et al,

2015; MacGregor et al., 2016). In conclusion, I propose that the projected inland expansion of surface lakes could cause net ice flow acceleration at high elevations. This effect is likely the strongest in the W, NW and NE, as the largest inland expansion of surface lakes is projected for these catchments (Figs. 4.6 and 4.15). The proposed net acceleration could also complement the aforementioned positive feedbacks between elevation, melt, albedo, ice thickness, bed-to-surface transfer, and depression/lake formation in these regions, and might be an additional factor contributing to saddle collapse.

At lower elevations, e.g. below 1100 m in SW Greenland (Tedstone et al., 2015), conditions are currently favourable for the formation of efficient subglacial drainage systems. Accordingly, increased surface melting currently causes net ice flow deceleration (i.e. self-regulation) in these regions (van de Wal et al., 2008, 2015; Sole et al., 2013; Tedstone et al., 2015) (Section 1.1). My projections focus on the inland expansion of surface lakes, and thus are not suitable to predict the intricate changes in surface lake distribution and volume at low elevations. However, in a warming climate, with greater melt volumes and longer melt seasons, efficient subglacial drainage and ice flow self-regulation is likely to remain prevalent at low elevations across the GrIS (e.g. Tedstone et al., 2015). Nevertheless, the GrIS might react differently to a warming climate – and thus increased surface melting – at marine terminating sections of the ice sheet margin (Section 1.1). Greater surface-to-bed meltwater injections and subglacial meltwater transport – originating locally and/or from higher elevations due to the inland expansion of surface lakes – might lead to larger and more persistent meltwater plumes emerging from the grounding lines of tidewater glaciers. This could then cause more intensive calving and terminus retreat, especially if coastal water is warming as well (e.g. Cowton et al., 2015, 2018). In conclusion, the response of the GrIS to increased surface lake presence and surface-to-bed meltwater transport likely differs between regions and elevations – though more information is needed to precisely ascertain these differences – thus the net effect on GrIS mass balance is uncertain (e.g. Shannon et al., 2013).

4.5. Summary

The total volume and regional distribution of surface depressions can be inferred from the predicted surface relief of the GrIS calculated using SICOPOLIS outputs, though the total volume of surface depressions is underestimated by ~24%. Hence,

projections calculated from the predicted surface relief and the SICOPOLIS derived ELA can be used to infer the changing future distribution of surface lakes. My calculations demonstrate that surface relief increases during the 21st century on the GrIS, but these changes are small and have a negligible effect on the total volume of surface lakes. Neglecting the changing surface relief causes only a 0.8-1.7% underestimation of the total volume of surface lakes during the 21st century (0.8-1.8% when surface lake volumes are normalised by the ice sheet area). Hence, projections based on the GIMP-DEM and MAR derived ELA are valid for the 21st century. However, the surface relief increases significantly between 2100 and 2300, exerting a stronger effect on surface lake volumes. Neglecting the changing surface relief causes a 13.3% underestimation of the total volume of surface lakes during 2100-2300 (14.4% when surface lake volumes are normalised by ice sheet area). Hence, surface lake projections beyond 2100 should account for the changing surface relief, and consequently the changing volume of surface depressions.

Although the SICOPOLIS derived surface lake projections are more comprehensive, I propose that the projections based on the GIMP-DEM and MAR derived ELA should be considered as the primary source of information about the changing future distribution of surface lakes during the 21st century. This is because these projections are likely to be more accurate than the SICPOLIS derived projections – e.g. due to the direct calculation of surface depression volume – and the effect of changing surface relief on surface lake volumes is small during the 21st century. The GIMP-DEM and MAR-ELA derived projections indicate that the ice sheet-wide total volume of surface lakes – i.e. the maximum volume of meltwater that could be contained in surface lakes during a given melt season – increases by around 172-270% during the 21st century. Due to regional variations in surface lake expansion, the focus of surface lake presence is predicted to shift from the SW to the W, NW and NE, while surface lakes remain rare in the S, SE and E during the 21st century. According to the SICOPOLIS derived projections, these trends continue between 2100 and 2300, though the rate of overall surface lake volume increase slows after 2100. The aforementioned shift of surface lakes from the SW to the W, NW and NE is also facilitated by the larger than average increase of surface relief – and consequently surface depression volume – in these regions after 2100. Although the position and the inland expansion of the ELA are important, the size and relative increase of the ablation area are not the main factors that control the future regional distribution of surface lakes. Instead the key factors are

the spatial distribution of surface depressions, and shifts of the ELA in regions where surface depressions are abundant.

Realistic estimations of the contemporary ice sheet-wide probability of rapid lake drainage were calculated from the dimensions of surface depressions, the thickness of the ice beneath the depressions, the width profiles of potential water-filled crevasses – based on elastic fracture mechanics – and the principal strain rate of the ice flow. As surface lakes expand into the interior of the GrIS, the ice sheet wide mean probability of rapid lake drainage is expected to decrease, though at a slower rate after 2100, due to the limited presence of surface cracks at high elevations. Despite reduction in the chances of individual lakes draining, the number of rapid lake drainage events increases during this period – especially between 1980 and 2100 – due to the greater number of surface lakes that are expected to form. However, the exact processes governing the rapid drainage of surface lakes – especially at high elevations – are still a subject of intensive research (e.g. Cooley and Christoffersen, 2017; Christoffersen et al., 2018; Hoffman et al., 2018). Hence, these results only represent an initial conservative estimation of future changes of rapid lake drainage probability and frequency across the GrIS, based on the most fundamental processes known to affect the rapid drainage of surface lakes.

Surface lakes enhance surface melting due to their lower albedo. This feedback is expected to be the strongest in the W, NW and NE, where projections indicate the largest surface lake expansion. Close to the ice sheet margin across the GrIS – especially at land terminating sections – the rapid drainage of surface lakes is likely to cause a net deceleration of the ice flow in the future, similar to the current situation in SW Greenland. However, the rapid drainage of lakes could also cause a net acceleration of the ice flow in regions where surface lakes expand far into the interior the ice sheet, which is expected in the W, NW and NE. These regions may also be susceptible for a future saddle collapse. Nevertheless, further work is needed to fully understand the net effects of rapid lake drainage on ice dynamics – especially at high elevations and tidewater glaciers – and to test my suggestions about these effects.

CHAPTER 5: CONCLUSIONS

5.1. Summary of the main findings

Below, I summarise my results into 7 principal findings. These relate to the application of the bed-to-surface transfer theory (Conclusions 1-2), the spatial-structure of surface drainage (Conclusion 3), and the changing future distribution of surface lakes (Conclusions 4-7).

1.) The surface relief of the GrIS is predominantly controlled by the bed-to-surface transfer of bed topographical variations, and thus can be predicted using existing theory.

The observed and predicted surface topographical undulations calculated along 5138 non-uniform flowlines on the GrIS represent a significant advancement in the empirical testing of the bed-to-surface transfer theory, as previous tests were spatially limited, i.e. 2 non-uniform (Ng et al., 2018) and 17 closely uniform (De Rydt et al., 2013) glacier flowlines. The spatial pattern of the observed surface relief is reproduced qualitatively by my calculations, which indicate the general success of the theory. Furthermore, sensitivity tests show that bed topography – along with modulating factors: ice thickness, basal slip ratio and surface slope – is the predominant control on the surface relief, while basal slipperiness perturbations only exert a secondary influence (accounting for less than <25% of the surface relief).

2.) Discrepancies between the observed and predicted surface relief conform to known limitations of the transfer theory and the input datasets.

Although the observed and predicted surface relief exhibit a reasonable linear relationship, the considerable mean absolute error (14.9 m) and the spatial pattern of the relief anomaly – i.e. spectral-mean difference between the observed and predicted CWT of surface undulation amplitudes – suggest several sources of uncertainty. These include unknown basal slipperiness perturbations, uncertainties of the bed topography and basal slip ratio datasets, surface processes on the ice sheet, the assumption of a linearly viscous fully temperate ice, and 3D effects on the transfer of basal variability. The spatial pattern of the relief anomaly was consistent with the expected effects caused by these factors. Despite the discrepancies, the surface relief can be predicted with acceptable accuracy using the non-stationary extension of Gudmunsson's (2003)

transfer theory (Ng et al., 2018). Furthermore, the spatial pattern of the relief anomaly can also be used to identify poorly resolved bed topography, e.g. undiscovered subglacial valleys in the SE where positive amplitude anomalies align with high strain rates and disconnected subglacial depressions (Section 2.4.2.4).

3.) The large-scale spatial structure of surface drainage is preconditioned by the bed-to-surface transfer of bed topographical variations.

The observed surface relief calculated from mesoscale surface topographical undulations – themselves controlled by bed topography – influences the large-scale spatial structure of the surface drainage, by delineating the maximum potential spatial distribution of surface drainage features. Other factors – such as surface runoff – modulate this control mainly through determining the seasonal evolution of surface drainage, i.e. to what degree the maximum coverage of surface drainage elements is attained at a certain location and at a given time. Although all key elements of the surface drainage system – i.e. surface lakes and streams, moulins – have been shown to correlate with surface relief, the strongest control was observed in the case of surface lakes. As surface relief is predominantly controlled by the bed-to-surface transfer of basal topographical perturbations, the large-scale spatial structure of surface drainage is also influenced by bed topography and the factors modulating bed-to-surface transfer (i.e. ice thickness, basal slip ratio, surface slope). As it is possible to predict the surface relief using the non-stationary extension of Gudmunsson's (2003) transfer theory, the spatial structure of surface drainage can also be inferred using this method.

4.) Changing surface relief only exerts a significant effect on the predicted volume of surface lakes after 2100.

Although the surface relief of the GrIS is projected to change during the 21st century – due to evolving ice thickness, basal slip ratio and surface slope – these changes are generally small. Accordingly, neglecting changes in the surface relief only causes 0.8-1.7% underestimation of the ice sheet-wide total surface lake volume during the 21st century (0.8-1.8% when surface lake volumes are normalised by the ice sheet area). Hence, surface lake projections for the 21st century could neglect changing surface topography. However, surface relief changes significantly between 2100 and 2300; neglecting the changing surface relief causes a 13.3% underestimation of the ice sheet-wide total surface lake volume by 2300 (14.4% when surface lake volumes are

normalised by the ice sheet area). Thus, surface lake projections beyond 2100 should take the changing ice surface topography into consideration, especially in regions where the increase in surface relief – and thus surface depression volume – is the largest (e.g. W, NW and NE).

5.) Surface lakes are projected to expand inland significantly by the end of the 23rd century, while the focus of lake presence shifts to the W, NW and NE.

The maximum volume of meltwater that could be contained in surface lakes – during a given melt season – is projected to increase with 172-270% by 2100 on the GrIS (compared to 1980-2010), according to the GIMP-DEM and MAR-ELA derived projections. The increase of surface lake volume is not uniform across the GrIS; the focus of surface lake presence will shift to the W, NW and NE – from the SW – by the end of the 21st century due to different regional trends. These trends continue between 2100 and 2300, though the rate of increase in surface lake volume slows after 2100 due to the more restricted presence of surface depressions at high elevations. Furthermore, the changing surface relief – which is the largest in the W, NW and NE – is projected to reinforce the regional shift in surface lake distribution from the SW to the W, NW and NE, especially after 2100.

6.) The changing future distribution of surface lakes is predominantly controlled by the distribution of surface depressions, and the efficiency of bed-to-surface transfer.

The size (and relative increase) of the ablation area per catchment correlates weakly with the total volume (and relative increase) of surface lakes, according to the GIMP-DEM and MAR-ELA derived projections. Furthermore, these correlations are lower as surface lakes expand further inland in the future (Section 4.3.1.3). Hence, regional variations in the rate of surface lake expansion are mostly attributed to regional differences in the distribution of surface depressions, controlled by the bed-to-surface transfer (e.g. high bed roughness and basal slip ratio cause the abundance of surface depressions at high elevations on the NEGIS, which then leads to a large inland expansion of surface lakes). This is expected to become increasingly important in the future when the ELA expands far into the interior of the GrIS, where surface depression are scarcer and thus pose an increasingly important limiting factor for surface lake formation.

7.) The inland expansion of surface lakes is expected to enhance surface melting and accelerate ice flow at high elevations.

The inland expansion of low albedo surface lakes is expected to contribute to the melt-elevation feedback on the GrIS. This feedback is projected to be the strongest in the W, NW and NE (e.g. Vizcaino et al., 2014), where the inland expansion of surface lakes is also the largest, potentially contributing to a future saddle collapse. The influence of surface lakes on ice flow dynamics, especially at high elevations, is dependent on the ability of lakes to drain rapidly to the ice sheet bed. The overall probability of rapid lake drainage is projected to decrease between by 2300 due to the inland expansion of lakes and the lower potential for rapid lake drainage at high elevations. However, the overall frequency of rapid lake drainage is likely to remain stable due to the increasing number of lakes. Furthermore, my estimations ignore several processes – especially at high elevations – that could facilitate rapid lake drainage, e.g. tensile shocks (Christoffersen et al., 2018; Hoffman et al., 2018). Hence, I propose that rapid lake drainage, and thus influence on ice flow, will remain widespread on the GrIS and will not be strongly limited to lower elevations. Although the effect of rapid lake drainage on ice flow dynamics is equivocal – either ice flow acceleration or self-regulation – I propose that ice flow acceleration in response to the inland expansion of surface lakes is likely at high elevations, as the formation of efficient subglacial drainage is hindered in those regions. On the other hand, ice flow self-regulation is likely to occur at low elevations in response to climate warming, though these regions were not in the focus of my investigation.

5.2. Main limitations of the study

To reach the conclusions that are summarised above (Section 5.1), several sources of uncertainty were considered throughout the thesis. Here, I summarise these sources which fall into 4 categories.

1.) Inherent limitations of the bed-to-surface transfer theory

The primary source of uncertainty in my thesis is related to the inherent limitations of Gudmundsson's (2003) bed-to-surface transfer theory and its non-stationary extension by Ng et al. (2018), as this theory was used to predict the surface relief of the GrIS in all major chapters of the thesis (i.e. Chapter 2, 3 and 4). The bed-to-

surface transfer equations were formulated using the full Stokes equations and perturbation theory by assuming steady, plane-parallel ice flow and constant ice viscosity (Gudmundsson, 2003). The non-stationary extension of the original theory – circumventing the plane-parallel ice flow assumption – was derived by considering Gudmundsson's (2003) transfer equations as impulse response functions and applying an approximation based on non-stationary convolution (Ng et al., 2018) (Section 1.2.3). The first and most obvious limitation associated with my approach is the exclusion of surface processes which influence the surface relief of the ice sheet (e.g. wind, spatial variation in surface mass balance and snow/firn compaction rates), as the non-stationary extension of Gudmundsson's (2003) bed-to-surface transfer theory (Ng et al., 2018) was used exclusively in my thesis to predict the surface relief of the GrIS. However, considering the results of previous studies (e.g. Black and Budd, 1964; Gow and Rowland, 1965; Whillans, 1975; Medley et al., 2015) and the success of my prediction experiments (Chapter 2), I concluded that surface processes only exert a secondary influence on the surface relief of the GrIS (Section 2.4.2.1).

Although the assumption of plane parallel ice flow has been circumvented, the assumption of constant ice viscosity – i.e. a linear stress-strain relationship – and steady ice flow still applies to the non-stationary extension of the bed-to-surface transfer theory (Ng et al., 2018). Numerical experiments by Raymond and Gudmundsson (2005) demonstrated that non-linear ice rheology exerts a quantitative influence on the bed-to-surface transfer, though the qualitative aspects of the transfer functions remain largely the same. Accordingly, the surface relief of the contemporary GrIS – especially its qualitative spatial pattern – was successfully predicted by my calculations (Chapter 2). Furthermore, the spatial pattern of the difference between the observed and predicted mean surface relief was found to be consistent with the expected effects due to the assumption of constant ice viscosity (Sections 2.3.2 and 2.4.2.3). Besides constant ice viscosity, my calculations also assume that the bed-to-surface transfer has reached a steady-state (Ng et al., 2018). Thus, the actual surface relief of the GrIS lags behind my predictions by about a couple of decades (Gudmundsson, 2003; Ng et al., 2018) (Section 4.4.1). However, the relative change in the factors that determine the strength of the bed-to-surface transfer is generally small during this period of time, especially further from the ice sheet margin (e.g. Section 4.2.1). Hence, I propose that the assumption of steady ice flow does not substantially hinder the accuracy of my calculations, this is demonstrated by the success of my contemporary experiments in Chapter 2.

Another key limitation of my study stems from the fact that the bed-to-surface transfer was calculated along ice flowlines. This approach was dictated by the non-stationary extension of Gudmundsson's (2003) bed-to-surface transfer theory which has only been derived for 2D ice flow, i.e. along ice flowlines (Ng et al., 2018). Previous studies demonstrated that 2D approximations tend to overestimate the strength of the actual 3D bed-to-surface transfer, especially where lateral variations in the basal properties are large (Sergienko, 2012; De Rydt et al., 2013). Despite this well established fact, the surface relief is underestimated over the majority of the ice sheet (92.5%), while overestimation is restricted to smaller areas which are generally close to the ice sheet margin and major subglacial valleys (Section 2.3.2). Hence, I conclude that 3D effects on the bed-to-surface transfer are only significant where lateral variations in the subglacial topography are exceptionally large.

2.) Uncertainties in observed contemporary datasets

Similar to the inherent limitations of the bed-to-surface transfer theory which are discussed above, uncertainties of the contemporary datasets – i.e. datasets that are predominantly based on observations of the present-day GrIS – that were used in my thesis (bed and surface DEMs, basal slip ratios, surface lakes, rivers and moulins derived from satellite imagery) also affect the outcomes of every major chapter (Chapter 2, 3 and 4).

The most significant limitation is caused by the uncertainty of the IceBridge BedMachine Greenland, Version 3 dataset (Morlighem et al., 2017a, 2017b; 150 m grid resolution). The nominal resolution of this bed DEM is suitable to predict the response of GrIS surface topography to basal topographical perturbations, as the bed-to-surface transfer is very weak at wavelengths similar to the spatial resolution of the bed DEM, unless the ice is very thin which only occurs close to the ice sheet margin (Gudmundsson, 2003). However, the actual resolution of the data is spatially inconsistent, and mainly depends on the density of the flight lines along which the ice thickness measurements were made (Morlighem et al., 2017a, 2017b). Hence, my calculations are less precise in regions where flight lines are scarce, and thus basal topographical features are poorly known, e.g. in the ice sheet interior and along the SE Greenland coastline (Morlighem et al., 2017a, 2017b). Accordingly, the surface relief of the GrIS is underestimated in these regions by my calculations (Section 2.3.2). Surface relief projections in Chapter 4 are affected in the same way, as the same bed DEM was

used for these calculations. Conversely, the resolution and accuracy of the GIMP-DEM (Howat et al., 2014; 2017; 30 m grid resolution) – the surface DEM which was used to calculate the observed surface relief of the GrIS – are relatively consistent across the GrIS, and suitable for calculating the surface relief of the ice sheet. Hence, I do not associate significant limitations to its application.

Limitations of the basal slip ratio dataset created by MacGregor et al. (2016) cause a degree of uncertainty in Chapter 2. Basal slip ratios are generally underestimated by this dataset due to the assumption of fully temperate ice throughout the GrIS and the exclusion of summer ice flow accelerations (Section 2.2.2). Two sensitivity tests were carried out in order to estimate the error caused by these assumptions (Section 2.2.7). In accordance with the theory – which predicts weaker bed-to-surface transfer where the basal slip ratio is low (Gudmundsson, 2003) – these tests demonstrated that the underestimation of basal slip ratios leads to the underestimation of the surface relief (Sections 2.3.4 and 2.4.2.2). However, the effects on the surface relief of the GrIS due to the exclusion of summer ice flow accelerations are moderate (~ 6.6%) and restricted to the vicinity of the ice sheet margin (Sections 2.3.4 and 2.4.2.2). Effects due to the assumption of fully temperate ice are generally stronger – especially towards the interior of the ice sheet – though the spatial pattern of the surface relief is not altered significantly (Sections 2.3.4 and 2.4.2.2). Another key limitation of the basal slip ratio dataset is its inability to capture mesoscale basal slipperiness perturbations (Section 2.2.3). However, sensitivity tests (Section 2.2.6) showed that – in accordance with the theory (Gudmundsson, 2003) – the response of the surface topography to basal slipperiness perturbations is small (< 20-25%) compared to the response to basal topographical perturbations of similar phase and magnitude (Sections 2.3.3 and 2.4.1).

Uncertainties caused by the limitations of my surface drainage datasets predominantly affect the results in Chapter 3. Surface lakes, rivers and moulins which were compared with the observed surface relief in SW Greenland (Sections 3.2.1 and 3.2.3), were derived by Yang and Smith (2016) from Landsat-8 panchromatic imagery (15 m resolution) acquired on 19 August 2013. Although surface lakes could be surveyed from this imagery with high accuracy, a large number of surface rivers and moulins were missed due to their small size (Yang and Smith, 2016). Furthermore, this dataset only provides a one-day snapshot for a small area in SW Greenland, thus it is not possible to investigate the temporal evolution – and maximum coverage – of the surface drainage system across the whole GrIS, and its relation to the surface relief. This

has been circumvented by surveying potential surface lakes, rivers and moulins from surface DEMs – GIMP-DEM (Howat et al., 2014; 2017) – and the MEaSUREs ice flow velocity dataset (Joughin et al., 2010; 2017) (Section 3.2.2). After filtering – to remove the noise introduced by the surface DEM – the surface depression dataset (Section 3.2.2.1) provides a good proxy for surface lakes by delineating their maximum potential distribution (Section 3.3.1). However, the 78 % recall and 31 % precision below the ELA indicate that several factors still hinder the accuracy of the surface depression dataset, e.g. presence of water or ice filled depressions, shallow depressions (within the GIMP-DEM 1σ vertical error), crevasses, moulins, narrow surface channels (Section 3.3.1). The density of the maximum potential river network – i.e. surface channels derived from surface DEMs – is dependent on the choice of the minimum catchment area, though the qualitative spatial distribution is largely unaffected by it (Section 3.3.2.2). Hence, the largest limitation to the accuracy of my potential river dataset – i.e. its alignment with actual surface rivers – is caused by the presence of crevasses (Section 3.4). Using principal strain rates – calculated from winter ice flow velocities – to estimate the maximum distribution of moulins has many advantages (Section 3.2.2.3), though the exclusion of summer ice flow accelerations could lead to a degree of underestimation (e.g. Christoffersen et al., 2018; Hoffman et al., 2018).

3.) Uncertainties in modelled contemporary and future datasets

Datasets that were obtained predominantly via numerical modelling are less frequently used in my thesis. Nevertheless limitations of the SICOPOLIS-derived ice thickness, basal slip ratio and SMB datasets (Vizcaino et al., 2014), and the MAR-derived SMB and surface runoff datasets (Fettweis et al., 2013, 2017) affect the outcomes of Chapter 4 and to a lesser degree Chapter 3.

Contemporary ELA and surface runoff datasets obtained from ERA-Interim forced MAR (Fettweis et al., 2013, 2017), were used to represent current conditions in the surface lake projections assuming constant surface topography (Sections 4.2.1 and 4.3.1), and were used exclusively in Chapter 3. ERA-Interim is a state-of-the-art atmospheric re-analysis – i.e. assimilation of observed data from different sources into forecast models – which provides spatially complete and physically coherent datasets about atmospheric conditions (Dee et al., 2011). Although SMB cannot be derived directly from the ERA-Interim due to its resolution and simplified physics, the MAR – which is a regional climate model developed for polar regions – estimates SMB

successfully (<10% uncertainty) when forced with ERA-Interim data (Fettweis et al., 2013, 2017). In fact, due to the lack of ice sheet wide observations, ERA-Interim forced MAR outputs have been used by several studies as a standard against which other simulations are compared (e.g. Fettweis et al., 2013, 2017). Hence, uncertainty of the contemporary ELAs and surface runoff is expected to be relatively low.

Future SMB projections obtained from MAR – and used for surface lake projections assuming constant surface relief in Chapter 4 (Sections 4.2.1 and 4.3.1) – are less accurate due to the use of general circulation models (GCM) and constant ice surface topography (Fettweis et al., 2013). However, Fettweis et al. (2013) only published the outputs of the three best performing – against historical ERA-Interim forced outputs – GCMs. Furthermore, the MIROC5 forced SMB projections are close to the multi-model mean – calculated from 30 Coupled Model Intercomparison Project Phase 5 GCMs – while the NorESM1 and CanESM2 systematically over- and underestimates it, respectively (Fettweis et al., 2013). Hence, using MAR projections forced by all three GCMs provides a good envelope of output for my surface lake projections. Fettweis et al. (2013) proposed that the uncertainty caused by using constant ice surface topography – and thus the exclusion of the melt-elevation feedback – is relatively low, causing around 8% additional mass loss. However, this effect could be more significant in some regions of the ice sheet – e.g. in NE Greenland (Vizcaino et al., 2014) – as discussed in Section 4.4.3.

Surface lake projections, which incorporate the effects of the changing surface relief (Section 4.2.2 and 4.3.2), are affected by the limitations of the datasets obtained from SICOPOLIS ice sheet modelling (Vizcaino et al., 2014). Although the SICOPOLIS based GrIS model of Vizcaino et al. (2014) is fully coupled to an atmosphere-ocean model and unphysical corrections were not employed (Section 4.2.2.1), the limited resolution, simplified representation of surface processes (e.g. no coupling between surface albedo and snowfall), and application of SIA hinders its performance (Vizcaino et al., 2014). This is demonstrated by the fact that the modelled contemporary GrIS extends beyond the observed ice sheet in most cases, except in the NW (Vizcaino et al., 2014). Historical SICOPOLIS simulations also underestimate observed GrIS mass loss between 1990 and 2013 – which is mainly attributed to the acceleration of outlet glaciers driven by ocean forcing (Joughin et al., 2012; Moon et al., 2012; Shepherd et al., 2012) – due to exclusion of longitudinal stress fields and simplified representation of tidewater glaciers (Vizcaino et al., 2014). Hence, future changes, especially around major outlet glaciers, might also be underestimated

(Vizcaino et al., 2014). I have mitigated these problems by handling surface lake projections based on SICOPOLIS model results (Sections 4.2.2 and 4.3.2) separately from the projections that are based on the observed contemporary ice sheet topography and MAR SMB projections (Sections 4.2.1 and 4.3.1). Another key limitation is that basal slipperiness perturbations cannot be derived from SICOPOLIS simulation outputs due to the limited spatial resolution and usage of SIA (Section 4.2.2.1). However, this is similar to the contemporary situation (Section 2.2.3), and thus the quality of my results in Section 4.3.2 are consistent with the contemporary calculations in Chapter 2 (Sections 2.2.6 and 2.3.6).

4.) Uncertainty associated with the projection of surface lake distribution, volume and rapid drainage

My surface lake projections – using both constant and evolving ice surface topography (Sections 4.3.1 and 4.3.2) – assume that all depressions below the ELA host lakes. Although the inland expansion of surface lakes correlates well with the rising ELA (Howat et al., 2013) and the majority (~80%) of contemporary surface lakes form below the ELA (Section 3.3.1), this approach excludes high elevation surface lakes and might overestimate surface lake distribution below the ELA as not all depressions host lakes, e.g. due to the presence of perennial crevasses, moulins and narrow surface channels (Section 3.3.1). Based on the ice sheet-wide ratio of surface lakes below the ELA (81%), and the ice sheet wide recall (78%) and precision (68% when weighed by the volume of depression), I proposed in Section 3.3.1 that the overall uncertainty of my surface lake volume projections is below 40%.

My surface lake projections (Sections 4.3.1 and 4.3.2) also assume that surface depressions below the ELA uniformly fill up with meltwater to 20% of their full volume. This assumption is based on comparisons between the seasonal maximum volume of surface lakes – derived from MODIS imagery – and the volume of their host surface depressions (Section 4.2.1.1). Although the seasonal evolution of surface lakes is disregarded by my projections, it provides a robust estimation of the maximum volume of meltwater that could be injected to the ice sheet bed via the rapid drainage of surface lakes during a given melt season. Nevertheless, the uniform value of meltwater infilling proportion introduces uncertainty into my projections, as this statistic was shown to vary across the GrIS, with lower latitudes experiencing higher percentages (Section 4.3.1.2). As 20% is lower than the ice sheet-wide median meltwater infilling

proportion and the climate is expected to become warmer, my surface lake volume projections are conservative (Section 4.3.1.2).

Two other sources of uncertainty only affect certain aspects of my surface lake projections. Firstly, the conversion of surface relief to net depression volume limits the accuracy of my surface lake projections incorporating the effects of changing surface topography (Section 4.3.2). As shown by tests on the contemporary GrIS, the observed volume of surface depressions is underestimated by my calculations, which convert the surface relief to surface depression volume (Section 4.3.2.4). Secondly, my calculations estimating the probability of rapid lake drainage – similar in the case of constant and evolving surface topography (Sections 4.2.1 and 4.2.2) – are limited by the exclusion of tensile shock events (e.g. Christoffersen et al., 2018; Hoffman et al., 2018), summer ice flow accelerations, and the poorly quantified elastic shear modulus of ice across the GrIS (Section 4.2.1.3). Due to these factors, the probability of rapid lake drainage is potentially underestimated by my calculations. This is confirmed by comparisons with the observed relative frequency of rapid lake drainage on the GrIS, which – after correcting for the observational bias (Cooley and Christoffersen, 2017) – are generally higher than my estimations (Section 4.4.2).

5.3. Future work

There are several ways to improve the accuracy of my calculations and to open up further research avenues. Firstly, the precision of surface lake projections might be improved by employing a more sophisticated projection approach, instead of simply assuming that every depression below the ELA fills up uniformly with meltwater (Section 4.2.1). Section 4.3.1.2 demonstrated that the meltwater infilling proportion of surface depressions varies with latitude. Hence, it is a reasonable to assume that a more negative SMB – indicative of larger surface melt – leads to higher meltwater infilling proportions. This could be investigated by creating a large database of maximum (within a given melt season) surface lake volumes – similar to the one I created in Section 4.2.1.1, but over a larger region and a longer time period – and compare it with the volumes of the host depressions and the SMB. If a significant correlation is found, SMB could be used to infer the meltwater infilling proportion of surface depressions, even if they are above the ELA. This is a promising way to simply improve the precision of surface lake projections, which would not only benefit investigations on the GrIS, but would make it more feasible to conduct such studies on the Antarctic Ice

Sheet (AIS). The latter is especially important given the recent publication of a high resolution ice sheet-wide surface DEM (Howat et al., 2018), and recent studies demonstrating that surface lakes might be more important and widespread on the AIS then previously assumed (Banwell et al., 2013, 2014, Kingslake et al., 2017).

Another way to widen the scope of this work is to carry out the approach of Chapter 2 on the AIS. This possibility is somewhat hindered by the lack of an ice sheet-wide high resolution bed DEM, as Bedmap2 – which is the best continental-scale bed DEM of the AIS – is based on unevenly distributed ice thickness measurements, and only has a resolution of 5 km (Fretwell et al., 2013). However, high resolution bed DEMs are available for certain smaller regions of the AIS, e.g. the Pine Island Glacier (Bingham et al., 2017). Although this would be an incremental step, applying the technique on flowlines covering a wider range of glaciological parameters – which is likely the case on the AIS, especially due to the more widespread presence of ice streams compared to the GrIS – might reveal additional insights regarding the precision of the non-stationary bed-to-surface transfer theory (Ng et al., 2018), which could inform more ambitious future investigations. One of these is the potential extension of the non-stationary bed-to-surface transfer theory – which is currently solved only for ice flowlines – to 3D (Ng et al., 2018). A preliminary study on the AIS using the available theory might reveal the full-scale of the potential benefits of such a theoretical advancement, which are likely moderate on the GrIS according to my conclusions (Section 2.4).

Another promising avenue is the application of the non-stationary bed-to-surface transfer theory to carry out inversions for basal slipperiness perturbations using perturbations in the surface topography, surface velocity and bed topography – this approach could be more computationally efficient than previous numerical inversions (Section 1.2.3). The theoretical foundations have already been outlined by Ng et al. (2018), though further work is needed on the optimisation procedure which offsets the complications caused by the uncertainties of bed topography, and the weak dependence of surface topography and velocity perturbations on basal slipperiness perturbations (Ng et al., 2018).

The approach outlined in this thesis could also be used to estimate the spatiotemporal evolution of the surface drainage network on palaeo ice sheets (Section 1.2.4), as the mesoscale surface topographical variations – which control the routing of surface meltwater (Chapter 3) – can be predicted without solving the computationally expensive full Stokes equations at high resolution (Chapter 2). This is perhaps the most

interesting potential research avenue as the short observational window – i.e. a couple of decades – of hydro-dynamical processes is a key limitation that currently hinders our understanding of the long-term (centennial to millennial) net effects of hydrology on ice sheet evolution (Section 1.1). Comparing the reconstructed spatiotemporal changes of the surface drainage network with reconstructed subglacial meltwater pathways (e.g. Livingstone et al., 2013), empirical ice sheet retreat rates, and subglacial meltwater landforms might provide a solution for the problem discussed above and could also provide insights into the genesis of subglacial landforms. The recent publication of good quality, high resolution DEMs of formerly glaciated areas – e.g. the ArcticDEM (Release 5, DigitalGlobe Inc., 2017) – and the quickly improving precision and spatiotemporal resolution of empirically constrained palaeo ice sheet reconstructions (e.g. Clark et al., 2012; Hughes et al., 2016) provide a good basis for such investigations.

REFERENCES

Alessio, S., (2016). *Digital signal processing and spectral analysis for scientists*. Switzerland: Springer International Publishing. doi: 10.1007/978-3-319-25468-5

Alley, R., Blankenship, D., Bentley, C., Rooney, S., (1986). Deformation of till beneath ice stream B, West Antarctica. *Nature*. **322**(6074), 57-59. doi: 10.1038/322057a0

Andrews, L., Catania, G., Hoffman, M., Gulley, J., Lüthi, M., Ryser, C., Hawley, R., Neumann, T. (2014). Direct observations of evolving subglacial drainage beneath the Greenland Ice Sheet. *Nature,* **514**, 80-83. doi: 10.1038/nature13796

Andrews, L., Hoffman, M., Neumann, T., Catania, G., Lüthi, M., Hawley, R., Schild, K., Ryser, C., Morriss, B., (2018). Seasonal evolution of the subglacial hydrologic system modified by supraglacial lake drainage in Westren Greenland. *Journal of Geophysical Research: Earth Surface*. **123**(6), 1479-1496. doi: 10.1029/2017JF004585

Arnold, N., Banwell, A., Willis, I., (2014). High-resolution modelling of the seasonal evolution of surface water storage on the Greenland Ice Sheet. *The Cryosphere*. **8**(4), 1149-1160. doi: 10.5194/tc-8-1149-2014

Banwell, A., Arnold, N., Willis, I., Tedesco, M., Ahlstrøm, A., (2012). Modeling supraglacial water routing and lake filling on the Greenland Ice Sheet. *Journal of Geophysical Research*. **117**(F4), F04012. doi: 10.1029/2012JF002393

Banwell, A., Caballero, M., Arnold, S.N., Glasser, F.N., Cathles M.L., MacAyeal, R.D., (2014). Supraglacial lakes on the Larsen B ice shelf, Antarctica, and at Paakitsoq, West Greenland: a comparative study. *Annals of Glaciology*. **55**(66), 1-8. doi: 10.3189/2014AoG66A049

Banwell, A., MacAyeal, D., Sergienko, O., (2013) Breakup of the Larsen B Ice Shelf triggered by chain reaction drainage of supraglacial lakes. *Geophysical Research Letters*. **40**(22), 5871-5876. doi: 10.1002/2013GL057694

Banwell, A., Hewitt, I., Willis, I., Arnold, N., (2016). Moulin density controls drainage development beneath the Greenland Ice Sheet. *Journal of Geophysical Research: Earth Surface*. **121**(12), 2248-2269. doi: 10.1002/2015JF003801

Bartholomew, I., Nienow, P., Mair, D., Hubbard, A., King., M., Sole, A., (2010). Seasonal evolution of subglacial drainage and acceleration in a Greenland outlet glacier. *Nature Geoscience*. **3**, 408-411. doi: 10.1038/ngeo863

Bartholomew, I., Nienow, P., Sole, A., Mair, D., Cowton, T., King, M., (2012). Short-term variability in Greenland Ice Sheet motion forced by time-varying meltwater drainage: Implications for the relationship between subglacial drainage system behaviour and ice velocity. *Journal of Geophysical Research: Earth Surface*. **117**(F3). doi: 10.1029/2011JF002220

Bingham, R., Nienow, P., Sharp, M., Boon, S., (2005). Subglacial drainage processes at a High Arctic polythermal valley glacier. *Journal of Glaciology*. **51**(172), 15-23. doi: 10.3189/172756505781829520

Bingham, R., Nienow, P., Sharp, M., Copland, L., (2006). Hydrology and dynamics of a polythermal (mostly cold) High Arctic glacier. *Earth Surface Processes and Landforms*. **31**(12), 1463-1479. doi: 10.1002/esp.1374

Bingham, R., Siegert, M., (2009). Quantifying subglacial bed roughness in Antarctica: implications for ice-sheet dynamics and history. *Quaternary Science Reviews*. **28**(3-4), 223-236. doi: 10.1016/j.quascirev.2008.10.014

Bingham, R., Vaughan, D., King, E., Davies, D., Cornford, S., Smith, A., Arthern, R., Brisbourne, A., De Rydt, J., Graham, A., Spagnolo, M., Marsh, O., Shean, D., (2017). Diverse landscapes beneath Pine Island Glacier influence ice flow. *Nature Communications*. **8**, 1618. doi: 10.1038/s41467-017-01597-y

Black, H., Budd, W., (1964). Accumulation in the region of Wilkes, Wilkes Land, Antarctica. *Journal of Glaciology*. **5**(37), 3-15. doi: 10.3189/S0022143000028549

Bougamont, M., Christoffersen, P., Hubbard, A., Fitzpatrick, A., Doyle, S., Carter, S., (2014). Sensitive response of the Greenland Ice Sheet to surface melt drainage over a soft bed. *Nature Communications*. **5**, 5052. doi: 10.1038/ncomms6052

Box, J., Ski, K., (2007). Remote sounding of Greenland supraglacial melt lakes: implications for subglacial hydraulics. *Journal of Glaciology*. **53**(181), 257-265. doi: 10.3189/172756507782202883

Brisbourne, A., Smith, A., Vaughan, D., King, E., Davies, D., Bingham, R., Smith, E., Nias, I., Rosier, S., (2017). Bed conditions of Pine Island Glacier, West Antarctica. *Journal of Geophysical Research: Earth Surface*. **122**(1), 419-433. doi: 10.1002/2016JF004033

Carroll, D., Sutherland, D., Shroyer, E., Nash, J., Catania, G., Stearns, L., (2015). Modeling turbulent subglacial meltwater plumes: implications for fjord-scale buoyancy-driven circulation. *Journal of Physical Oceanography*. **45**, 2169-2185. doi: 10.1175/JPO-D-15-0033.1

Catania, G., Neumann, T., (2010). Persistent englacial drainage features in the Greenland Ice Sheet. *Geophysical Research Letters*. **37**(2), L02501. doi: 10.1029/2009GL041108

Chandler, D., Wadham, J., Lis, G., Cowton, T., Sole, A., Bartholomew, I., Telling, J., Nienow, P., Bagshaw, E., Mair, D., Vinen, S., Hubbard, A., (2013). Evolution of the subglacial drainage system beneath the Greenland Ice Sheet revealed by tracers. *Nature Geoscience*. **6**, 195-198. doi: 10.1038/NGEO1737

Chang, M., Jamieson, S., Bentley, M., Stokes, C., (2016). The surficial and subglacial geomorphology of western Dronning Maud Land, Antarctica. *Journal of Maps*. **12**(5), 892-903. doi: 10.1080/17445647.2015.1097289

Christoffersen, P., Bougamont, M., Hubbard, A., Doyle, S., Grigsby, S., Petterson, R., (2018). Cascading lake drainage on the Greenland Ice Sheet triggered by tensile shock and fracture. *Nature Communications*. **9**, 1064. doi: 10.1038/s41467-018-03420-8

Clark, C., Hughes, A., Greenwood, S., Jordan, C., Sejrup, H., (2012) Pattern and timing of retreat of the last British-Irish Ice Sheet. *Quaternary Science Reviews*. **44**, 112-146. doi: 10.1126/science.1153360

Clason, C., Mair, D., Nienow, Bartholomew, I., Sole, A., Palmer, S., Schwangart, W., (2015). Modelling the transfer of supraglacial meltwater to the bed of Leverett Glacier, Southwest Greenland. *The Cryosphere*. **9**(1), 123-138. doi: 10.5194/tc-9-123-2015

Colgan, W., Steffen, K., McLamb, S.W., Abdalati, W., Rajaram, H., Motyka, R., Phillips, T., Anderson, R., (2011). An increase in crevasse extent, West Greenland: Hydrologic implications. *Geophysical Research Letters*. **38**(18), L18502. doi: 10.1029/2011GL048491

Cooley, S., Christoffersen, P., (2017). Observation bias correction reveals more rapidly draining lakes on the Greenland Ice Sheet. *Journal of Geophysical Research: Earth Surface*. **122**(10), 1867-1881. doi: 10.1002/2017JF004255

Copeland, L., Sharp, M., Nienow, P., (2003). Links between short-term velocity variations and the subglacial hydrology of a predominantly cold polythermal glacier. *Journal of Glaciology*. **49**(166), 337-348. doi: 10.3189/172756503781830656

Cowton, T., Slater, D., Sole, A., Goldberg, D., Nienow, P., (2015). Modeling the impact of glacial runoff on fjord circulation and submarine melt rate using a new subgrid-scale parameterization for glacial plumes. *Journal of Geophysical Research: Oceans*. **120**(2), 796-812. doi: 10.1002/2014JC010324

Cowton, T., Nienow, P., Sole, A., Bartholomew, I., Mair, D., (2016). Variability in ice motion at a land-terminating Greenland outlet glacier: the role of channelized and distributed drainage system. *Journal of Glaciology*. **62**(233), 451-466. doi: 10.1017/jog.2016.36

Cowton, T., Sole, A., Nienow, P., Slater, D., Christoffersen, P., (2018). Linear response of east Greenland's tidewater glaciers to ocean/atmosphere warming. *PNAS*. **115**(31), 7907-7912. doi: 10.1073/pnas.1801769115

Cuffey, K. and Paterson, W., (2010). *The Physics of Glaciers*. 4th ed. New York, N.Y.: Academic Press, Elsevier.

Das, S., Joughin, I., Benn, D., Howat, I., King, M., Lizarralde, D., Bhatia, M., (2008). Fracture propagation to the base of the Greenland Ice Sheet during supraglacial lake drainage. *Science*. **320**(5877), 778-781. doi: 10.1126/science.1153360

De Rydt, J., Gudmundsson, H., Corr, J., Christoffersen, P., (2013). Surface undulations of Antarctic ice streams tightly controlled by bedrock topography. *The Cryosphere*. **7**(2), 407-417. doi: 10.5194/tc-7-407-2013

Dee, D., Uppala, S., Simmons, A., Berrisford, P., Poli, P., Kobayashi, S., Andrae, U., Balmaseda, M., Balsamo, G., Bauer, P., Bechtold, P., Beljaars, A., van de Berg, L., Bidlot, J., Bormann, N., Delsol, C., Dragani, R., Fuentes, M., Geer, A., Haimberger, L., Healy, S., Hersbach, H., Hólm, E., Isaksen, L., Kållberg, P., Köhler, M., Matricardi, M., McNally, A., Monge-Sanz, B., Morcrette, J.-J., Park, B.-K., Peubey, C., de Rosnay, P., Tavolato, C., Thépaut, J.-N., Vitart, F., (2011) The ERA-Interim reanalysis: configuration and performance of the data assimilation system. *Quarterly Journal of the Royal Meteorological Society*. **137**(656), 553-597. doi: 10.1002/qj.828

Dow, C., Kulessa, B., Rutt, I., Doyle, S., Hubbard, A., (2014). Upper bounds on subglacial channel development for interior regions of the Greenland Ice Sheet. *Journal of Glaciology*. **60**(224), 1044-1051. doi: 10.3189/2014JoG14J093

Dow, C., Kulessa, B., Rutt, I., Tsai, V., Pimentel, S., Doyle, S., van As, D., Linbäck, K., Pettersson, R., Jones, G., Hubbard, A., (2015). Modeling of subglacial hydrological development following rapid supraglacial drainage. *Journal of Geophysical Research: Earth Surface*. **120**(6), 1127-1147. doi: 10.1002/2014JF003333

Doyle, S., Hubbard, A., Fitzpatrick, A., van As, D., Mikkelsen, A., Pettersson, R., Hubbard, B., (2014). Persistent flow acceleration within the interior of the Greenland ice sheet. *Geophysical Research Letters*. **41**(3), 899-905. doi: 10.1002/2013GL058933

Echelmeyer, K., Clarke T., Harrison, W., (1991). Surficial glaciology of Jakobshavn Isbrae, West Greenland: part I. Surface-morphology. *Journal of Glaciology*. **37**(127), 368-382. doi: 10.3189/S0022143000005803

Enderlin, E., Howat, I., Jeong, S., Noh, M., van Angelen, J., van den Broeke, M., (2014). An improved mass budget for the Greenland ice sheet. *Geophysical Research Letters*. **41**(3), 866-872. doi: 10.1002/2013GL059010

Fettweis, X., Box, J., Agosta, C., Amory, C., Kittel, C., Lang, C., van As, D., Machguth, H., Gallée, H., (2017). Reconstructions of the 1900-2015 Greenland ice sheet surface mass balance using the regional climate MAR model. *The Cryopshere*. **11**(2), 1015-1033. doi: 10.5194/tc-11-1015-2017

Fettweis, X., Franco, B., Tedesco, M., van Angelen, H.J., Lenaerts, M.T.J., van den Broeke, R.M., Gellée, H., (2013). Estimating the Greenland ice sheet surface mass balance contribution to future sea level rise using the regional atmospheric climate model MAR. *The Cryosphere*. **7**(2), 469-489. doi: 10.5194/tc-7-469-2013

Fitzpatrick, A., Hubbard, A., Box, J., Quincey, D., van As, D., Mikkelsen, A., Doyle, S., Dow, C., Hasholt, B., Jones, G., (2014). A decade (2002-2012) of supraglacial lake volume estimates across Russell Glacier, West Greenland. *The Cryosphere*. **8**(1), 107-121. doi: 10.5194/tc-8-107-2014

Flowers, G., (2010). Glacier hydromechanics: early insights and the lasting legacy of three works by Iken and colleagues. *Journal of Glaciology*. **56**(200), 1069-1078. doi: 10.3189/002214311796406103

Flowers, G., (2015). Modelling water flow under glaciers and ice sheets. *Proceedings of the Royal Society A*. **471**(2176), 20140907. doi: 10.1098/rspa.2014.0907

Fretwell, P., Pritchard, H., Vaughan, D., Bamber, J., Barrand, N., Bell, R., Bianchi, C., Bingham, R., Blankenship, D., Casassa, G., Catania, G., Callens, D., Conway, H., Cook, A., Corr, H., Damaske, D., Damm, V., Ferraccioli, F., Forsberg, R., Fujita, S., Gim, Y., Gogineni, P., Griggs, J., Hindmarsh, R., Holmlund, P., Holt, J., Jacobel, R., Jenkins, A., Jokat, W., Jordan, T., King, E., Kohler, J., Krabill, W., Riger-Kusk, M., Langley, K., Leitchenkov, G., Leuschen, C., Luyendyk, B., Matsuoka, K., Mouginot, J., Nitsche, F., Nogi, Y., Nost, O., Popov, S., Rignot, E., Rippin, D., Rivera, A., Roberts, J., Ross, N., Siegert, M., Smith, A., Steinhage, D., Studinger, M., Sun, B., Tinto, B., Welch, B., Wilson, D., Young, D., Xiangbin, C., Zirizzotti, A., (2013) Bedmap2: improved ice bed, surface and thickness datasets for Antarctica. *The Cryosphere*. **7**(1), 375-393. doi: 10.5194/tc-7-375-2013

Gledhill, L., Williamson, A., (2017). Inland advance of supraglacial lakes in north-west Greenland under recent climatic warming. *Annals of Glaciology*. **59**(79pt1), 66-82. doi: 10.1017/aog.2017.31

Gow, J., Rowland, R., (1965). On the relationship of snow accumulation to surface topography at “Byrd Station”, Antarctica. *Journal of Glaciology*. **5**(42), 843-847. doi: 10.3189/S0022143000018906

Gregoire, L., Payne, A., Valdes, P., (2012). Deglacial rapid sea level rises caused by ice-sheet saddle collapse. *Nature*. **487**, 219-222. doi: 10.1038/nature11257

Greuell, W., Reijmer, C., Oerlemans, J., (2002). Narrowband-to-broadband albedo conversion for glacier ice and snow based on aircraft and near-surface measurements. *Remote Sensing of Environment*. **82**(1), 48–63. doi: 10.1016/S0034-4257(02)00024-X

Gudmundsson, H., (2003). Transmission of basal variability to a glacier surface. *Journal of Geophysical Research*. **108**(B5), 2253. doi: 10.1029/2002JB002107

Gudmundsson, H., Raymond, C., Bindschadler, R., (1998). The origin and longevity of flow stripes on Antarctic ice streams. *Annals of Glaciology*. **27**, 145-152. doi: 10.3189/1998AoG27-1-145-152

Gumley, L., Descloitres, J., Schmaltz, J., (2007). Creating reprojected MODIS True Color images: A Tutorial, 19 pp.
URL ftp://ftp.ssec.wisc.edu/pub/IMAPP/MODIS/TrueColor

Harrington, J., Humphrey, N., Harper, J., (2015). Temperature distribution and thermal anomalies along a flowline of the Greenland Ice Sheet. *Annals of Glaciology*. **56**(70), 98-104. doi: 10.3189/2015AoG70A945

Hawkings, J., Wadham, J., Tranter, M., Lawson, E., Sole, A., Cowton, T., Tedstone, A., Bartholomew, I., Nienow, P., Chandler, D., Telling, J., (2015). The effect of warming climate on nutrient and solute export from the Greenland Ice Sheet. *Geochemical Perspectives Letters*. **1**(1), 94-104. doi: 10.7185/geochemlet.1510

Hodgkins, R., (1997). Glacier hydrology in Svalbard, Norwegian High Arctic. *Quaternary Science Reviews*. **16**(9), 957-973. doi: 10.1016/S0277-3791(97)00032-2

Hoffman, M., Andrews, L., Price, S., Catania, G., Neumann, T., Lüthi, M., Gulley, J., Ryser, C., Hawley, R., Morriss, B., (2017). Greenland subglacial drainage evolution regulated by weakly connected regions of the bed. *Nature Communications*. **7**, 13903. doi: 10.1038/ncomms13903

Hoffman, M., Perego, M., Andrews, L., Price, S., Neumann, T., Johnson, J., Catania, G., Lüthi, M., (2018). Widespread moulin formation during supraglacial lake drainages in Greenland. *Geophysical Research Letters*. **45**(2), 778-788. doi: 10.1002/2017GL075659

Hooke, R., (1989). Englacial and subglacial hydrology: a qualitative review. *Arctic and Alpine Research*. **21**(3), 221-233. doi: 10.1080/00040851.1989.12002734

Howat, I., Morin, P., Porter, C., Noh, M-J., (2018) *The Reference Elevation Model of Antarctica, Version 1*. Harvard Dataverse. doi: 10.7910/DVN/SAIK8B

Howat, I., Negrete, A., Smith, B., (2014) The Greenland Ice Mapping Project (GIMP) land classification and surface elevation data sets. *The Cryosphere*. **8**(4), 1509-1518. doi: 10.5194/tc-8-1509-2014

Howat, I., Negrete, A., Smith, B., (2017). *MEaSUREs Greenland Ice Mapping Project (GIMP) Digital Elevation Model from GeoEye and WorldView Imagery, Version 1*. Boulder, Colorado USA. NASA National Snow and Ice Data Center Distributed Active Archive Center. doi: 10.5067/H0KUYVF53Q8M

Howat, I., de la Peña, S., van Angelen, J., Lenaerts, J., van den Broeke, M., (2013). Brief communication "Expansion of meltwater lakes on the Greenland ice sheet". *The Cryosphere*. **7**(1), 201-204. doi: 10.5194/tc-7-201-2013

Hughes, A., Gyllencreutz, R., Lohne, Ø., Mangerud, J., Svendsen, J., (2016) The last Eurasian ice sheets – a chronological database and time-slice reconstruction, DATED-1. *Boreas*. **41**(1), 1-45. doi: 10.1111/bor.12142

Ignéczi, Á., Sole, A., Livingstone, S., Fettweis, X., Selmes, N., Gourmelen, N., Briggs, K., (2016). Northeast sector of the Greenland Ice Sheet to undergo the greatest inland expansion of supraglacial lakes during the 21st century. *Geophysical Research Letters*. **43**(18), 9729–9738. doi: 10.1002/2016GL070338

Ignéczi, Á., Sole, A., Livingstone, S., Ng, F., Yang, K., (2018). Greenland Ice Sheet surface topography and drainage structure controlled by the transfer of basal variability. *Frontiers in Earth Science*. **6**(101). doi: 10.3389/feart.2018.00101

Iken, A., (1974). *Velocity fluctuations of an Arctic valley glacier; a study of White Glacier, Axel Heiberg Island, Canadian Arctic Archipelago*. Ph.D. thesis, McGill University, Montréal, Québec. doi: 10.3929/ethz-a-000090485

Iken, A., (1981). The effect of the subglacial water pressure on the sliding velocity of a glacier in an idealized numerical model. *Journal of Glaciology*. **27**(97), 407-421. doi: 10.3189/S0022143000011448

Iken, A., Bindschadler, R., (1986). Combined measurements of subglacial water pressure and surface velocity of Findelengletscher, Switzerland: conclusions about drainage system and sliding mechanism. *Journal of Glaciology*. **32**(110), 101-119. doi: 10.3189/S0022143000006936

Iken, A., Röthlisberger, H., Flotron, A., Haeberli, W., (1983). The uplift of Unteraargletscher at the beginning of the melt season – a consequence of water storage at the bed? *Journal of Glaciology*. **29**(101), 28-47. doi: 10.3189/S0022143000005128

IPCC, 2013: Climate Change 2013: The Physical Science Basis. Contribution of Working Group I to the Fifth Assessment Report of the Intergovernmental Panel on Climate Change [Stocker, T.F., D. Qin, G.-K. Plattner, M. Tignor, S.K. Allen, J. Boschung, A. Nauels, Y. Xia, V. Bex and P.M. Midgley (Eds.)]. Cambridge, UK and New York, NY, USA: Cambridge University Press. pp. 1535. doi: 10.1017/CBO9781107415324

Irvine-Fynn, T., Hodson, A., Moorman, B., Vatne, G., Hubbard, A., (2011). Polythermal glacier hydrology: a review. *Reviews of Geophysics*. **49**(4), RG4002. doi: 10.1029/2010RG000350

Jamieson, A., Ross, N., Greenbaum, J., Young, D., Aitken, A., Roberts, J., Blakenship, D., Bo, S., Siegert, M., (2016). An extensive subglacial lake and canyon system in Princess Elizabeth Land, East Antarctica. *Geology*. **44**(2), 87-90. doi: 10.1130/G37220.1

Johansson, M., Jansson, P., Brown, I., (2013). Spatial and temporal variations in lakes on the Greenland Ice Sheet. *Journal of Hydrology*. **476**, 314-320. doi: 10.1016/j.jhydrol.2012.10.045

Jordan, T., Cooper, M., Schroeder, D., Williams, C., Paden, J., Siegert, M., Bamber, J., (2017). Self-affine subglacial roughness: consequences for radar scattering and basal water discrimination in northern Greenland. *The Cryosphere*. **11**(3), 1247-1264. doi: 10.5194/tc-11-1247-2017

Joughin, I., Das, S., Flowers, G., Behn, M., Alley, R., King, M., Smith, B., Bamber, J., van den Broeke, M., van Angelen, J., (2013). Influence of ice-sheet geometry and supraglacial lakes on seasonal ice-flow variability. *The Cryosphere*. **7**(4), 1185-1192. doi: 10.5194/tc-7-1185-2013

Joughin, I., Das, S., King, M., Smith, B., Howat, I., Moon, T., (2008). Seasonal speedup along the western flank of the Greenland Ice Sheet. *Science*. **320**(5877), 781-783. doi: 10.1126/science.1153288

Joughin, I., Smith, B., Howat, I., Scambos, T., (2017). *MEaSUREs Greenland Ice Sheet Velocity Map from InSAR Data, Version 2*. Boulder, Colorado USA. NASA National Snow and Ice Data Center Distributed Active Archive Center. doi: 10.5067/OC7B04ZM9G6Q

Joughin, I., Smith, B., Howat, I., Scambos, T., Moon, T., (2010). Greenland flow variability from ice-sheet-wide velocity mapping. *Journal of Glaciology*. **56**(197), 415-430. doi: 10.3189/002214310792447734

Kamb, B., Raymond, C., Harrison, W., Engelhardt, H., Echelmeyer, K., Humphrey, N., Brugman, M., Pfeffer, T. (1985). Glacier surge mechanism: 1982-1983 surge of Variegate Glacier, Alaska. *Science*. **227**(4686), 469-479. doi: 10.1126/science.227.4686.469

Karlstrom, L., Yang, K., (2016). Fluvial supraglacial landscape evolution on the Greenland Ice Sheet. *Geophysical Research Letters*. **43**(6), 2683-2692. doi: 10.1002/2016GL067697

Kingslake, J., Ng, F., Sole, A., (2015). Modelling channelized surface drainage of supraglacial lakes. *Journal of Glaciology*. **61**(225), 185-199. doi: 10.3189/2015JoG14J158

Kingslake, J., Ely, J., Das, I., Bell, R., (2017) Widespread movement of meltwater onto and across Antarctic ice shelves. *Nature*. **544**(7650), 269-386. doi: 10.1038/nature22049

Koenig, L., Lampkin, D., Montgomery, L., Hamilton, S., Turrin, J., Joseph, C., Moutsafa, S., Panzer, B., Casey, K., Paden, J., Leuschen, C., Gogineni, P., (2015). Wintertime storage of water in buried supraglacial lakes across the Greenland Ice Sheet. *The Cryosphere*. **9**(4), 1333-1342. doi: 10.5194/tc-9-1333-2015

Krawczynski, M., Behn, M., Das, S., Joughin, I., (2009). Constraints on the lake volume required for hydrofracture through ice sheets. *Geophysical Research Letters*. **36**(10), L10501. doi: 10.1029/2008GL036765

Kulessa, B., Hubbard, A., Booth, A., Bougamont, M., Dow, C., Doyle, S., Christoffersen, P., Lindbäck, K., Pettersson, R., Fitzpatrick, A., Jones, G., (2017). Seismic evidence for complex sedimentary control of Greenland Ice Sheet flow. *Science Advances*. **3**(8), e1603071. doi: 10.1126/sciadv.1603071

Kyrke-Smith, T., Gudmundsson, H., Farrell, P., (2017). Can seismic observations of bed conditions on ice streams help constrain parameters in ice flow models? *Journal of Geophysical Research: Earth Surface*. **122**(11), 2269-2282. doi: 10.1002/2017JF004373

Kyrke-Smith, T., Gudmundsson, H., Farrell, P., (2018). Relevance of detail in basal topography for basal slipperiness inversions: a case study on Pine Island Glacier, Antarctica. *Frontiers in Earth Science*. **6**(33), doi: 10.3389/feart.2018.00033

Lampkin, D., (2011). Supraglacial lake spatial structure in western Greenland during the 2007 ablation season. *Journal of Geophysical Research*. **116**(F4), F04001. doi: 10.1029/2010JF001725

Lampkin, D., VanderBerg J., (2011). A preliminary investigation of the influence of basal and surface topography on supraglacial lake distribution near Jakobshavn Isbrae, western Greenland. *Hydrological Processes*. **25**(21), 3347-3355. doi: 10.1002/hyp.8170

Lampkin, D., VanderBerg, J., (2014). Supraglacial melt channel networks in the Jakobshavn Isbræ region during the 2007 melt season. *Hydrological Processes*. **28**(25), 6038-6053. doi: 10.1002/hyp.10085

Langley, E., Leeson, A., Stokes, C., Jamieson, S., (2016). Seasonal evolution of supraglacial lakes on an east Antarctic outlet glacier. *Geophysical Research Letters*. **43**(16), 8563-8571. doi: 10.1002/2016GL069511

Leeson, A., Shepherd, A., Briggs, K., Howat, I., Fettweis, X., Morlighem, M., Rignot, E., (2015). Supraglacial lakes on the Greenland Ice Sheet advance inland under warming climate. *Nature Climate Change*. **5**, 51-55. doi: 10.1038/nclimate2463

Leeson, A., Shepherd, A., Palmer, S., Sundal, A., Fettweis, X., (2012). Simulating the growth of supraglacial lakes at the western margin of the Greenland Ice Sheet. *The Cryosphere*. **6**(5), 1077-1086. doi: 10.5194/tc-6-1077-2012

Leeson, A., Shepherd, A., Sundal, A., Johansson, M., Selmes, N., Briggs, K., Hogg, A., Fettweis, X., (2013). A comparison of supraglacial lake observations derived from MODIS imagery at the western margin of the Greenland ice sheet. *Journal of Glaciology*. **59**(218), 1179-1188. doi: 10.3189/2013JoG13J064

Liang, Y-L., Colgan, W., Lv, Q., Steffen, K., Abdalati, W., Stroeve, J., Gallaher, D., Bayou, N., (2012). A decadal investigation of supraglacial lakes in West Greenland using a fully automatic detection and tracking algorithm. *Remote Sensing of Environment*. **123**, 127-138. doi: 10.1016/j.rse.2012.03.020

Livingstone, S., Clark, C., Woodward, J., Kingslake, J., (2013). Potential subglacial lake locations and meltwater drainage pathways beneath the Antarctic and Greenland ice sheets. *The Cryosphere*. **7**(6), 1721-1740. doi: 10.5194/tc-7-1721-2013

Lliboutry, L., (1958). Contribution à la théorie du frottement du glacier sur son lit. *Comptes Rendus Hebdomadaires des Séances de l'Académie des Sciences (Paris)*. **247**(2), 228-230.

Lüthje, M., Pedersen, L., Reeh, N., Greuell, W., (2006). Modelling the evolution of supraglacial lakes on the west Greenland Ice Sheet margin. *Journal of Glaciology*. **52**(179), 608-618. doi: 10.3189/172756506781828386

MacGregor, J., Fahnestock, M., Catania, G., Aschwanden, A., Clow, G., Colgan, W., Gogineni, S., Morlighem, M., Nowicki, S., Paden, J., Price, S., Seroussi, H., (2016) A synthesis of the basal thermal state of the Greenland Ice Sheet. *Journal of Geophysical Research: Earth Surface*. **121**(7), 1328-1350. doi: 10.1002/2015JF003803

Machguth, H., MacFerrin, M., van As, D., Box, J., Charalampidis, C., Colgan, W., Fausto, R., Meijer, H., Mosley-Thompson, E., van de Wal, R., (2016). Greenland meltwater storage in firn limited by near-surface ice formation. *Nature Climate Change*. **6**, 390-393. doi: 10.1038/nclimate2899

Mallat, S., (2009). *A Wavelet tour of signal processing: the sparse way*. 3rd ed. Burlington, M.A.: Academic Press, Elsevier.

Margrave, G., (1998). Theory of nonstationary linear filtering in the Fourier domain with application to time-variant filtering. *Geophysics*. **63**(1), 244–259. doi: 10.1190/1.1444318

Maritorena, S., Morel, A., Gentili, B., (1994). Diffuse reflectance of oceanic shallow waters: Influance of water depth and bottom albedo. *Limnology and Oceanography*. **39**(7), 1689-1703. doi: 10.4319/lo.1994.39.7.1689

McMillan, M., Nienow, P., Shepherd, A., Benham, T., Sole, A., (2007). Seasonal evolution of supra-glacial lakes on the Greenland Ice Sheet. *Earth and Planetary Science Letters*. **262**(3-4), 484-492. doi: 10.1016/j.epsl.2007.08.002

Medley, B., Ligtenberg, S., Joughin, I., van den Broeke, M., Gogineni, S., Nowicki, S., (2015). Antarctic firn compaction rates from repeat-track airborne radar data: I. Methods. *Annals of Glaciology*. **56**(70), 155-166. doi: 10.3189/2015AoG70A203

Morlighem, M., Rignot, E., Mouginot, J., Seroussi, H., Larour, E., (2014). Deeply incised submarine glacial valleys beneath the Greenland ice sheet. *Nature Geoscience*. **7**, 418-422. doi: 10.1038/ngeo2167

Morlighem, M. et al., (2017a). *IceBridge BedMachine Greenland, Version 3*. Boulder, Colorado USA. NASA National Snow and Ice Data Center Distributed Active Archive Center. doi: 10.5067/2CIX82HUV88Y

Morlighem, M., Williams, C., Rignot, E., An, L., Arndt, J., Bamber, J., Catania, G., Chauché, N., Dowdeswell, J., Dorschel, B., Fenty, I., Hogan, K., Howat, I., Hubbard, A., Jakobsson, M., Jordan, T., Kjeldsen, K., Millan, R., Mayer, L., Mouginot, J., Noël, B., O'Cofaigh, C., Palmer, S., Rysgaard, S., Seroussi, H., Siegert, M., Slabon, P., Straneo, F., van den Broeke, M., Weinrebe, W., Wood, M., Zinglersen, K., (2017b). BedMachine v3: Complete bed topography and ocean bathymetry mapping of Greenland from multi-beam echo sounding combined with mass conservation. *Geophysical Research Letters*. **44**(21), 11051-11061. doi: 10.1002/2017GL074954

Morriss, B., Hawley, R., Chipman, J., Andrews, L., Catania, G., Hoffman, M., Lüthi, M., Neumann, T., (2013). A ten-year record of supraglacial lake evolution and rapid drainage in West Greenland using an automated processing algorithm for multispectral imagery. *The Cryosphere*. **7**(6), 1869-1877. doi: 10.5194/tc-7-1869-2013

Motyka, R., Hunter, L., Echelmeyer, Connor, C., (2003). Submarine melting at the terminus of a temperate tidewater glacier, Leconte Glacier, Alaska, USA. *Annals of Glaciology*. **36**(1), 57-65. doi: 10.3189/172756403781816374

Müller, F., Iken, A., (1973). Velocity fluctuations and water regime of Arctic valley glaciers. *International Association of Scientific Hydrology Publication 95 (Symposium at Cambridge 1969 – Hydrology of Glaciers)*. 165–182.

Murray, T., Dowdeswell, J., Drewry, D., Frearson, I., (1998). Geometric evolution and ice dynamics during a surge of Bakaninbreen, Svalbard. *Journal of Glaciology*. **44**(147), 263–272. doi: 10.3189/S0022143000002604

Ng, F., Ignéczi, A., Sole, A., Livingstone S., (2018). Response of surface topography to basal variability along glacial flowlines. *Journal of Geophysical Research: Earth Surface*. **123**(10), 2319-2340. doi: 10.1029/2017JF004555

Nienow, P., Hubbard, A., Hubbard, B., Chandler, D., Mair, D., Sharp, M., Willis, I., (2005). Hydrological controls on diurnal ice flow variability in valley glaciers. *Journal of Geophysical Research: Earth Surface*. **110**(F4), F04002. doi: 10.1029/2003JF000112

Nienow, P., Sole, A., Slater, D., Cowton, T., (2017). Recent advances in our understanding of the role of meltwater in the Greenland Ice Sheet system. *Current Climate Change Reports*. **3**(4), 330-344. doi: 10.1007/s40641-017-0083-9

Noh, M-J., Howat, I., (2015). Automated stereo-photogrammetric DEM generation at high latitudes: Surface Extraction with TIN-based Search-space Minimization (SETSM) validation and demonstration over glaciated region. *GIScience & Remote Sensing*. **52**(2), 198-217. doi: 10.1080/15481603.2015.1008621

Phillips, T., Rajaram, H., Steffen, K., (2010). Cryo-hydrologic warming: A potential mechanism for rapid thermal response of ice sheet. *Geophysical Research Letters*. **37**(20), L20503. doi: 10.1029/2010GL044397

Poinar, K., Joughin, I., Das, S., Behn, M., Lenaerts, J., van den Broeke, M., (2015). Limits to future expansion of surface-melt-enhanced ice flow into the interior of western Greenland. *Geophysical Research Letters*. **42**(6), 1800-1807. doi: 10.1002/2015GL063192

Poinar, K., Joughin, I., Lilien, D., Brucker, L., Kehrl, L., Nowicki, S., (2017). Drainage of southeast Greenland firn aquifer water through crevasses to the bed. *Frontiers in Earth Science*. **5**(5). doi: 10.3389/feart.2017.00005

Price, S., Hoffman, M., Bonin, J., Howat, I., Neumann, T., Saba, J., Tezaur, I., Geurber, J., Chambers, D., Evans, K., Kennedy, J., Lenaerts, J., Lipscomb, W., Perego, M., Salinger, A., Tuminaro, R., van den Broeke, M., Nowicki, S., (2017). An ice sheet model validation framework for the Greenland ice sheet. *Geoscientific Model Development*. **10**(1), 255-270. doi: 10.5194/gmd-10-255-2017

Pritchard, H., Arthern, R., Vaughan, D., Edwards, L., (2009). Extensive dynamic thinning on the margins of the Greenland and Antarctic Ice Sheets. *Nature*. **461**, 971-975. doi: 10.1038/nature08471

Raymond, J., Gudmundsson, H., (2005). On the relationship between surface and basal properties on glaciers, ice sheets, and ice streams. *Journal of Geophysical Research*. **110**(B8), B08411. doi: 10.1029/2005JB003681

Raymond, M., Gudmundsson, H., (2009). Estimating basal properties of ice streams from surface measurements: a non-linear Bayesian inverse approach applied to synthetic data. *The Cryosphere*. **3**(2), 265-278. doi: 10.5194/tc-3-265-2009

Raymond Pralong, M., Gudmundsson, H., (2011). Bayesian estimation of basal conditions on Rutford Ice Stream, West Antarctica, from surface data. *Journal of Glaciology*. **57**(202), 315-324. doi: 10.3189/002214311796406004

Rennermalm, A., Moustafa, S., Mioduszewski, J., Chu, V., Forster, R., Hagedorn, B., Harper, J., Mote, T., Robinson, D., Shuman, C., Smith, L., Tedesco, M., (2013). Understanding Greenland ice sheet hydrology using an integrated multi-scale approach. *Environmental Research Letters*. **8**(1), 015017. doi: 10.1088/1748-9326/8/1/015017

Rignot, E., Box, J., Burgess, E., Hanna, E., (2008). Mass balance of the Greenland ice sheet from 1958 to 2007. *Geophysical Research Letters*. **35**(20), L20502. doi: 10.1029/2008GL035417

Rignot, E., Mouginot, J., (2012). Ice flow in Greenland for the International Polar Year 2008-2009. *Geophysical Research Letters*. **39**(11), L11501. doi: 10.1029/2012GL051634

Rippin, D., (2013). Bed roughness beneath the Greenland ice sheet. *Journal of Glaciology*. **59**(216), 724-732. doi: 10.3189/2013JoG12J212

Rippin, D., Bingham, R., Jordan, T., Wright, A., Ross, N., Corr, H., Ferraccioli, F., Le Brocq, A., Rose, K., Siegert, M. (2014). Basal roughness of the Institute and Möller Ice Streams, West Antarctica: Process determination and landscape interpretation. *Geomorphology*. **214**, 139-147. doi: 10.1016/j.geomorph.2014.01.021

Rosenau, R., Scheinert, M., Dietrich, R., (2015). A processing system to monitor Greenland outlet glacier velocity variations at decadal and seasonal time scales utilizing the Landsat imagery. *Remote Sensing of Environment*. **169**, 1-19. doi: 10.1016/j.rse.2015.07.012

Ross, N., Jordan, T., Bingham, R., Corr, H., Ferraccioli, F., Le Brocq, A., Rippin, D., Wright, A., Siegert, M., (2014). The Ellsworth Subglacial Highlands: Inception and retreat of the West Antarctic Ice Sheet. *GSA Bulletin*. **126**(1/2), 3-15. doi: 10.1130/B30794.1

Ross, N., Sole, A., Livingstone, S., Ignéczi, Á., Morlighem, M., (2018). Near-margin ice thickness from a portable radar: implications for subglacial water routing, Leverett Glacier, Greenland. *Arctic, Antarctic and Alpine Research*. **50**(1), e1420949. doi: 10.1080/15230430.2017.1420949

Röthlisberger, H., (1972). Water pressure in intra- and subglacial channels. *Journal of Glaciology*. **11**(62), 177-203. doi: 10.3189/S0022143000022188

Selmes, N., Murray, T., James, T., (2011). Fast-draining lakes on the Greenland Ice Sheet. *Geophysical Research Letters*. **38**(15), L15501. doi: 10.1029/2011GL047872

Selmes, N., Murray, T., James, T., (2013). Characterizing supraglacial lake drainage and freezing on the Greenland ice sheet. *The Cryosphere Discussion*. **7**, 475-505. doi: 10.5194/tcd-7-475-2013

Sergienko, O., (2012). The effects of transverse bed topography variations in ice flow models. *Journal of Geophysical Research: Earth Surface*. **117**(F3), F03011. doi: 10.1029/2011JF002203

Sergienko, O., (2013). Glaciological twins: basally controlled subglacial and supraglacial lakes. *Journal of Glaciology*. **59**(213), 3-8. doi: 10.3189/2013JoG12J040

Shannon, S., Payne, A., Bartholomew, I., van den Broeke, M., Edwards, T., Fettweis, X., Gagliardini, O., Gillet-Chaulet, F., Goelzer, H., Hoffman, M., Huybrechts, P., Mair, D., Nienow, P., Perego, M., Price, S., Smeets, P., Sole, A., van de Wal, R., Zwinger, T., (2013). Enhanced basal lubrication and the contribution of the Greenland ice sheet to future sea-level rise. *PNAS*. **110**(35), 14156-14161. doi: 10.1073/pnas.1212647110

Shepherd, A., Hubbard, A., Nienow, P., King, M., McMillan, M., Joughin, I., (2009). Greenland ice sheet motion coupled with daily melting in late summer. *Geophysical Research Letters*. **36**(1), L01501. doi: 10.1029/2008GL035758

Shepherd, A., Ivins, E., Geruo, A., Barletta, V., Bentley, M., Bettadpur, S., Briggs, K., Bromwich, D., Forsberg, R., Galin, N., Horwath, M., Jacobs, S., Joughin, I., King, M., Lenaerts, J., Li, J., Ligtenberg, S., Luckman, A., Luthcke, S., McMillan, M., Meister, R., Milne, G., Mouginot, J., Muir, A., Nicolas, J., Paden, J., Payne, A., Pritchard, H., Rignot, E., Rott, H., Sørensen, L., Scambos, T., Scheuchl, B., Schrama, E., Smith, B., Sundal, A., van Angelen, J., van der Berg, W., van den Broeke, M., Vaughan, D., Velicogna, I., Wahr, J., Whitehouse, P., Wingham, D., Yi, D., Young, D., Zwally, H.J., (2012). A reconciled estimate of ice sheet mass balance. *Science*. **338**(6111), 1183-1189. doi: 10.1126/science.1228102

Shreve, R., (1972). Movement of water in glaciers. *Journal of Glaciology*. **11**(62), 205-214. doi: 10.3189/S002214300002219X

Slater, D., Nienow, P., Cowton, T., Goldberg, D., Sole, A., (2015). Effect of near-terminus subglacial hydrology on tidewater submarine melt rates. *Geophysical Research Letters*. **42**(8), 2861-2868. doi: 10.1002/2014GL062494

Slater, D., Nienow, P., Goldberg, D., Cowton, T., Sole, A., (2017a). A model for tidewater glacier undercutting by submarine melting. *Geophysical Research Letters*. **44**(5), 2360-2368. doi: 10.1002/2016GL072374.

Slater, D., Nienow, P., Sole, A., Cowton, T., Mottram, R., Langen, P., Mair, D., (2017b). Spatially distributed runoff at the grounding line of a large Greenlandic tidewater glacier inferred from plume modelling. *Journal of Glaciology*. **63**(238), 309-323. doi: 10.1017/jog.2016.139

Smith, R., Baker, K., (1981). Optical properties of the clearest natural waters (200-800 nm). *Applied Optics*. **20**(2), 177-184. doi: 10.1364/AO.20.000177

Smith, L., Chu, V., Yang, K., Gleason, C., Pitcher, L., Rennermalm, A., Legleiter, C., Behar, A., Overstreet, B., Moustafa, S., Tedesco, M., Forster, R., LeWinter, A., Finnegan, D., Sheng, Y., Balog, J., (2015). Efficient meltwater drainage through supraglacial stream and rivers on the southwest Greenland ice sheet. *PNAS*. **112**(4), 1001-1006. doi: 10.1073/pnas.1413024112

Sneed, W., Hamilton, G., (2007). Evolution of melt pond volume on the surface of the Greenland Ice Sheet. *Geophysical Research Letters*. **34**(3), L03501. doi: 10.1029/2006GL028697

Sole., A, Mair, D., Nienow, P., Bartholomew, I., King, M., Burke, M., Joughin, I., (2011). Seasonal speedup of a Greenland marine terminating outlet glacier forced by surface melt-induced changes in subglacial hydrology. *Journal of Geophysical Research: Earth Surface*. **116**(F3), F03014. doi: 10.1029/2010JF001948

Sole, A., Nienow, P., Bartholomew, I., Mair, D., Cowton, T., Tedstone, A., King, M., (2013). Winter motion mediates dynamic response of the Greenland Ice Sheet to warmer summers. *Geophysical Research Letters*. **40**(15), 3940-3944. doi: 10.1002/grl.50764

Stevens, L., Behn, M., McGuire, J., Das, S., Joughin, I., Herring, T., Shean, D., King, M., (2015). Greenland supraglacial lake drainages triggered by hydrologically induced basal slip. *Nature*. **522**, 73-76. doi: 10.1038/nature14480

Straneo, F., Curry, R., Sutherland, D., Hamilton, G., Cenedese, C., Våge, K., Stearns, L., (2011). Impact of fjord dynamics and glacial runoff on the circulation near Helheim Glacier. *Nature Geoscience*. **4**, 322-327. doi: 10.1038/ngeo1109

Sundal, A., Shepherd, A., Nienow, P., Hanna, E., Palmer, S., Huybrechts, P., (2009). Evolution of supra-glacial lakes across the Greenland Ice Sheet. *Remote Sensing of Environment*. **113**(10), 2164-2171. doi: 10.1016/j.rse.2009.05.018

Tedesco, M., Lüthje, M., Steffen, K., Steiner, N., Fettweis, X., Willis, I., Bayou, N., Banwell, A., (2012). Measurement and modelling of ablation of the bottom of supraglacial lakes in western Greenland. *Geophysical Research Letters*. **39**(2), L02502. doi: 10.1029/2011GL049882

Tedesco, M., Mote, T., Fettweis, X., Hanna, E., Jeyaratnam, J., Booth, J., Datta, R., Briggs, K., (2016). Arctic cut-off high drives the poleward shift of new Greenland melting record. *Nature Communications*. **7**, 11723. doi: 10.1038/ncomms11723

Tedesco, M., Willis, I., Hoffman, M., Banwell, A., Alexander, P., Arnold, N., (2013). Ice dynamic response to two modes of surface lake drainage on the Greenland ice sheet. *Environmental Research Letters*. **8**(3), 034007. doi: 10.1088/1748-9326/8/3/034007

Tedstone, A., Nienow, P., Gourmelen, N., Dehecq, A., Goldberg, D., Hanna, E., (2015). Decadal slowdown of a land-terminating sector of the Greenland Ice Sheet despite warming. *Nature*. **526**, 692-695. doi: 10.1038/nature15722

Van As, D., Hubbard, A., Hasholt, B., Mikkelsen, A., van den Broeke, M., Fausto, R., (2012). Large surface meltwater discharge from the Kangerlussuaq sector of the Greenland ice sheet during the record-warm year 2010 explained by detailed energy balance observations. *The Cryosphere*. **6**(1), 199-209. doi: 10.5194/tc-6-199-2012

Van de Wal, W., Boot, W., van den Broeke, M., Smeets, C., Reijmer, C., Donker, J., Oerlemans, J., (2008). Large and rapid melt-induced velocity change in the ablation zone of the Greenland Ice Sheet. *Science*. **321**(5885), 111-114. doi: 10.1126/science.1158540

Van de Wal, R., Smeets, C., Boot, W., Stoffelen, M., van Kampen, R., Doyle, S., Wilhelms, F., van den Broeke, M., Reijmer, C., Oerlemans, J., Hubbard, A., (2015). Self-regulation of ice flow varies across the ablation area in south-west Greenland. *The Cryosphere*. **9**(2), 603-311. doi: 10.5194/tc-9-603-2015

Van den Broeke, M., Bamber, J., Ettema, J., Rignot, E., Schrama, E., van de Berg, W., van MeijGaard, E., Velicogna, I., Wouters, B., (2009). Partitioning recent Greenland mass loss. *Science*. **326**(5955), 984-986. doi: 10.1126/science.1178176

Van den Broeke, M., Enderlin, E., Howat, I., Kuipers Munneke, P., Noël, B., van de Berg, W., van Meijgaard, E., Wouters, B., (2016). On the recent contribution of the Greenland Ice Sheet to sea level change. *The Cryopshere*. **10**(5), 1933-1946. doi: 10.5194/tc-10-1933-2016

Van der Veen, C., (2007). Fracture propagation as means of rapidly transferring surface melt-water to the base of glaciers. *Geophysical Research Letters*. **34**(1), L03501. doi: 10.1029/2006GL028385

Vaughan, D., (1995). Tidal flexure at ice shelf margins. *Journal of Geophysical Research: Solid Earth*. **100**(B4), 6213-3224. doi: 10.1029/94JB02467

Vizcaino, M., Mikolajewicz, U., Ziemen, F., Rodehacke, C., Greve, R., van den Broeke, M., (2014). Coupled simulations of Greenland Ice Sheet and climate change up to A.D. 2300. *Geophysical Research Letters*. **42**(10), 3927-3935. doi: 10.1002/2014GL061142.

Weertman, J., (1964). The theory of glacier sliding. *Journal of Glaciology*. **5**(39), 287-303. doi: 10.3189/S0022143000029038

Weertman, J., (1971) Theory of water-filled crevasses in glaciers applied to vertical magma transport beneath oceanic ridges. *Journal of Geophysical Research*. **76**(5), 1171–1183. doi: 10.1029/JB076i005p01171

Weertman, J., (1973). Can a water-filled crevasse reach the bottom surface of a glacier? *International Association of Scientific Hydrology Publication 95 (Symposium at Cambridge 1969 – Hydrology of Glaciers)*. 139–145.

Weertman, J., (1996). *Dislocation based fracture mechanics*. River Edge, N.J.: World Scientific Publishing.

Whillans, I., (1975). Effect of inversion winds on topographic detail and mass balance on inland ice sheets. *Journal of Glaciology*. **14**(70), 85-90. doi: 10.1080/15230430.2017.1420949

Willis, M., Herried, B., Bevis, M., Bell, R., (2015). Recharge of a subglacial lake by surface meltwater in northeast Greenland. *Nature*. **518**, 223-227. doi: 10.1038/nature14116

Yang, K., Smith, L., (2016). Internally drained catchments dominate supraglacial hydrology of the southwest Greenland Ice Sheet. *Journal of Geophysical Research: Earth Surface*. **121**(10), 1891-1910. doi: 10.1002/2016JF003927

Yang, K., Smith, L., Chu, V., Gleason, C., Li, M., (2015). A caution on the use of surface digital elevation models to simulate supraglacial hydrology of the Greenland Ice Sheet. *IEEE Journal of Selected Topics in Applied Earth Observations and Remote Sensing*. **8**(11), 5212-5224. doi: 10.1109/JSTARS.2015.2483483

Yang, K., Smith, L., Chu, V., Pitcher, L., Gleason, C., Rennermalm, A., Li, M., (2016). Fluvial morphometry of supraglacial river networks on the southwest Greenland Ice Sheet. *GIScience & Remote Sensing*. **53**(4), 459-482. doi: 10.1080/15481603.2016.1162345

Zwally, H.J., Abdalati, W., Herring, T., Larson, K., Saba, J., Steffen, K., (2002). Surface melt-induced acceleration of Greenland Ice-Sheet flow. *Science*. **297**(5579), 218-222. doi: 10.1126/science.1072708

Zwally, H.J., Giovinetto, M., Beckley, M., Saba, J., (2012). Antarctic and Greenland Drainage Systems. GSFC Cryospheric Sciences Laboratory. at http://icesat4.gsfc.nasa.gov/cryo_data/ant_grn_drainage_systems.php.